

# **Applications of Electrospinning in Post-Lithium-Ion Batteries**

Zur Erlangung des akademischen Grades eines  
DOKTORS DER NATURWISSENSCHAFTEN  
(Dr. rer. nat.)

von der KIT-Fakultät für Chemie und Biowissenschaften  
des Karlsruher Instituts für Technologie (KIT)

genehmigte

DISSERTATION

von

M.Eng. Xinyang Liu-Théato geb. Liu  
aus Heilongjiang, China

KIT-Dekan: Prof. Dr. Manfred Wilhelm

Referent: Prof. Dr. Helmut Ehrenberg

Korreferent: Prof. Dr. Rolf Schuster

Tag der mündlichen Prüfung: 07.12.2020



Die vorliegende Arbeit wurde im Zeitraum vom 1. Februar 2018 bis 1. Oktober 2020 am Institut für am Institut für Angewandte Materialien und der Anorganischen Chemie der Fakultät für Chemie und Biowissenschaften am Karlsruher Institut für Technologie (KIT) unter der Leitung von Prof. Dr. Helmut Ehrenberg angefertigt.

Hiermit versichere ich, die vorliegende Arbeit selbstständig verfasst und keine anderen als die angegebenen Quellen und Hilfsmittel verwendet sowie Zitate kenntlich gemacht zu haben. Die Dissertation wurde bisher an keiner anderen Hochschule oder Universität eingereicht.



## Contents

ABSTRACT .....	1
Zusammenfassung .....	3
Abbreviation .....	5
1 Introduction .....	7
2 Background .....	9
2.1 Post-lithium-ion batteries .....	9
2.1.1 Lithium-ion batteries .....	9
2.1.1 Post-lithium-ion batteries .....	12
2.1.2 Sodium-ion batteries .....	14
2.1.3 Magnesium-sulfur batteries .....	19
2.2 Electrospinning technology .....	21
2.2.1 Electrospinning principle .....	21
2.2.2 Electrospinning of nanofibers .....	22
2.2.3 Electrospinning of carbon nanofibers .....	24
2.3 Applications of electrospinning in post-lithium-ion batteries .....	26
2.3.1 Applications in anode materials for SIBs .....	26
2.3.2 Applications in cathode materials for SIBs .....	29
2.3.3 Applications in modified separators for Mg-S batteries .....	31
3 Scope and objectives .....	33
4 Mechanisms of carbon nanofibers as anode materials for SIBs .....	35
4.1 Experimental part .....	35
4.1.1 Material preparation .....	35
4.1.2 Material characterization .....	36
4.1.3 Electrochemical performance .....	37

4.2	Results and discussions .....	37
4.2.1	Morphology and structure .....	37
4.2.2	Electrochemical performance.....	41
4.2.3	<i>In situ</i> and <i>ex situ</i> studies.....	52
4.3	Summary .....	53
5	Self-standing NaFePO <sub>4</sub> / carbon nanofiber cathode for SIBs .....	54
5.1	Experimental part .....	54
5.1.1	Material preparation .....	54
5.1.2	Material characterization.....	55
5.1.3	Electrochemical performance.....	56
5.2	Results and discussions .....	57
5.2.1	Morphology and structure .....	57
5.2.2	Electrochemical performance.....	61
5.2.3	<i>Ex situ</i> studies.....	68
5.3	Summary .....	72
6	Polyoxometalate/carbon-based modified separator for Mg-S batteries .....	74
6.1	Experimental part .....	74
6.1.1	Material preparation .....	74
6.1.2	Material characterization.....	76
6.1.3	Electrochemical performance.....	77
6.2	Results and discussions .....	77
6.2.1	Morphology and structure .....	77
6.2.2	Electrochemical performance.....	82
6.2.3	<i>Ex situ</i> studies.....	87
6.3	Summary .....	90

---

7	Conclusions and outlook .....	91
8	References .....	93
9	Acknowledgement.....	108



## ABSTRACT

The worldwide energy consumption is growing rapidly nowadays and renewable energies are playing a critical role in alleviating this energy crisis. Batteries, as sustainable energy storage systems, are emerging as the key solutions to effectively integrate renewable resources. The lithium-ion battery is the most widely used rechargeable battery nowadays; however, limitations in uneven distribution of raw materials and high risk of increasing costs have motivated researchers to seek for alternatives such as sodium-ion batteries or metal sulfur batteries, mostly summarized as post-lithium-ion batteries. Different storage mechanisms and new materials are potentially able to maintain structural stability and offer high energy density, among which nanomaterials have attracted a lot of attention. As a low-cost, controllable and scalable method of nanomaterial fabrication, electrospinning was applied in three different aspects in post-lithium-ion batteries in this work: (i). Carbon nanofibers (CNFs) were synthesized as anode material in sodium-ion batteries; (ii). Nanocomposites from maricite  $\text{NaFePO}_4$  and carbon nanofibers were developed as cathode material in sodium-ion batteries; (iii). Modified separator aided with electrospinning was applied in magnesium-sulfur batteries.

(i). Free standing carbon nanofibers in the form of fiber mats were successfully prepared by electrospinning and directly used as negative electrode in sodium-ion batteries. Different carbonization temperatures were carried out to generate various carbon structures containing both graphitic domains and defects. Morphologies of the electrodes before and after cycling were analyzed. From extensive electrochemical analysis such as cyclic voltammetry and *in situ* Raman spectroscopy, the behavior of each kind of CNFs was characterized. The CNFs carbonized at 600 and 800 °C exhibited a capacitive behavior from surface charging while the CNFs treated at 1000 °C followed a mixed diffusion-controlled and surface-controlled behavior. *In situ* Raman spectra showed that the G-band was shifted upon discharge, which proved an intercalation of sodium ions into the carbon host. However, the irreversible high capacity loss in the first cycle is the main reason of hindering the application of such CNFs as anode materials in sodium-ion batteries.

(ii). A self-standing, collector-free, binder-free maricite  $\text{NaFePO}_4$  / carbon nanofiber hybrid positive electrode was successfully prepared via electrospinning. An increased capacity was observed in the initial cycles and finally the electrode reached a capacity of 108 mAh g<sup>-1</sup> based on the mass of active material  $\text{NaFePO}_4$  (30 wt%) at a 0.1C rate after 200 cycles. In comparison, a

slurry-based NaFePO<sub>4</sub> electrode yields a capacity of only around 20 mAh g<sup>-1</sup>. A comprehensive study of the hybrid electrode's morphology, structure, and electrochemical performance was conducted. Mössbauer spectra showed an increasing Fe<sup>3+</sup> content from 43.2% at the first charged state to 63.0% at the charged state after 100 cycles, demonstrating an activating process of maricite NaFePO<sub>4</sub> upon extensive charge-discharge cycling. This study on self-standing positive electrodes revealed the change in activity of maricite NaFePO<sub>4</sub> from electrochemical inactive to active within the network of carbon nanofibers upon charge-discharge cycles.

(iii). Magnesium-sulfur (Mg-S) batteries, with a high theoretical volumetric energy up to 3200 Wh/L, are considered to be competitive post-lithium battery systems. However, the known "shuttle effect" of soluble polysulfides during cycling typically leads to rapid capacity fade that greatly hinders their practical applications. Although considerable efforts have been made in cathode design and electrolyte development, the functionalization of separators is often neglected. In this study, a one-side coated glass fiber separator with polyoxometalate/carbon composite materials was prepared via electrospinning as a "polysulfide-phobic" shield. Mg-S batteries assembled with such a coated separator showed significantly enhanced cycling stability with a capacity of 350 mAh g<sup>-1</sup> for over 100 cycles. Furthermore, a compact and low-cost battery design was realized with conductive carbon/S as cathode, Mg foil as anode and additive-free Mg[B(hfip)<sub>4</sub>]<sub>2</sub> as electrolyte. This electrospun functional separator is expected to enlighten future separator design for metal-sulfur batteries towards practical applications.

## Zusammenfassung

Um dem weltweit rasch wachsenden Energieverbrauch heutzutage Herr zu werden, spielen erneuerbare Energien eine entscheidende Rolle. Batterien als nachhaltige Energiespeichersysteme entwickeln sich zu den wichtigsten Lösungen für eine effektive Integration erneuerbarer Energien. Die Lithium-Ionen-Batterie ist heutzutage die am weitesten verbreitete wiederaufladbare Batterie; jedoch haben Einschränkungen bei der ungleichmäßigen Verteilung der benötigten Rohstoffe und das hohe Risiko steigender Kosten die Forscher dazu motiviert, nach Alternativen wie Natrium-Ionen-Batterien oder Metallschwefelbatterien zu suchen, die generell als Post-Lithium-Ionen-Batterien zusammengefasst werden. Alternative Speichermechanismen und neue Materialien sind potenziell in der Lage, die strukturelle Stabilität von Post-Lithium-Ionen-Batterien aufrechtzuerhalten und eine hohe Energiedichte zu bieten. Insbesondere Nanomaterialien haben hier große Aufmerksamkeit erlangt. Als eine kostengünstige, kontrollierbare und skalierbare Methode zur Herstellung von Nanomaterialien wurde in dieser Arbeit das Elektrosponnen in drei verschiedenen Aspekten bei Post-Lithium-Ionen-Batterien angewandt: (i). Kohlenstoff-Nanofasern (CNF) wurden als negative Elektrode in Natrium-Ionen-Batterien hergestellt; (ii). Nanokomposite aus  $\text{NaFePO}_4$  und Kohlenstoff-Nanofasern wurden als positive Materialien in Natrium-Ionen-Batterien entwickelt; (iii). Ein modifizierter durch Elektrosponnen hergestellter Separator wurde in Magnesium-Schwefel-Batterien eingesetzt.

(i). Freistehende Kohlenstoff-Nanofasern in Form von Fasermatten wurden erfolgreich durch Elektrosponnen hergestellt und direkt als negative Elektrode in Natrium-Ionen-Batterien verwendet. Es wurden verschiedene Karbonisierungstemperaturen durchgeführt, um verschiedene Kohlenstoffstrukturen zu erzeugen, die sowohl graphitische Domänen als auch Defekte enthielten. Die Morphologien der Elektroden vor und nach dem Zyklisieren wurden analysiert. Durch umfangreiche elektrochemische Analysen wie z.B. zyklische Voltammetrie und *in situ* Raman-Spektroskopie wurde das Verhalten der einzelnen CNFs charakterisiert. Die bei 600 und 800 °C karbonisierten CNFs zeigten ein kapazitives Verhalten durch Oberflächenaufladung, während die bei 1000 °C behandelten CNFs ein gemischtes diffusionskontrolliertes und oberflächenkontrolliertes Verhalten aufwiesen. In-situ-Raman-Spektren zeigten, dass die G-Bande bei der Entladung verschoben wurde, was die Interkalation von Natriumionen bewies. Der

irreversible hohe Kapazitätsverlust im ersten Zyklus ist jedoch der Hauptgrund warum solche CNFs als Anodenmaterial in Natrium-Ionen-Batterien bisher keine Anwendung gefunden haben.

(ii). Eine selbststehende, kollektor- und bindemittelfreie Maricit  $\text{NaFePO}_4$  / Kohlenstoff-Nanofaser-Hybrid-Positivelektrode wurde erfolgreich durch Elektrosinnen hergestellt. In den ersten Zyklen wurde eine Zunahme der Kapazität beobachtet, und schließlich erreichte die Elektrode nach 200 Zyklen eine Kapazität von  $108 \text{ mAh g}^{-1}$  basierend auf der Masse des aktiven Materials  $\text{NaFePO}_4$  bei einer Rate von  $0,1\text{C}$ . Im Vergleich dazu ergibt eine auf Slurry basierende  $\text{NaFePO}_4$ -Elektrode nur eine Kapazität von etwa  $20 \text{ mAh g}^{-1}$ . Eine umfassende Studie zur Morphologie, Struktur und elektrochemischen Leistung der Hybridelektrode wurde durchgeführt. Mössbauer-Spektren zeigten einen Anstieg des  $\text{Fe}^{3+}$ -Gehalts von  $43,2\%$  im ersten geladenen Zustand auf  $63,0\%$  im geladenen Zustand nach 100 Zyklen, was einen Aktivierungsprozess des Maricits  $\text{NaFePO}_4$  nach zahlreichen Ladungs-Entladungs-Zyklen zeigte. Diese Studie einer selbsttragenden positiven Elektrode zeigte die Aktivitätsänderung von Maricit  $\text{NaFePO}_4$  von elektrochemisch inaktiv zu aktiv innerhalb des Netzwerks von Kohlenstoff-Nanofasern durch Lade-Entladezyklen.

(iii). Magnesium-Schwefel-Batterien (Mg-S) mit einer theoretisch hohen volumetrischen Energie von bis zu  $3200\text{Wh/L}$  werden als wettbewerbsfähige Post-Lithium-Batteriesysteme angesehen. Allerdings führt der bekannte "shuttle effect" löslicher Polysulfide während des Zyklierens typischerweise zu einem schnellen Kapazitätsschwund, der die praktische Anwendung von Mg-S Batterien zurzeit noch verhindert. Obwohl erhebliche Anstrengungen im Kathodendesign und in der Elektrolytentwicklung unternommen wurden, wird die zusätzliche Funktionalisierung von Separatoren als Polysulfid-Sperre oft vernachlässigt. In dieser Studie wurde ein einseitig beschichteter Glasfaserseparator mit Polyoxometalat/Kohlenstoff-Verbundmaterialien durch Elektrosinnen als "polysulfid-phobe" Abschirmung hergestellt. Mg-S-Batterien, die mit einem solchen beschichteten Separator gebaut wurden, zeigten eine signifikant verbesserte Zyklenstabilität mit einer Kapazität von  $350 \text{ mAh g}^{-1}$  für über 100 Zyklen. Darüber hinaus wurde ein kompaktes und kostengünstiges Batteriedesign mit leitfähigem Kohlenstoff/S als Kathode, Mg-Folie als Anode und additivfreiem  $\text{Mg}[\text{B}(\text{hfip})_4]_2$  als Elektrolyt realisiert. Von diesem elektrogenesponnenen Funktionsseparator wird erwartet, dass er zukünftige Separatordesigns für Metall-Schwefel-Batterien bereichern wird und zu praktischen Anwendungen führen kann.

---

## Abbreviation

CNF	Carbon nanofiber
CV	Cyclic voltammetry
GF	Glass fiber
DEC	Diethyl carbonate
DMC	Diethyl carbonate
DME	Dimethoxy ethane
DMF	Dimethylformamide
EC	Ethylene carbonate
EDX	Energy-dispersed X-ray spectroscopy
EIS	Electro impedance spectroscopy
es-	electrospun
ESS	Energy storage system
GIC	Graphite intercalation compound
HT	High temperature
KB	Ketjen black
LIB	Lithium-ion battery
Li - S	Lithium - sulfur
Mg - S	Magnesium - sulfur
MSB	Magnesium - sulfur battery
NMP	<i>N</i> -Methyl-2-pyrrolidone

---

PAN	Polyacrylonitrile
PC	Propylene carbonate
PEO	Poly(ethylene oxide)
PI	Polyimide
PMMA	Poly- (methyl methacrylate)
POM	Polyoxometalate
Post-LIB	Post-lithium-ion battery
PVAc	Poly- (vinyl acetate)
PVdF	Poly (vinylidene fluoride)
PVP	Poly(vinyl pyrrolidone)
RT	Room temperature
SEI	Solid electrolyte interphase
SEM	Scanning electron microscope
SHE	Standard hydrogen electrode
SIB	Sodium-ion battery
TGA	Thermogravimetric analysis
VOC	Open-circuit Voltage
XPS	X-ray photoelectron spectroscopy
XRD	X-ray diffraction

## 1 Introduction

Fossil fuels such as coal, oil and gas are the most widely used energy resource worldwide.<sup>1</sup> Risks related to resource depletion, environmental pollution and climate change have been constantly increasing since the industrialization of modern society.<sup>2</sup> Moreover, the competition over the limited traditional energy resources have constantly caused uneven development, economic conflict and political unrest. With the changing lifestyles of an increasing global population, the energy demand of human beings will double from 14 TW (2010) to 28 TW (2050), as shown in Figure 1.1. This ever-growing energy demand and depleting fossil fuels have accelerated the significant reform and concerted transition in energy sources.<sup>3</sup> Renewable and cleaner energy alternatives such as wind, solar and wave energy start to play more and more important roles in reducing environmental impacts by emitting significantly less pollutants (e.g. CO, CO<sub>2</sub>, C<sub>n</sub>H<sub>m</sub>, SO<sub>x</sub>, NO<sub>x</sub>; heavy metals, ashes, etc.).<sup>4,5</sup> Within the last decades, a significant expansion in renewable energy resources has solved many urgent needs in electricity demands especially in developing countries like India and China.<sup>6</sup>

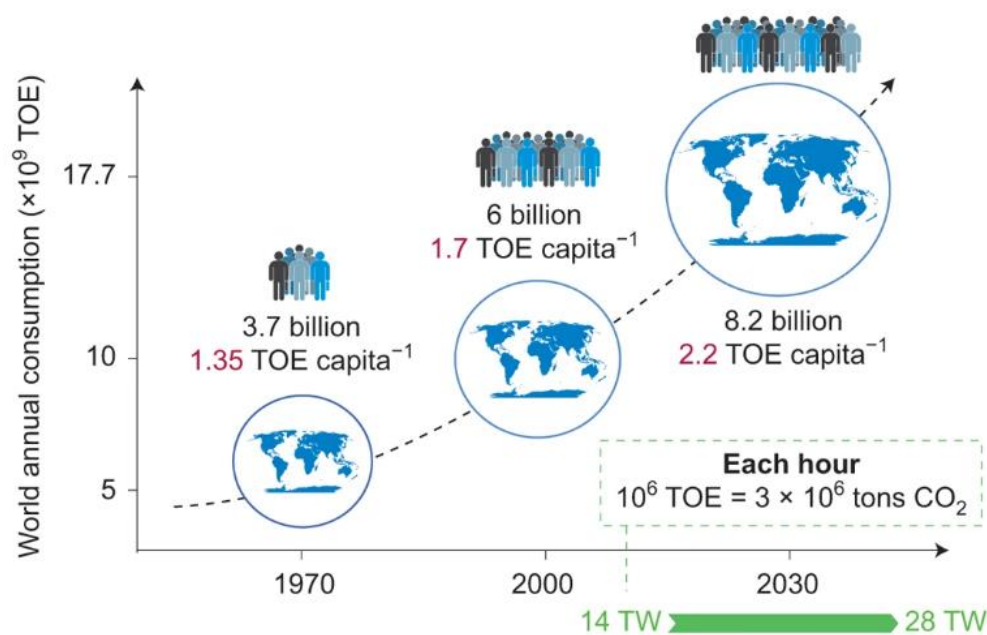


**Figure 1.1** The energy demand worldwide based on TOE (tonnes of oil equivalent) from the past to the future (Reprinted from ref.3, Copyright (2014), with permission from Springer Nature)

Nature itself provides multifold and abundant energy powers. However, when harvesting energy resources from nature, uncontrollable weather conditions and day-night time variations have a huge impact on energy availability and converting efficiency. Thus, a large-scale energy storage system (ESS) is critical for a highly efficient transmission in order to transfer these renewable energies into the electrical grid, storing during surplus energy and outputting it when needed.<sup>7</sup> Unfortunately, the storage grids only have the capacity to obtain around 1% of the energy consumed worldwide.<sup>3</sup> Efficient, reliable, sustainable and low-cost energy storage devices and systems are in high demand. Current energy storage technologies can be generally divided into five types: mechanical, electrical, chemical, electrochemical and hydrogen storage.<sup>8</sup> Among all these technologies, electrochemical energy storage possesses some desirable features, including pollution-free operation, flexible power and energy characteristics, long cycle life and low maintenance.<sup>9</sup>

The rechargeable battery system is considered to be a promising energy storage facility with high-value opportunities. Representatives such as lithium-ion batteries show advantages among the energy storage systems which allows for small size and lightweight applications. In nowadays daily life, one can interact with lithium-ion batteries multiple times: starting with an electronic toothbrush in the morning, riding an electric bicycle to work, working with a laptop and using a cellphone through the whole day. Portable electronic devices have become such an important part of our lives that one can get anxiety by being without one. Moreover, rechargeable lithium-ion batteries have made electrical vehicles possible with the potential to decrease CO<sub>2</sub> emission in a long run. From large scale systems to portable small devices, the improvement of rechargeable batteries is of great importance for sustainable technology development.

## 2 Background

### 2.1 Post-lithium-ion batteries

#### 2.1.1 Lithium-ion batteries

The ongoing industrialization and technology development have led to a more and more energy powered and electricity driven society. Facing the crisis from limited traditional energy sources and unavoidable pollutions, humans are devoted to seek alternative energy sources. Since the debut of commercialized lithium-ion batteries (LIBs) by Sony in 1991, LIBs has accelerated the growth of portable devices, electrical vehicles and novel energy resources.<sup>10</sup> Lithium is the lightest metal (6.94 u), offers a low standard reduction potential (-3.04 V), and is capable to deliver a significant high energy density and a high working voltage up to 3.6 V compared to traditional lead or zinc batteries.<sup>11</sup>

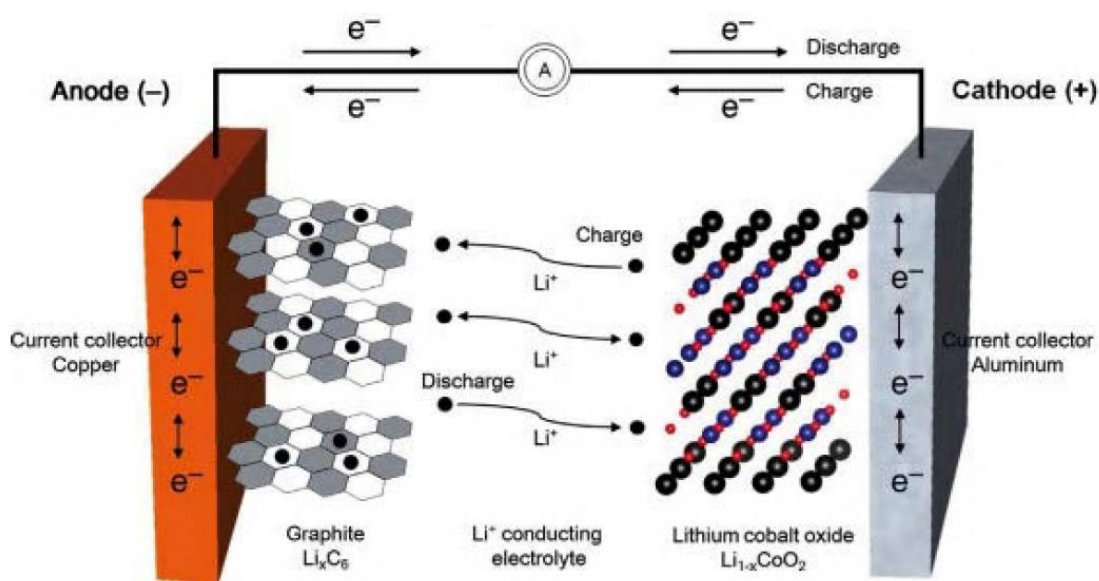
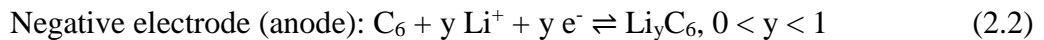
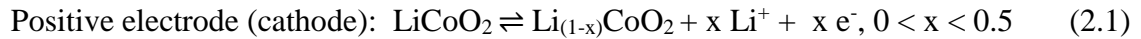


**Figure 2.1** Schematic illustration of the charge-discharge process in lithium-ion cell consisting of lithium insertion compounds as both anode and cathode of work. (Reprinted from ref.12, Copyright (2012), with permission from John Wiley and Sons)

The working principle of a typical rechargeable battery is based on a reversible redox-reaction between a cathode material and an anode material. The structure of the LIB is illustrated in Figure 2.1 using lithium cobalt oxide (LiCoO<sub>2</sub>) and graphite as example electrodes. The cathode material and the anode material are spatially separated by a separator but externally connected through an electrical circuit and ionic conductively connected via an electrolyte.<sup>12</sup> Upon discharging (battery delivering an electric current), the anode releases lithium ions to the cathode, generating a flow of electrons externally from one side to the other. The charges released as free electrons accompanied with the movement of lithium ions reach the poles through the current collectors. Reversely, upon charging, the electrons and lithium ions are moving in the opposite directions, being extracted from the cathode material and reinserted into the anode to store the electric energy in form of higher energetic chemical bonds. Cathode materials and anode materials participate in an oxidation/reduction (redox reaction) by releasing or receiving electrons. The reversible electrochemical process is as follows:



It is noteworthy to point out that the definitions of anode and cathode in rechargeable batteries are different from the traditional terms in electrochemistry, which are based on the direction of current flows. Hence, the anode is the negative electrode that releases electrons during discharge, while the electrode that receives electrons during discharge is defined as cathode, i.e. the positive electrode.

The electrode consists of a large majority of electrochemically active material, but also of a polymer binder and a conductive additive. Separator, usually a porous membrane that is filled with liquid electrolyte, is also a critical component of a battery especially for safety issues.<sup>13</sup> The current collector serves as a vital bridge in supporting the electrode, at the same time electrochemically connecting the overall structure of anodes and cathodes with an external circuit.<sup>14</sup>

The open-circuit voltage  $V_{oc}$  in a battery cell is defined as the difference in the lithium chemical potential between the cathode ( $\mu_{c(\text{Li})}$ ) and the anode ( $\mu_{a(\text{Li})}$ ):

$$V_{oc} = \frac{\mu_{c(\text{Li})} - \mu_{a(\text{Li})}}{F} \quad (2.3)$$

Where  $F$  is the Faraday constant. The redox energies of anode ( $E_a$ ) and cathode ( $E_c$ ) need to lie within the band gap of the electrolyte ( $E_g$ ), as shown in Figure 2.2, so that no unexpected reduction or oxidation of the electrolyte will occur during the charge – discharge process. Different structures and geometry of the electrodes will affect the thermodynamic transfer of  $\text{Li}^+$  and electron, thus determine the amount of energy involved in the whole cell. The enhancement in operating voltage window is one of the appropriate approaches to increasing the cell energy.<sup>15</sup>

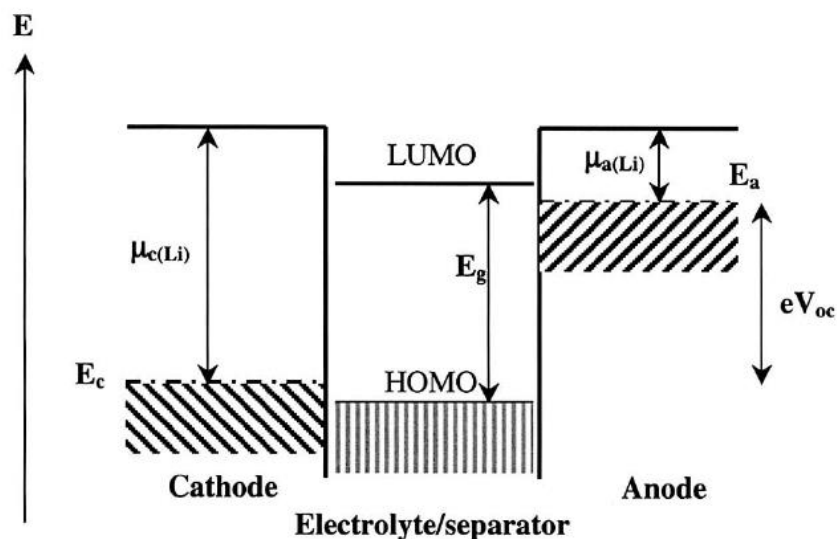


**Figure 2.2** Schematic energy diagram of a lithium cell at open circuit. HOMO and LUMO refer to the highest occupied molecular orbital and lowest unoccupied molecular orbital in the electrolyte.<sup>16</sup>

(Reprinted from ref.16, Copyright (2009), with permission from Springer Nature)

The electrochemical performance of such a cell is also characterized by a few important parameters such as capacity, energy density, power density, and cycle life. The capacity of a battery defines the total amount of charge that can be released during a complete discharge. In another expression, capacity means the potentiality of the amount of electricity able to be released by a pre-charged secondary battery. Cell capacity can be measured by gravimetric specific capacity (Ah/kg, mAh/g) or volumetric specific capacity (Ah/l, mAh/cm<sup>3</sup>). Energy density (Wh/kg) is the amount of energy stored per unit mass or volume, which means that a lower amount of passive material such as current collectors and battery housing results in a higher energy density under the same circumstances. On the other hand, power density is measured in watts per kilogram (W/kg) from the integral of the product of current and voltage over time per weight. A higher operating voltage

will lead to a higher power density, as well as a higher energy density. Cycle life is an indicator of how long the battery can operate and sometimes can only be improved on the cost of charging-discharging rate and energy density. Overall, the electrochemical parameters of a rechargeable battery will inevitably have to be compromised in real-life applications to deliver a reasonable comprehensive performance.

However, the speed of the development of LIBs has been limited by several disadvantages. Challenges in safety, lithium-dendrite formation, unstable long-term structure and poor low-temperature performance have not yet been solved to satisfy the endless demand for better performing batteries. The major challenges come not only from the lithium metal, but also from the components such as intercalation material (cobalt, graphite) and combustible organic electrolyte. Progress in pursuing longer operating time, longer life time, faster charging and lower production cost are continuously being pushed forward. In 2020, research and development of LIBs has reached a phase where an innovative leap is highly welcomed to satisfy the growing customer and technology demands.

### **2.1.1 Post-lithium-ion batteries**

Lithium will eventually reach its limit to meet the ever-growing demand in energy storage industry with its uneven distribution on the earth and increasing production costs.<sup>17</sup> During the last two decades, researchers have explored new electrode materials to develop various battery systems and increase economic efficiency of the rechargeable batteries. Alternative cell configurations composed of the elements such as sodium (Na), magnesium (Mg), potassium (K), aluminum (Al) and sulfur (S) are gaining attention due to their advantages over LIBs in terms of high abundance and potentially lower cost.<sup>18</sup> The concept of post-lithium-ion batteries (post-LIBs) has been brought out to represent sustainable replacements of lithium-ion batteries. It is necessary to point out that some scientists also define post-LIBs on the basis of distinct reactions, such as alloying and conversion, which is beyond the traditional “intercalation” mechanisms.<sup>19</sup>

Presently, the options of post-LIBs are in general consisting of different battery technologies: (1) Sodium-ion batteries (SIBs): as an alkali metal sodium shares similar chemical properties with lithium and hence a large portion of the knowledge that has been accumulated for LIBs can be transferred to SIBs. Moreover, due to the low cost and natural abundance of Na precursors, Na-ion

batteries are considered as a promising alternative to Li-ion technology. Another possible candidate is the K-ion battery which also started to gain momentum in recent years;<sup>20</sup> (2) Multivalent-ions such as Mg-, Al- and Ca-ions batteries: by storing more than one electron per ion, these batteries can offer very high energy densities.<sup>21</sup> The Mg anode is an outstanding candidate due to its high volumetric capacity, abundance and safety.<sup>22,23</sup> (3) Metal-Sulfur batteries: sulfur is one of the most promising active materials with vast abundance and a higher energy density (1675 mAh g<sup>-1</sup>) than LIBs; (4) Metal-air batteries: though having received attention since 1970s, metal-air batteries are still at a situation far away from commercialization due to a poor reversibility.<sup>24,25</sup>

**Table 2.1** Comparison of physical properties of some metal elements as charge carriers for rechargeable batteries.

	Li	Na	K	Mg	Al
Relative atomic mass	6.94	22.99	39.10	24.30	26.95
Cation radius (Å)	0.76	1.06	1.38	0.72	0.535
E <sup>0</sup> (A <sup>n+</sup> <sub>aq</sub> / A) (V vs. SHE)	-3.04	-2.71	-2.93	-2.38	-1.66
Cost (USD / kg)	81.4-85.6	2.57-3.43	12.1-13.6	2.32	1.79
Abundance (crust) (ppm)	17	23,000	15,000	29,000	82,000
Gravimetric capacity (mAh g <sup>-1</sup> )	3861	1166	685 <sup>26</sup>	2205	2980
Volumetric capacity (mAh cm <sup>-3</sup> )	2062	1128	609	3833	8046

Data collected from: ptable.com, chemcool.com, hyperphysics.phy-astr.gsu.edu and Wikipedia

As the replacement of lithium, several metals and their physical properties related to battery applications are shown in Table 2.1. In spite of higher standard reduction potentials than Li, all other metals have noticeable advantages in cost and abundance over lithium. Among the research of last decade, Na-ion battery has received the most attention among all post-LIB candidates with an abundance in crust of 23,000 ppm of sodium compared to 17 ppm of lithium. The battery components, electrical storage mechanism, and intercalation chemistry of cathode materials of SIBs are very similar to those of LIBs except for the ion carriers.<sup>7</sup> As for potassium, with a larger radius, it requires a much higher structural stability of the electrode material for a fast K<sup>+</sup> ion insertion and extraction compared to Na<sup>+</sup> ion. Besides, considering the higher chemical activity and

softer physical property due to the weaker metallic bonds, it is harder to handle K metal than Na metal in a battery assembly.

Another competitive next-generation battery system is the Mg battery, which started to receive intense attention in recent years. The ionic radius of  $\text{Mg}^{2+}$  is 0.86 Å, similar to the 0.9 Å of  $\text{Li}^+$ . However, multivalent metals have higher volumetric capacities (3833 mAh  $\text{cm}^{-3}$  for Mg vs. 2205 mAh  $\text{cm}^{-3}$  for Li) than lithium metal. Moreover, the reduction potential of  $\text{Mg}^{2+}/\text{Mg}$  (-2.4 V vs. standard hydrogen electrode) is 0.72 V lower than that of  $\text{Al}^{3+}/\text{Al}$ , which is critical for a higher cell voltage window even though Al has the highest volumetric capacity. Alternative charge-carriers, new chemistries, novel materials, and nanotechnologies have broadened the definitions of post-LIBs. However, great efforts are still to be undertaken in terms of establishing stable structures of the active materials and controlled reactions at the electrode/electrolyte interface to tackle the problems in inferior reversibility and performance stability.<sup>19</sup>

Since the main part of this thesis deals with sodium-ion batteries and magnesium-sulfur batteries, a detailed introduction on the working principles and material options of these two battery systems will be given in the following sections.

### 2.1.2 Sodium-ion batteries

Sodium-ion batteries (SIBs) were investigated at the same time as LIBs back in 1970s and 1980s. With the great success of LIBs, the research work on SIBs was almost paused for three decades. In recent years, SIBs started to regain people's attention considering the risks in increasing production cost of lithium due to the limited sources.<sup>27</sup> Detailed studies have demonstrated that replacement of lithium with sodium can lead to effective cost advantages.<sup>28</sup> This saving results not only from the metal substitution, but also from the possibility of using aluminum foils as both current collectors. In LIBs, a copper current collector must be used for the anode side as lithium forms a binary alloy with aluminum at a low potential, which does not apply for SIBs.<sup>29</sup> Moreover, sharing the same working principle and architectures as LIBs, SIBs have become the most widely investigated batteries among all post-LIBs so far.

Despite the similarities in synthetic strategy, intercalation/alloying/conversion chemistry and cell structures, two major differences have limited the applications of SIBs compared with LIBs: a higher standard reduction potential of Na (0.3 V higher than Li) and a larger ionic radius (0.3 Å

larger than Li). The higher potential of Na metal along with the higher reactivity with organic solvents made Na a less suitable candidate to be utilized as an anode material compared to Li.<sup>30</sup> Satisfactory reversible intercalation hosts are required to provide the channels and sites for larger Na<sup>+</sup> ion. Moreover, the host material needs to maintain a stable structure that can stand the volume change for long cycle life and reasonable high rate capability.

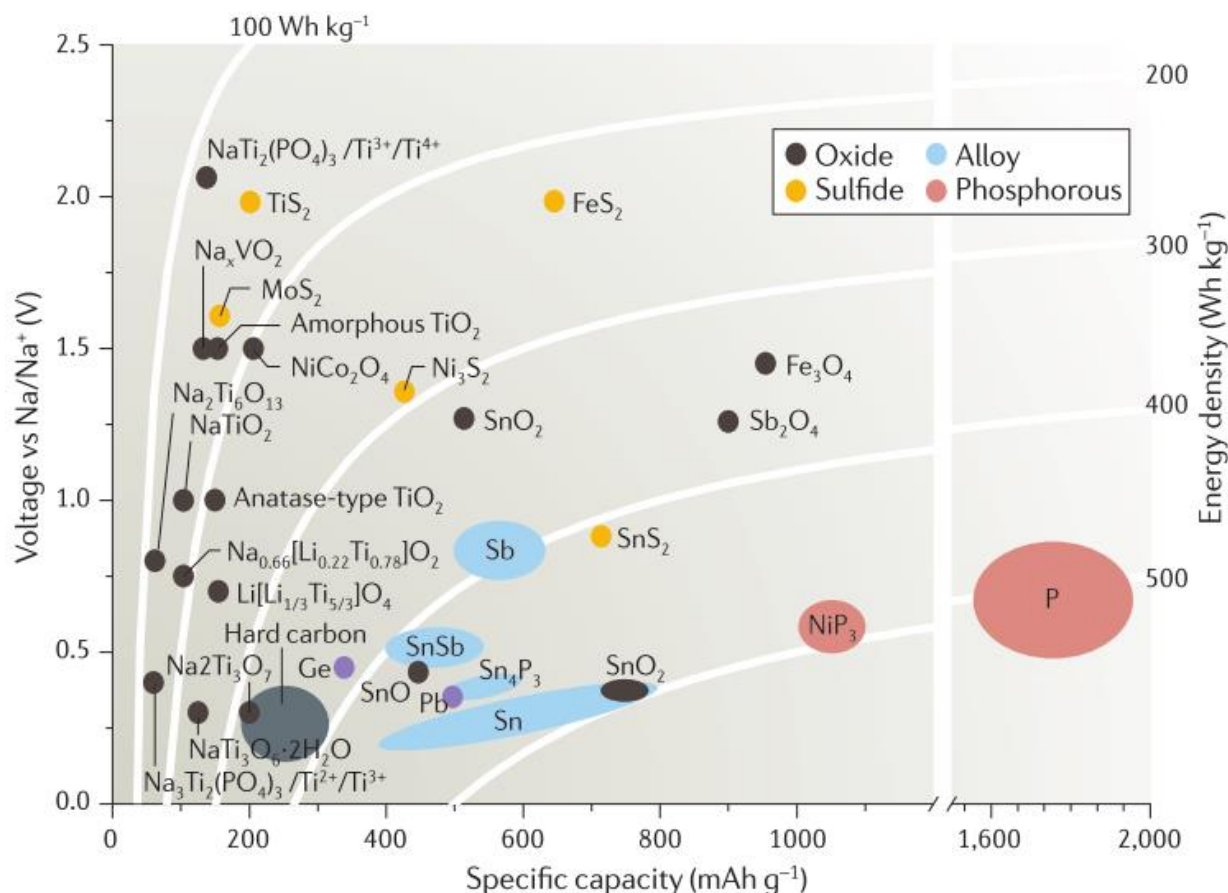


**Figure 2.3** Operation voltage vs. specific capacities of SIB anode materials. (Reprinted from ref.19, Copyright (2016), with permission from Springer Nature)

Possible anode candidates in SIBs are carbon-based materials, metal oxides (TiO<sub>2</sub>, Sb<sub>2</sub>O<sub>4</sub> and NiCo<sub>2</sub>O<sub>4</sub>) and intermetallic anode materials (Sn-Sb, Fe-Sb and Ni-Sn), as shown in Figure 2.3. Carbonaceous materials have played a fundamental role as anode materials in both LIBs and SIBs owing to their large abundance, low toxicity and acceptable price.<sup>31</sup> Graphite, as a layered material, which is the most commonly used anode material in commercial LIBs, cannot be applied to SIBs. Graphite intercalation compounds (GICs) are unable to be formed between Na and carbon (C) due

to a weakening ionic bonding with the decrease of ion size from Cs to Na in the alkali group. The even smaller lithium ion behaves as an exception due to a negative formation energy from a covalent component of Li-GICs.<sup>32</sup> Up to date, hard carbon, as a non-graphitic, graphene-containing structure, has received the most attentions and can deliver a reversible capacity of 210 – 335 mAh g<sup>-1</sup> depending on the precursors.<sup>33</sup>

Very different from the intercalation mechanism of Li<sup>+</sup> ions into graphite, Na<sup>+</sup> ions interact with carbonaceous material following a more complicated behavior. Taking hard carbon as an example, the discharge profiles when using Na as counter electrode are shown in Figure 2.4. Dahn *et al.* have first developed a detailed study of the Na storage mechanism in hard carbon.<sup>34</sup> There are two distinct steps including a first sloping region assigned to the insertion of Na<sup>+</sup> ions between the graphene layers and a second low-potential plateau close to the metal potential which is related to the adsorption of ions in the micropores.<sup>35</sup> Carbon nanostructures such as carbon nanofibers have also received tremendous attention due to a promising performance in flexibility, low cost, and structural stability. Moreover, it is suggested that the unique structure of these one-dimensional (1D) nanomaterials can offer short diffusion path for ionic and electron transport.<sup>36</sup>

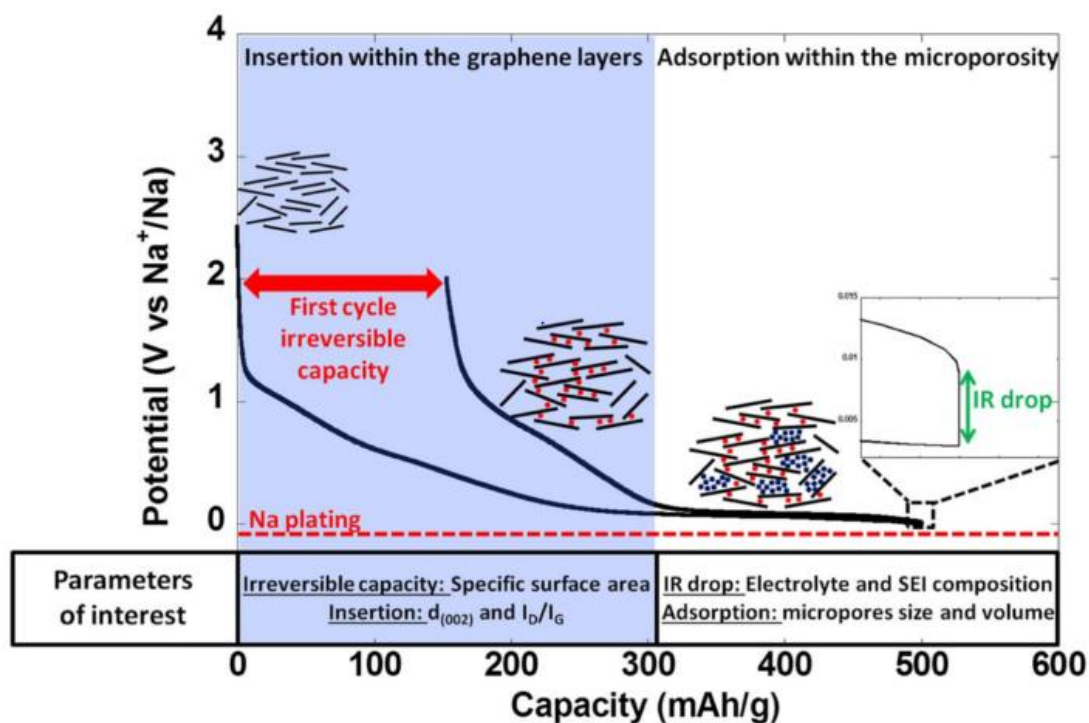


**Figure 2.4** Representative potential vs. capacity profile with step explanations for hard carbon against sodium metal. (Reprinted from ref.34 under CC BY license, with permission from IOPscience)

Fruitful research has resulted in many options for cathode materials for SIBs. However, aspects concerning limited cell voltage windows, low capacity at higher current rates and fast capacity decay are still hindering the process of finding a suitable cathode structure for SIBs. In Table 2.2 some common cathode materials are listed as examples with their electrochemical performances in sodium half cells. Layered materials can exhibit large specific capacities but insufficient structural stability during long-term cycling.<sup>19</sup> Among all the structures, metal-phosphate based, also named as phosphate polyanion based electrodes, are believed to be very promising cathode materials. Such polyanionic compounds are able to offer chemical and structural stability due to the stable P-O covalent bond that is responsible for the stability against oxygen release.<sup>37</sup> The use of low-cost iron (Fe) also avoids environmental unfriendly heavy metals such as cobalt (Co) and toxic elements such as vanadium (V).<sup>38</sup>

**Table 2.2** Summary of some representatives as cathode material with their electrochemical performances for SIBs.

Categories	Materials	Working voltage (V vs. Na <sup>+</sup> /Na)	Capacity (mAh g <sup>-1</sup> )	Rate	Retention (%, cycles)
Fluorides	NaFeF <sub>3</sub> <sup>39</sup>	1.5 - 4.5	170-181	0.01C	-
NASICON	Na <sub>3</sub> V <sub>2</sub> (PO <sub>4</sub> )/C <sup>40</sup>	2.7 - 3.7	107	0.1C	93% after 80
Phosphates	NaFePO <sub>4</sub> <sup>41</sup>	1.5 – 4.5	115	1C	91.3% after 800
Vanadium Oxides	Bilayered V <sub>2</sub> O <sub>5</sub> <sup>42</sup>	1.5 – 3.8	250	20 mA g <sup>-1</sup>	85% up to 350
Transition-Metal Oxides	Na <sub>x</sub> CoO <sub>2</sub> <sup>43</sup>	2.0 – 3.5	75.2	0.08C	93.6% up to 90
	NaNi <sub>1/3</sub> Co <sub>1/3</sub> Fe <sub>1/3</sub> O <sub>2</sub> <sup>44</sup>	2.0 - 4.2	165	0.05C	92%
Na <sub>0.44</sub> MnO <sub>2</sub> Tunnel	Na <sub>0.44</sub> MnO <sub>2</sub> nanowire <sup>45</sup>	2.0 – 4.0	110	0.1 A g <sup>-1</sup>	88% after 20

Among iron-based phosphate cathode materials, NaFePO<sub>4</sub> offers the highest theoretical capacity with up to 154 mAh g<sup>-1</sup> and a decent working voltage up to 4.5 V vs Na<sup>+</sup>/Na.<sup>46,47</sup> Olivine and maricite structures are two crystal structures of NaFePO<sub>4</sub>, of which the olivine structure is not thermodynamically stable and the maricite structure is inhibited from applications due to its electrochemical inactive nature.<sup>48-50</sup> Detailed structural sketches of olivine-type and maricite-type

$\text{NaFePO}_4$  are shown in Figure 2.5. The crystal structures of both olivine and maricite consist of slightly distorted  $\text{FeO}_6$  octahedra and  $\text{PO}_4$  tetrahedra.<sup>38</sup> The major difference for these two polymorphs is the  $\text{FeO}_6$  connecting patterns, which is corner-sharing in olivine phase and edge-sharing in maricite phase. A 1D  $\text{Na}^+$  diffusion channel can be clearly seen along the b-axis in the olivine phase whereas in maricite  $\text{NaFePO}_4$  it shows no cationic channels for  $\text{Na}^+$  movement. However, olivine  $\text{NaFePO}_4$  have to be accessed via chemical or electrochemical displacement methods from olivine  $\text{LiFePO}_4$  which is neither easy nor effective.<sup>41</sup>

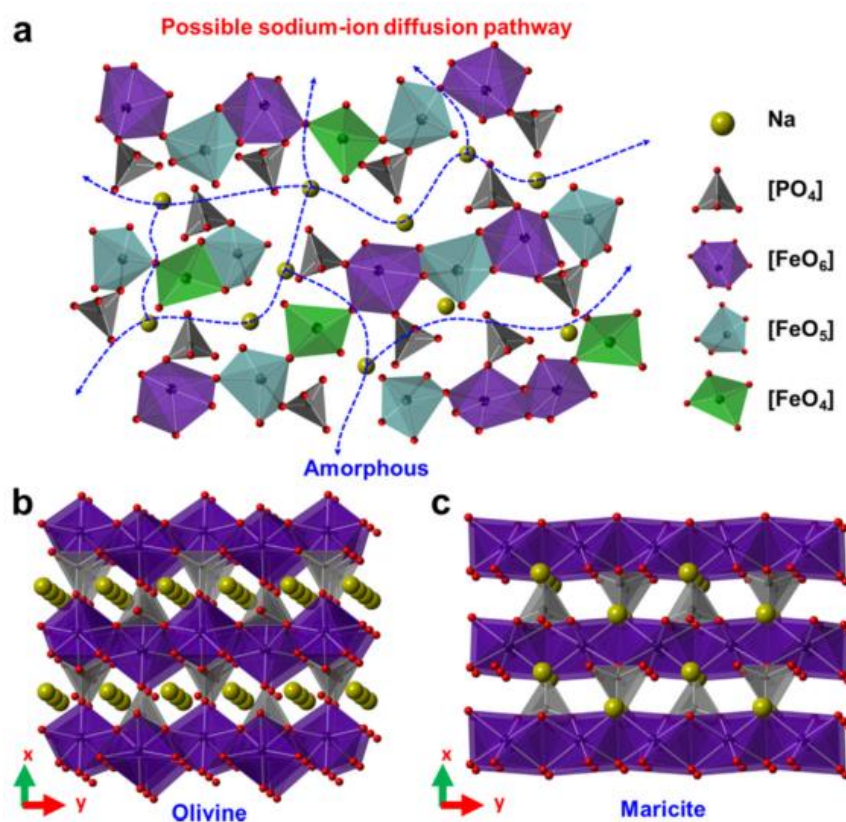


**Figure 2.5** Schematic illustrations for Na diffusive mechanism. (a) Possible sodium-ion diffusive pathways and atomistic structure for amorphous  $\text{NaFePO}_4$ ; Structural sketching diagrams of (b) olivine-type  $\text{NaFePO}_4$  and (c) maricite-type  $\text{NaFePO}_4$  (Reprinted from ref.41, Copyright (2020), with permission from Elsevier)

$\text{LiFePO}_4$  was also once believed incapable of performing as a cathode material due to its low electrical conductivity until approaches of particle size reduction and conductive material coating

were utilized for its commercialization.<sup>51</sup> Consequently, efforts in improving maricite  $\text{NaFePO}_4$ 's electrochemical performance such as downsizing and carbon addition have been undertaken to improve specific capacities of maricite  $\text{NaFePO}_4$ .<sup>41,52</sup> A successful attempt has been made with a voltage window of 1.5 – 4.5 V, a good high-rate performance and a long cycle retention over 90% after 800 cycles as listed in Table 2.2.<sup>41</sup> It was confirmed in most studies that maricite  $\text{NaFePO}_4$  was transformed into an amorphous phase including  $\text{FePO}_4$  and  $\text{Na}_x\text{FePO}_4$  upon charging to over 4.5 V.<sup>37,52,53</sup>

### 2.1.3 Magnesium-sulfur batteries

Because of the abundant reserve of multivalent elements (*e.g.* Mg, Al, and Ca) and their suppressed dendrite growth, the corresponding multivalent batteries are thought to be potential candidates as post-lithium energy storage solutions.<sup>21</sup> Unfortunately, the higher charge density of  $\text{Mg}^{2+}$  (120 C  $\text{mm}^{-3}$  vs. 52 C  $\text{mm}^{-3}$  for  $\text{Li}^+$ ) is accompanied by sluggish kinetics of  $\text{Mg}^{2+}$  solid-state diffusion or irreversible cation trapping in many crystal structures.<sup>54</sup> Oxide materials could provide the required energy densities, but  $\text{Mg}^{2+}$  cannot be intercalated into oxide materials as they tend to undergo conversion reactions, resulting in the formation of  $\text{MgO}$ .<sup>55,56</sup>

Alternatively, elemental sulfur is cost-effective and attractive as a positive electrode material due to its high capacity of 1670 mAh  $\text{g}^{-1}$ .<sup>57</sup> A high theoretical energy density (nearly 2600 Wh  $\text{kg}^{-1}$ ) combined with a lithium anode has drawn wide attentions for lithium-sulfur (Li-S) batteries. However, lithium erosion, volume expansion and safety issues from lithium dendrite growth have limited the performance of Li-S batteries.<sup>58</sup> Magnesium generally does not plate in a dendrite manner; thus, the replacement of Mg, which can behave as a more suitable metallic anode than Li, has gained substantial interest. Magnesium-Sulfur (Mg-S) batteries, offering a theoretical energy density of over 3200 Wh  $\text{L}^{-1}$  only experience a volume expansion of 24%, while in Li-S batteries the active material expands by 72% when  $\text{Li}_2\text{S}$  is formed.<sup>59</sup>

A schematic illustration of the working mechanism of Mg-S batteries is shown in Figure 2.6, where the cell is constituted by Mg as anode, S as cathode, separator and organic electrolyte. Electrons are released via the oxidization of Mg to  $\text{Mg}^{2+}$  and received by the reduction of sulfur into polysulfide (Mg-PSs) with various chain lengths. Stepwise, elemental sulfur on the cathode side is

first converted to long-chain polysulfides ( $\text{MgS}_8$ ), then cleaved into lower-order polysulfides ( $\text{MgS}_4$ ) and in the end transformed to  $\text{MgS}$  followed by a solid-state transition illustrated as:

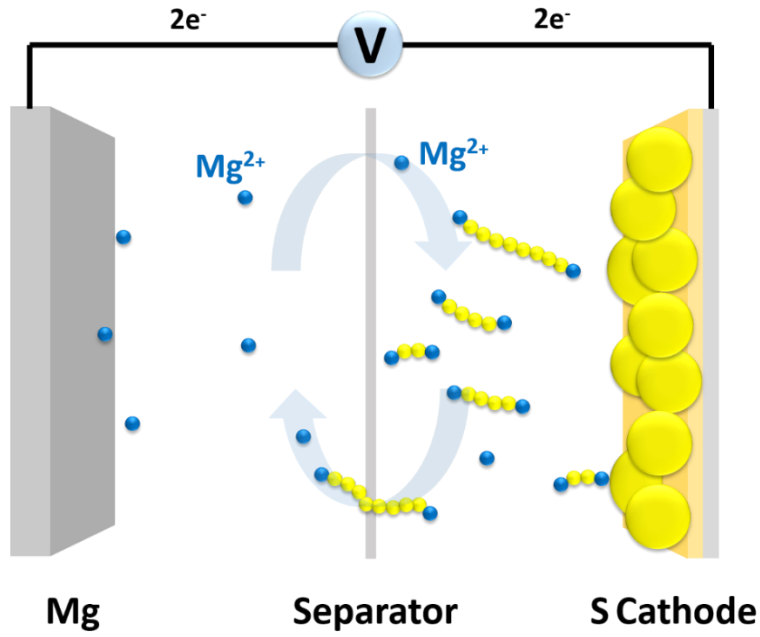
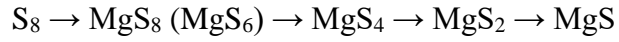


**Figure 2.6** Schematic illustration of Mg-S batteries working mechanism.

These steps can be described as:



With an anodic reaction:



Despite the advantages of Mg-S batteries, similar to Li-S batteries, the major challenge is to efficiently tackle the notorious “polysulfide shuttle effect”. Specifically, long-chain polysulfides ( $\text{S}_n^{2-}$ ,  $n = 4 - 8$ ), the first reduction products from sulfur ( $\text{S}_8$ ), can easily dissolve in the liquid electrolyte and diffuse to the anode resulting in serious anode passivation problems and hence a very fast capacity decay.<sup>60,61</sup> Mitigating this shuttling effect of polysulfides in Mg-S batteries is considered to be imperative to enhance the reversible discharge capacity and cycling stability.<sup>62</sup> Efforts in solving this problem by designing hierarchical sulfur hosts<sup>63,64</sup>, developing new electrolytes and/or additives<sup>59,65-67</sup>, as well as investigating anode/electrolyte interfaces<sup>68</sup> have been reported. Another important route to suppress polysulfide-shuttling is the modification of separators, which has received less attention so far.<sup>69,70</sup>

## 2.2 Electrospinning technology

Nanotechnology is offering new structures, different perspectives and novel breakthroughs in the field of energy storage technologies. One-dimensional nanostructures such as nanofibers and their composites have been broadly studied as anode materials, cathode materials, separators and even solid electrolytes in rechargeable batteries. Among all the methods of nanofiber fabrication methods, electrospinning, as a simple, versatile, controllable and cost-efficient technique, has been widely investigated to produce designed architectures in lithium-ion batteries and post-lithium-ion batteries.

### 2.2.1 Electrospinning principle

The basic principles of electrospinning are based on the uniaxial elongation of a viscous polymer solution under an electrostatic repulsive force.<sup>71</sup> In general, an electrospinning equipment consists of three parts (Figure 2.7): (1) a plastic syringe filled with electrospinning solution with a stainless needle; (2) a high voltage power supply; (3) a grounded collector.<sup>72</sup> The polymer solution is pumped to the surface of the needle edge shaping a pendant droplet at a constant rate, and the collector is placed at an adjusted distance away from the droplet. During electrospinning, a high electric field is applied in between the tip of the needle and the collector, charging the surface of

the polymer solution. When the electrostatic forces are significant to overcome the surface tension and viscosity of the fluid, a liquid jet will travel in the track of the collector. At this time, the charged droplet forms into a so called “Taylor cone” and its shape is influenced by the applied voltage as shown in Figure 2.7. Solvent evaporates on the way travelling to the collector leaving solid (as-spun) fibers depositing on the collector. A variety of parameters can be tuned to make an effect on the fibers development which made electrospinning a flexible and controllable method, see in section 2.2.2.

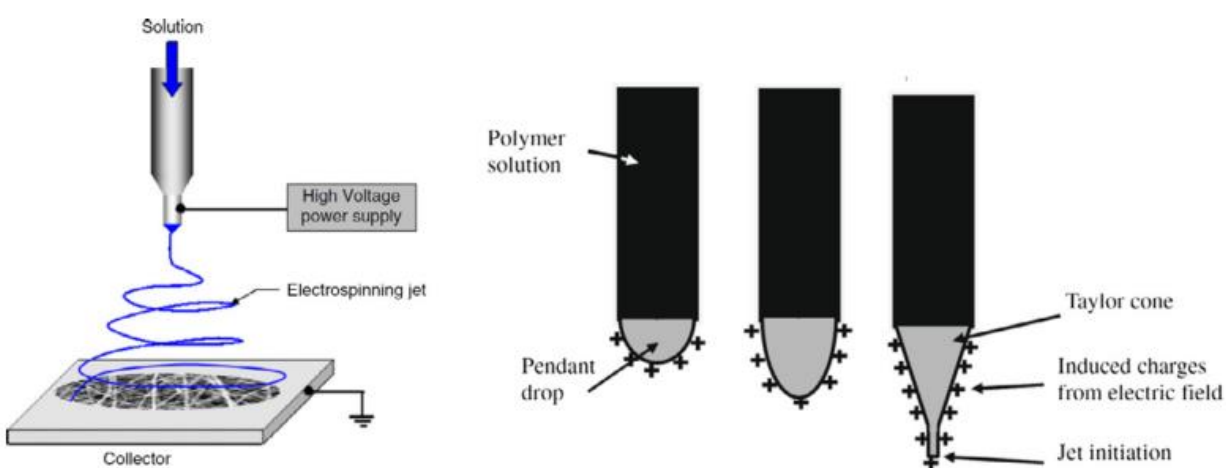


**Figure 2.7** Illustration of electrospinning device<sup>73</sup> (left) and the different tip forms used for electrospinning solution<sup>74</sup> (right). (Reprinted with permission from ref. 73 and 74, Copyright (2006) IOPscience and (2010) Elsevier)

## 2.2.2 Electrospinning of nanofibers

Nanofibers can appear in different macroscopic forms via electrospinning: random fibers, aligned fibers, core/shell fibers and composite fibers shown in Figure 2.8. Technically, the easiest fabricated fiber is a random fiber mesh by using a single nozzle of injecting needle and a flat metal plate or graphite paper collector.<sup>71</sup> New set-ups such as rotating collector with high speed are required for aligned fibers and a unique co-axial nozzle has to be utilized to synthesize core/shell fibers. The type of composite fibers can be formed mostly on the basis of random fibers with additives generated from a composite electrospun solution, to introduce certain functionalities in different research fields.

The properties and the micro-structures of as-spun fibers depend on (a) solution properties such as polymer molecular weight ( $M$ ), viscosity, solution conductivity and compositions; (b) operating parameters such as applied voltage, solution feed rate, spinning distance, environment temperature and humidity.<sup>75</sup> The values and significance of some important factors such as viscosity, surface tension, applied voltage and feeding rate are discussed in detail as follows.

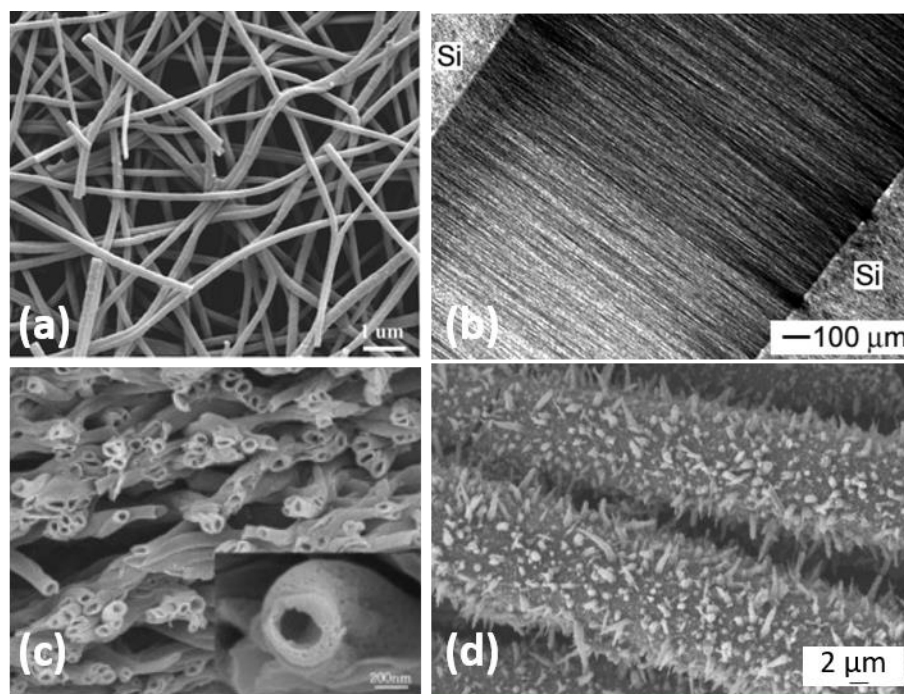


**Figure 2.8** Scanning electron microscopy images of different types of fibers: (a) random fibers<sup>76</sup>, (b) aligned fibers<sup>77</sup>, (c) core/shell fibers<sup>78</sup>, and (d) composite fibers<sup>79</sup>. (Reprinted with permission from ref. 76-79, Copyright (2013) WILEY-VCH, (2003) American Chemical Society, (2013) Elsevier B.V., and (2016) Elsevier B.V.)

### (i) Viscosity

Viscosity,  $\eta$ , of the precursor solution is among the most important factors in bead formation and diameter of the fibers. For a linear polymer, the Mark-Houwink-Sakurada equation can be written as:

$$\eta = k_1 M^a \quad (2.8)$$

where the constants “ $k_1$ ” and “ $a$ ” relay on the polymer, solvent and temperature. Also, viscosity can also influence fiber diameter  $d_f$ :

$$d_f = k_2 \eta^n \quad (2.9)$$

where  $k_2$  is a constant and  $n$  depends on the type of polymer precursor.

(ii) **Surface tension**

The surface tension of the electrospun solution should be kept low to diminish the required applied voltage. Typically, soft and smooth fibers are formed at low surface tension.

(iii) **Applied voltage**

The applied voltage will directly affect the form of charged polymer solutions. A higher voltage will pull the solution tip into a more threadlike shape and thus decrease the fiber diameters.

(iv) **Feeding rate**

The feeding rate of precursor solution directly determines the electrospinning efficiency. The flow rate needs to be taken into account when choosing the applied voltage and together they affect the fiber diameters.

(v) **Humidity**

Humidity can affect both the processability and morphology of fibers. In general, the humidity should be kept low to avoid possible reactions between highly hygroscopic polymers and moisture.

### 2.2.3 Electrospinning of carbon nanofibers

The ultimate structure and composition of nanofibers is powerfully reliant on precursors, in most of the cases polymers are solubilized in a solvent. The precursors can be classified into two categories, which are host precursor acting as a framework and guest precursor offering void space. Some commonly used precursors are poly(vinyl pyrrolidone) (PVP), polystyrene (PS), poly(methyl methacrylate) (PMMA), polyacrylonitrile (PAN), poly(vinyl acetate) (PVAc), poly(ethylene oxide) (PEO), and poly(vinylidene fluoride) (PVdF), dissolved in one or more than one solvent.<sup>36</sup> The polymeric fibers then will undergo post treatments such as high temperature treatments and chemical activations depending on the targeted structures and function of the nanofibers.

Carbon nanofibers (CNFs) have received a vast interest in the applications in energy storage devices thanks to its high electrical conductivity. Two main methods can be applied for the production of carbon fibers with a submicron or nanometer dimension: vapor growth and spinning.<sup>80</sup> In the approach of vapor phase growth, graphitic carbon nanofibers are grown from carbon-containing gases by using metallic catalysts.<sup>81,82</sup> However, this method requires expensive equipment and the CNFs are relatively short and difficult to be aligned or assembled. Electrospinning, on the contrary, provides a straightforward method to produce CNFs at submicrometer (usually 100 – 1000 nm) scale with a controllable and scalable manner which has gained an enormous interest in the past decade.<sup>83</sup>

Polyacrylonitrile (PAN) is one of the most common polymer precursors for constructing electrospun CNFs with a high carbon yield of 50%. Moreover, PAN fibers are thermally stable due to the nitrile groups forming a ladder structure with adjacent groups (Figure 2.9). A subsequent two-step thermal treatment is required to convert the polymeric fibers into CNFs. First, a stabilization step needs to be performed at low temperature (below 400 °C) in air, during which the cyano side groups of PAN form cyclic rings by a dehydrogenation process.<sup>84</sup> In the second step, high temperature carbonization under inert gas will be performed to obtain the final CNFs product. The carbonization temperature can be adjusted to control the carbon structures and hence the mechanical and electrochemical properties of carbon nanofibers.

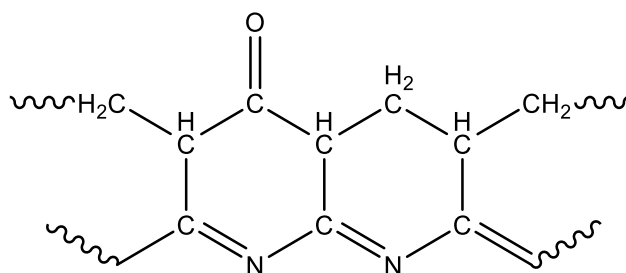


**Figure 2.9** Proposed ladder structure of PAN.

Unlike the conventional CNF production methods, single CNFs from electrospun PAN can exhibit weak mechanical strengths. PAN polymer chains will relax when deposited on the collector and start to lose their initial orientation after some time. The loss of macromolecular orientation in the final electrospun PAN may lead to some structural imperfections and inferior mechanical properties of the final CNFs.<sup>83,85</sup> However, the microstructures of CNFs such as porous structures can be tuned by modifying the precursor solutions and electrospinning parameters.<sup>86</sup> Additionally,

composite nanofibers consisting of CNFs and other functional materials have been fabricated and studied via electrospinning by introducing functional material's precursors into the electrospinning solutions or directly combining the materials into the electrospun CNFs. In the following section, applications of electrospun nanofibers, carbon nanofibers and their composite materials for post-LIBs will be introduced.

## **2.3 Applications of electrospinning in post-lithium-ion batteries**

The method of electrospinning can be utilized in a wide range of components for energy storage applications such as electrode materials, separators and solid electrolytes. A variety of material options are offered via electrospinning based on the varieties in precursors and the following processing. Target materials explored by electrospinning can be divided into the following categories: (1) nanoparticles synthesis; (2) nanofibers synthesis; (3) composite material synthesis and (4) modifications such as coating and doping. Challenges in post-LIBs concerning poor cycle stability caused by factors such as unstable electrode structures for bigger ions insertion/deinsertion, volume change, shuttle effect in sulfur batteries are yet to be solved. Therefore, electrospinning can provide new nanomaterials options and possible modifications, hence introduce appealing enhancement for post-LIBs performance.

### **2.3.1 Applications in anode materials for SIBs**

Among the alternatives for graphite as anode material for SIBs, many options can be prepared by electrospinning into the forms of nanostructures. First, for nanoparticles synthesis, starting materials are dissolved in a polymer solution (aqueous or organic solvent) and the crystalline nanoparticles are synthesized during subsequent calcination along with the decomposition of the polymer.<sup>87,88</sup> Second, carbon nanofibers have been widely applied as anode materials itself or as conductive substrates to further improve the electrochemical performance of active materials. In many cases either PVP or PAN is used as precursor to generate CNFs serving as both supporting skeleton and electrically conductive matrix.<sup>87,89</sup> PVP is often used in metal oxides/carbon composites for neat metal oxides with a low carbon yield of 15% while PAN is more favored in CNFs fabrications and the CNFs hybrid materials where a high carbon yield is needed. A representative synthesis route of carbon nanofibers modified anode material is shown in Figure 2.10 by Xiong *et al.* where nanosized TiO<sub>2</sub> is embedded in the conductive CNFs. An improved

long cycle performance with nearly 100% capacity retention over 1000 cycles was achieved with a high redox capacity of 302 mAh g<sup>-1</sup> at a high current of 2 A g<sup>-1</sup>.<sup>89</sup>

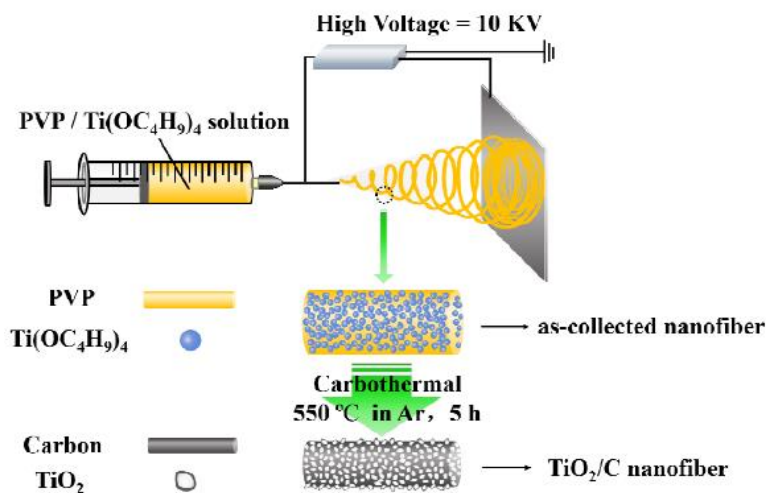


**Figure 2.10** Schematic synthesis route for the TiO<sub>2</sub>/C nanofibers (Reprinted with permission from ref. 89, Copyright (2016) American Chemical Society)

Some other options of electrospun anode materials for SIBs are listed in Table 2.3.<sup>90</sup> In most of the cases, carbon is added to increase electrical conductivity and buffer the volume expansion. Moreover, carbon nanofibers can offer a shorter diffusion pathway relative to the powder materials and a larger number of ion sites. In spite of the significant research of carbon nanofiber-based anodes, the mechanism of sodiation and desodiation in CNFs still remains a complex subject. A high surface area can facilitate a faster ion diffusion but also lead to more side reactions. A careful analysis of the CNFs structure and its effect on the mechanism in sodium ion storage is worth being investigated.

Besides the flexibility in material preparations, there are some other advantages that can be used by electrospinning compared to a conventional slurry electrode. Binder-free and self-standing are two common concepts where the usage of passive materials such as binder and collectors can be excluded which can increase the overall cell energy density and might reduce the cost. In a traditional battery assembly, binders, mostly PVdF, are used to fix the conductive agent and the active materials on the current collector by a coating method.<sup>91,92</sup> However, in the cases of some

**Table 2.3** Examples of various electrospun anode materials for SIBs application.

Materials	Precursor	Process	SIB Performance
Hard Carbon <sup>93</sup>	PVC/THF, DMF (3.5 : 6.5)	700 °C in Ar	211 mAh g <sup>-1</sup> after 221 cycles at 12 mA g <sup>-1</sup>
N – doped CNFs <sup>94</sup>	Urea/PAN/DMF	250 °C – 2 h in air 700 °C – 3 h in N <sub>2</sub>	201.5 mAh g <sup>-1</sup> after 1000 cycles at 50 mA g <sup>-1</sup>
Fe <sub>2</sub> O <sub>3</sub> @C <sup>95</sup>	Fe(NO <sub>3</sub> ) <sub>3</sub> · 9H <sub>2</sub> O DMF/PAN	260 °C – 2 h in Ar 290 °C – 2 h in Ar/H <sub>2</sub>	345 mAh g <sup>-1</sup> after 1000 cycles at 2000 mA g <sup>-1</sup>
Free-standing Porous CNFs <sup>96</sup>	PAN, triblock copolymer Pluronic F127/DMF	280 °C – 3 h in air 1000 °C in Ar	266 mAh g <sup>-1</sup> after 100 cycles at 50 mA g <sup>-1</sup>
Bi/C nanofibers <sup>97</sup>	BiCl <sub>3</sub> /Bi(NO <sub>3</sub> ) <sub>3</sub> /DMF/PAN	350 °C – 2 h in Ar 650 °C – 3 h in Ar/H <sub>2</sub>	273.2 mAh g <sup>-1</sup> after 500 cycles at 100 mA g <sup>-1</sup>
SnSb@C <sup>87</sup>	SnO <sub>2</sub> NPs, Sb <sub>2</sub> O <sub>5</sub> NPs/PMMA, PAN/DMF	280 °C – 5.5 h in air 700 °C – 3 h in air	356 mAh g <sup>-1</sup> after 200 cycles at 500 mA g <sup>-1</sup>
Li <sub>4</sub> Ti <sub>5</sub> O <sub>12</sub> @C <sup>98</sup>	Li(ac) <sub>2</sub> · H <sub>2</sub> O, TiO(acac) <sub>2</sub> /PVPV/EtOH	400 °C – 2 h in Ar 800 °C – 5 h in Ar	163 mAh g <sup>-1</sup> after 100 cycles at 35 mA g <sup>-1</sup>
TiO <sub>2</sub> @C <sup>99</sup>	Ti (OC <sub>4</sub> H <sub>9</sub> ) <sub>4</sub> /PVP/C <sub>2</sub> H <sub>5</sub> OH and CH <sub>3</sub> COOH (10:1 by wt)	280 °C – 5.5 h in air 450, 550, 650 and 750 °C	68.2% ICE after 100 cycles at 30 mA g <sup>-1</sup>

novel materials for post-LIBs, the weak interfacial interaction between binders and active material can result in particle self-aggregation and even separation from current collector.<sup>100</sup> Binder-free electrodes, facilitated by the network within electrospun carbon nanofibers, show potentials in the improved ionic and electronic transportation, cycling performance and energy density. Instead of conventional aluminum and copper foils, carbon material such as carbon paper and carbon fiber mats were also investigated as current collectors with superb electronic conductivities.<sup>101,102</sup> Self-standing (also named as free-standing) electrodes based on electrospun CNFs are expected to bring more flexibilities in both manufacturing and cost savings.<sup>102,103</sup>

### 2.3.2 Applications in cathode materials for SIBs

Unsatisfied performances in cathode materials concerning practical capacity, cycle stability and rate capability have limited the real-time applications of SIBs. The main reason lies in the sluggish electrode kinetics due to the large radius of  $\text{Na}^+$  ion.<sup>104</sup> Therefore, modification and optimization of cathode materials are essential for achieving high-performance SIBs. For example, in NASICON-type cathode material, the poor electronic conductivity of phosphates makes it difficult to achieve a high capacity close to their theoretical values.<sup>88</sup> Efficient strategies to overcome these shortcomings are mainly focused on designing nanomaterials or/and providing conductive coatings. Electrospinning, as introduced above, is able to realize nanostructures fabrication with carbon additives. Many studies have been reported with the help of electrospinning to tune cathode active materials in different morphologies and introduce carbon coatings and thus enhance the overall

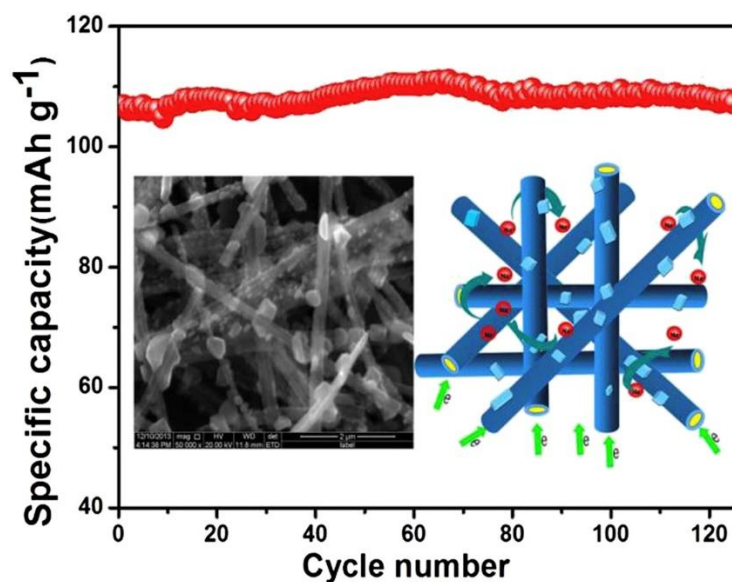


**Figure 2.11** Morphology and cycle performance of  $\text{Na}_3\text{V}_2(\text{PO}_3)/\text{C}$  nanofiber cathode material. (Reprinted with permission from ref. 108, Copyright (2015) Elsevier)

electrochemical performance.<sup>105–107</sup> Wu and co-workers synthesized  $\text{Na}_3\text{V}_2(\text{PO}_3)$  nanoparticles anchored on and encapsulated in carbon-based nanofibers via electrospinning.<sup>108</sup> As presented in Figure 2.11, the nanoparticles are embedded among the nanofiber structures. The composite cathode showed a reversible capacity of  $107.2 \text{ mAh g}^{-1}$  after 125 cycles at a current density of  $0.2\text{C}$ .

We can see the interconnected structure of nanofibers from the SEM image, which was proposed to facilitate the diffusion of  $\text{Na}^+$  ions and thus increase the overall electrical conductivity.

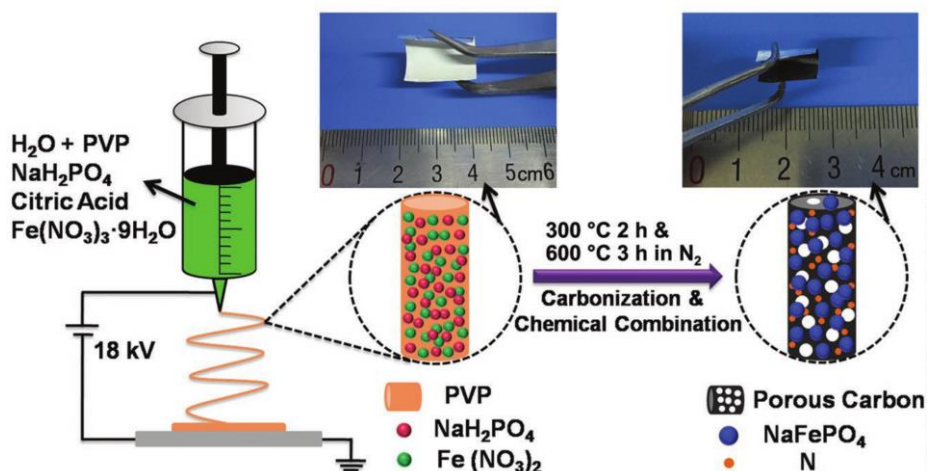


**Figure 2.12** Schematic synthesis route of the maricite  $\text{NaFePO}_4$  nanodots in N-doped carbon nanofibers ( $\text{NaFePO}_4@C$ ) (Reprinted with permission from ref. 53, Copyright (2018) John Wiley and Sons)

Some representative cathode composite materials prepared by electrospinning are shown in Table 2.4 listed with a variety of precursors and heating processes. Maricite  $\text{NaFePO}_4$  has been mentioned to have a lack of  $\text{Na}^+$ -ion pathways due to a “closed” framework.<sup>47</sup> Fan’s group has utilized electrospinning for nanoparticle synthesis realizing an embedding of  $\text{NaFePO}_4$  nanodots ( $\approx 1.6$  nm) in N-doped carbon fibers to obtain a high reversible capacity of  $145 \text{ mAh g}^{-1}$  at  $0.2C$  with a schematic synthesis route shown in Figure 2.12.<sup>53</sup> In most of the reported work, water was used as solvent in the cathode synthesis where the majority of inorganic salts can be dissolved in. The choice of solvent leads to a more often utilization of PVP as polymer matrix than PAN, which can only be dissolved in a limited number of solvents such as DMF. CNFs have been demonstrated to be good conductive additives and improve the electronic conductivity and sodium-storage performance.<sup>88,108</sup> A direct carbon coating from PAN precursor can also offer promising chances for material modifications.<sup>109</sup> Bachtin *et al.* prepared  $\text{LiFePO}_4$ /carbon composite with an improved overall electrical conductivity and cycle stability via a direct electrospinning from the hybrid solution of  $\text{LiFePO}_4$  and polyacrylonitrile (PAN) resulting in a carbon decorated  $\text{LiFePO}_4$  after carbonization of PAN.<sup>109</sup>

**Table 2.4** Examples of various electrospun cathode materials for SIBs application.

Materials	Precursor	Content	Process	SIB Performance
Na <sub>3</sub> V <sub>2</sub> (PO <sub>3</sub> )/C nanofiber <sup>108</sup>	NaH <sub>2</sub> PO <sub>4</sub> , NH <sub>4</sub> VO <sub>3</sub> and citric acid, PVP/water	carbon 9.13 wt%	300 °C 3h 800 °C 8h in Ar	107.2 mAh g <sup>-1</sup> after 125 cycles at 0.2C
Na <sub>3</sub> V <sub>2</sub> (PO <sub>3</sub> )/C nanofiber <sup>88</sup>	NaH <sub>2</sub> PO <sub>4</sub> , NH <sub>4</sub> VO <sub>3</sub> and citric acid, PEO/water	carbon 18 wt%	500 °C and 800 °C in Ar	101 mAh g <sup>-1</sup> at 0.1C
Na <sub>2/3</sub> (Fe <sub>1/2</sub> Mn <sub>1/2</sub> )O <sub>2</sub> nanofibers <sup>110</sup>	sodium acetate, iron nitrate, manganese acetate, DMF/PVP	Not available	Stepwise up to 900 °C 2 h in air	166 mAh g <sup>-1</sup> after 80 cycles at 0.1C
NaVPO <sub>4</sub> F/C nanofibers <sup>111</sup>	NH <sub>4</sub> VO <sub>3</sub> , H <sub>2</sub> C <sub>2</sub> O <sub>4</sub> , NH <sub>4</sub> H <sub>2</sub> PO <sub>4</sub> , NaF, PVP/water	carbon 2.58 – 6.07 wt%	400 °C 2 h and 750 °C 4 h in Ar	126.3 mAh g <sup>-1</sup> at 1C
Maricite NaFePO <sub>4</sub> nanodots <sup>53</sup>	NaH <sub>2</sub> PO <sub>4</sub> , citric acid, Fe(NO <sub>3</sub> ) <sub>3</sub> ·9H <sub>2</sub> O, PVP/water	NaFePO <sub>4</sub> 70.2 wt%	300 °C 2 h 600 °C 3 h in N <sub>2</sub>	140 mAh g <sup>-1</sup> for 300 cycles at 20 mA g <sup>-1</sup>

### 2.3.3 Applications in modified separators for Mg-S batteries

Among the battery components, the separator plays an important role in safety and long-term performance though it does not directly participate in battery reactions. Improvements of thermal stability, mechanical property and porosity for higher ion transportation efficiency are still needed to fulfill the higher standards of battery performance and to adapt to more diverse materials for post-LIBs. Electrospun separators can be divided into five major types: monolayer separator, multilayer separator, composite separator, modified separator and gel polymer electrolyte (separator).<sup>112</sup> Polymer electrospun membranes can be directly used as separators such as PVdF, PAN and polyimide (PI) in the form of nanofibers. Besides, it is noteworthy to mention that modified separators can also lead to improved properties such as suppressing polysulfide-shuttling in Li-S and Mg-S batteries and hence improve cell performance.<sup>69,70</sup>

The criteria for an ideal separator for sulfur batteries does not only depend on an outstanding ionic conductivity but also the function to block “shuttle effect” of polysulfide.<sup>113</sup> Electrospinning can be applied in separator preparations for metal sulfur batteries in multiple folds: polymer separators

with functional groups, doped-separator with additives, and an interlayer between cathode and separator as an extra shield for polysulfide. As mentioned, the shuttle effect from dissolved polysulfide is one of the biggest obstacles in the development of metal sulfur batteries. To suppress this shuttle effect, functionalized separators can act in either one or more of the following modes: 1) physically or chemically anchoring polysulfides;<sup>114–116</sup> 2) electrostatic repulsion of polysulfides;<sup>117–119</sup> 3) adding up to the upper current collector and thus increasing the utilization of sulfur species.<sup>120–122</sup> For example, Zhou *et al.* have developed a “polysulfide-phobic” separator in Li-S battery by immobilization of two-dimensional VOPO<sub>4</sub> sheets onto a PP membrane through suction filtration. The cell implementing such a VOPO<sub>4</sub> layer showed a high reversible capacity of 840 mAh g<sup>-1</sup> after 300 cycles with capacity retention of 75.3%, while a battery with pristine PP separator in comparison, maintained only a capacity of 310 mAh g<sup>-1</sup> after 300 cycles with capacity retention of merely 28.1%. The enhanced battery performance was attributed to the vanadium-rich layer that formed intramolecular V-S interaction to efficiently block the shuttling of polysulfides.

It is worth to mention that a vanadium-rich functional separator based on polyoxovanadates (i.e. highly redox-active vanadium-based polyoxometalates) has also shown potentials in alleviating of polysulfide-shuttling.<sup>123</sup> Polyoxometalates (POMs) are based upon metal oxide building blocks with a general formula [MO<sub>x</sub>]<sub>n</sub>, where M=Mo, W, V and x=4~7. Precisely, POMs are one family of redox-active molecular metal oxides with vast structural, chemical and redox tunability, which have shown promising performances in lithium-ion batteries.<sup>124–127</sup> Heteropolyanions, the most frequently investigated subset of POMs, are metal oxide clusters including heteroanions such as SO<sub>4</sub><sup>2-</sup> and PO<sub>4</sub><sup>3-</sup>.<sup>128,128</sup> The breakthrough “Molecular Cluster Battery” hypothesis of POMs was proposed by Awaga *et al.*,<sup>129,130</sup> and the following developments of POMs as lithium-ion battery materials are mainly based on heteropolyanions, including the archetypal Keggin [XM<sub>12</sub>O<sub>40</sub>]<sup>n-</sup><sup>131,132</sup> and Wells-Dawson [X<sub>2</sub>M<sub>18</sub>O<sub>62</sub>]<sup>n-</sup><sup>133,134</sup> anions (where M=W or Mo, X is a tetrahedral template). Whereas decavanadate [V<sub>10</sub>O<sub>28</sub>]<sup>n-</sup>, a typical type of isopolyanions (POM subset without internal heteroatom/heteroanion), is regarded to possess high theoretical specific capacity, owing to low atomic weight in contrast to traditional Mo-based (95.95 g mol<sup>-1</sup>) and W-based (183.84 g mol<sup>-1</sup>) isopolyanions. A reversible transfer of 10 electrons by a single [V<sub>10</sub>O<sub>28</sub>]<sup>n-</sup> molecule, accompanied by reduction of all ten V<sup>5+</sup> centers to V<sup>4+</sup>, gives a theoretical capacity of over 200 mAh g<sup>-1</sup>.<sup>135</sup> The research of using POM in enhancing the performance of Metal-Sulfur batteries is still at an infant phase.

### 3 Scope and objectives

In this work, the applications of electrospinning in post-lithium-ion batteries are to be developed in three different aspects: anode material for sodium-ion batteries, cathode material for sodium-ion batteries and modified separator for magnesium-sulfur batteries. The main scope is focused on electrode materials and modified separators prepared mainly via electrospinning, and their electrochemical performance and fundamental mechanisms.

*(1) Studying the mechanism of self-standing carbon nanofibers as anode material for SIBs:*

Carbon nanofibers and their composites have been widely researched as anode material in lithium-ion batteries and sodium-ion batteries. Unlike hard carbon, which usually has to undergo high temperature (over 1000 °C) treatment, CNFs carbonized at lower temperatures can also offer Na<sup>+</sup> intercalation sites and thus function as anode materials for SIBs. With a more amorphous phase and disordered structure compared to hard carbon, CNFs may interact with Na<sup>+</sup> ions following a very different mechanism. Self-standing CNFs were synthesized via electrospinning from PAN / *N,N*-dimethylformamide (DMF) without additional collectors and binders. Effects of carbonization temperatures in low range (under 1000 °C) on electrochemical performance are investigated. A detailed study on morphology and structural changes of such self-standing CNFs and its electrochemical performances during cycling was carried out.

*(2) Self-standing NaFePO<sub>4</sub> / carbon nanofiber cathode for SIBs:*

Self-standing composite cathode materials can be realized in a network of carbon nanofibers via fabrication from the electrospinning. NaFePO<sub>4</sub>, as a promising cathode for SIBs, its two different structures and the corresponding limitations have been introduced. To solve the issues like insufficient diffusion channels for Na<sup>+</sup> ions in maricite structure, efforts with carbon coatings and downsizing to nanostructures have proven successful. Aided by electrospinning, a new composite electrode material from maricite NaFePO<sub>4</sub> and CNFs was prepared. In this way, not only improved electrical conductivity will be introduced, the CNFs can also function as the current collector realizing a self-standing and collector-free electrode material with potentials to be utilized in flexible, soft and wearable batteries. Herein, I synthesize self-standing NaFePO<sub>4</sub> / carbon nanofibers (NaFePO<sub>4</sub>/CNF) electrodes via electrospinning of ball-milled NaFePO<sub>4</sub> and PAN / DMF solution. A comprehensive investigation of the electrode morphology, structure, and

electrochemical performance before and after cycling is conducted. The study of such a composite electrode material will enlighten the knowledge on: (a)  $\text{Na}^+$  ion transfer mechanism in carbon containing cathode material, (b) the capacitive contribution of carbon content and nanomaterials in SIBs, and (c) potentials of such self-standing, collector-free, binder-free electrodes in the field of energy storage systems.

*(3) Polyoxometalate/carbon-based modified separator for Mg-S batteries:*

Modified separators using electrospun material coating layers have proven effective to substantially moderate the “shuttle effect” of polysulfide species in metal sulfur batteries.<sup>113</sup> In this part of work, a “polysulfide-phobic” coating was prepared by electrospinning a mixed solution of decavanadate clusters (POM), Super P carbon and PVdF on a commercial glass fiber separator. Mg-S cells are assembled with the modified separator and the electrochemical performances are compared to the ones using pristine separators. Battery setups are assembled with Ketjen black / S composite as cathode, neat  $\text{Mg}[\text{B}(\text{hifp})_4]_2$  ( $\text{Cl}^-$  free, no-additive-containing) dissolved in DME as electrolyte (0.3 M) as well as pure Mg foil as anode. For this, the functionality of the modified separator to block polysulfides is expected to be more reliable with less inactive components. In addition, in order to investigate the mechanism of polysulfide-shuttling suppression, the as-fabricated POM-based separator is immersed in synthesized magnesium polysulfide solution. X-ray photoelectron spectroscopy (XPS) is conducted to detect the interaction between polysulfide species and decavanadate clusters.

## 4 Mechanisms of carbon nanofibers as anode materials for SIBs

### 4.1 Experimental part

#### 4.1.1 Material preparation

Polyacrylonitrile (PAN) ( $M_w=150,000$ , Aldrich) powder was first dried in a drying oven at  $80\text{ }^\circ\text{C}$  for 12 hours before being dissolved in *N,N*-dimethylformamide (DMF) (99.9% GPR Rectapur, VWR Chemicals) solvent. The polymer was dispersed in DMF in a 20 mL glass vial and got dissolved gradually under strong stirring on a magnetic stirrer with a weight percentage of 10 wt% for 24 hours. A homogeneous and viscous polymer solution was obtained and then loaded into a 1 mL syringe attached to an assembled injecting needle with an inner diameter of 0.8 mm. Normally, about 1.1 – 1.2 mL solution was added to allow a practical 1 mL spinning amount with filling the gap in the needle attachment. The syringe was set in an ultrasonic cleaner for 10 minutes to get rid of possible existing bubbles. A climate-controlled electrospinning apparatus (EC-CLI, IME Technologies) was utilized, where the temperature and humidity can be fixed to provide a stable environment for fiber formation. The electrospinning temperature was set to  $25\text{ }^\circ\text{C}$  and the relative air humidity ( $\text{H}_2\text{O}$ ) to 20%. The needle tip was placed 15 cm away from collector, which was covered by a sheet of smooth and clean aluminum foil. A high voltage of 13 kV was first applied to form a steady Taylor cone and gradually was increased to 16.5 kV keeping a steady polymer solution shape at the tip of the needle. Electrospun solution was pumped with a flowing rate of 0.5 mL/h using an electrical pump (11 Elite, Harvard Apparatus). A total 2 mL solution was spun onto one fiber mat and then two fiber mats were attached on the surface of each other. The combined fiber mats were then placed in between two pieces of smooth glass plates after drying at  $80\text{ }^\circ\text{C}$  for 6 hours. The glass plates can keep the dimensional stability of the fiber mats during the following heating treatment processes.

The first step of heating treatment was a stabilization procedure where the glass plates with the fiber mats in between were placed in a calcination furnace in air. Heating program was set with segments: 2 hours at  $180\text{ }^\circ\text{C}$  with a heating rate of  $120\text{ }^\circ\text{C/h}$  from room temperature, 12 hours at  $240\text{ }^\circ\text{C}$  with  $60\text{ }^\circ\text{C/h}$ , and 4 hours at  $280\text{ }^\circ\text{C}$  with  $120\text{ }^\circ\text{C/h}$ . The stabilized fiber mats were then punched into round shape with a diameter of 12 mm. The second heating process was carbonization

carried out in a horizontal furnace under the atmosphere of argon at a flow rate of 0.55 l/min. The stabilized electrodes were placed in between ceramic plates with carbon mats on top serving as surface protections. The carbonization was performed at different temperatures of 600 °C, 800 °C, and 1000 °C for 3 hours with a heating rate of 5 °C/min. Samples obtained were named as CNF\_600, CNF\_800, and CNF\_1000.

Details on electrospinning equipment, syringe setup, and operating procedures have been introduced in the reference.<sup>136</sup>

#### 4.1.2 Material characterization

##### *SEM*

The morphology of all the samples was observed with a Merlin thermal field emission scanning electron microscope (FE- SEM) (Carl Zeiss SMT AG). Carbon tapes were used as substrates. Self-standing CNF anodes were directly attached on the carbon tape without any coating. Cycled samples were obtained after cell disassembly, thoroughly washed with DMC, and then dried under vacuum at 65 °C in a glovebox for at least 2 hours prior to the test. A vacuum transport tube was used for transferring the cycled *ex situ* samples.

##### *Raman Spectroscopy*

Raman measurements were performed on a LabRam Evolution HR instrument (HORIBA Jobin Yvon) applying a 532 nm wavelength laser. Each spectrum was taken as the average of three 10-second accumulations. The peaks were fitted with the Labspec 6 Spectroscopy Suite Software following a Gauss-Lorentz function. *In situ* Raman was carried out on the same instrument utilizing a coin cell with glass window. The cell was being discharged at a current density of 5 mA g<sup>-1</sup> and charged at a current density of 10 mA g<sup>-1</sup>. Spectra were taken every 10 minutes with an autofocus function at the beginning of each measurement. The baseline of each spectrum was subtracted and the intensities were normalized to a maximum value of 100.

### 4.1.3 Electrochemical performance

The self-standing CNF anodes were dried under 65 °C for 8 hours prior to use. Coin cells (CR2032) were assembled with sodium metal as the counter/reference electrode, glass fiber (Whatman, GF/D), ( $\varnothing = 17$  mm) as the separator and 0.8M NaClO<sub>4</sub> in EC:DEC 1:1 w:w as electrolyte. The electrospun fiber mats were punched into the right size ( $\varnothing = 12$  mm) after stabilization and before carbonization. The self-standing electrodes were directly assembled in the coin cells without any additional current collector. Galvanostatic cycling with potential limitations, cyclic voltammetry (CV) and electrochemical impedance spectroscopy (EIS) were carried out on a multichannel potentiostat (VMP3, Bio-Logic). The voltage ranges of galvanostatic cycling and CV tests are 0.01 V - 2.0 V vs. Na<sup>+</sup>/Na. EIS tests were carried out at charged state (2.0 V) and discharged state (0.01 V) with an alternating current signal of a 5 mv amplitude ranging from 1MHz and 0.01Hz. The calculation of the specific capacity of CNF electrodes is based on the mass of carbon determined from C/H/N/S analysis. CVs were carried out under different scan rates: 0.1, 0.25, 0.5, 1, 2.5, 5, 10, 25, 50, and 100 mV s<sup>-1</sup>. Galvanostatic cyclings were done with a current density of 100 mA g<sup>-1</sup>. Rate capabilities were carried out at current densities of 50, 100, 200, 500 mA g<sup>-1</sup>, 1 A g<sup>-1</sup> and again at 50 mA g<sup>-1</sup>.

## 4.2 Results and discussions

### 4.2.1 Morphology and structure

Self-standing carbon nanofiber electrodes were prepared following the route introduced in 4.1.1, illustrated in Figure 4.1a. A white polymeric fiber mat was collected after spinning a total amount of 2 mL solution. After drying the fiber mats in the oven at 80 °C for 6 hours, they underwent heating treatments including stabilization and carbonization. During the stabilization process, the fiber mats not only turned brown as shown in Figure 4.1b, but also ended up with a higher mechanical stability which helps to sustain the fiber structure through the next higher temperature treatment. The stabilized fiber mats were then punched into discs with a diameter of 12 mm. All carbonized fibers were black and featured a good flexibility. The electrodes were then directly used in coin cell assemblies without any binder and current collector, hence, called self-standing electrodes.

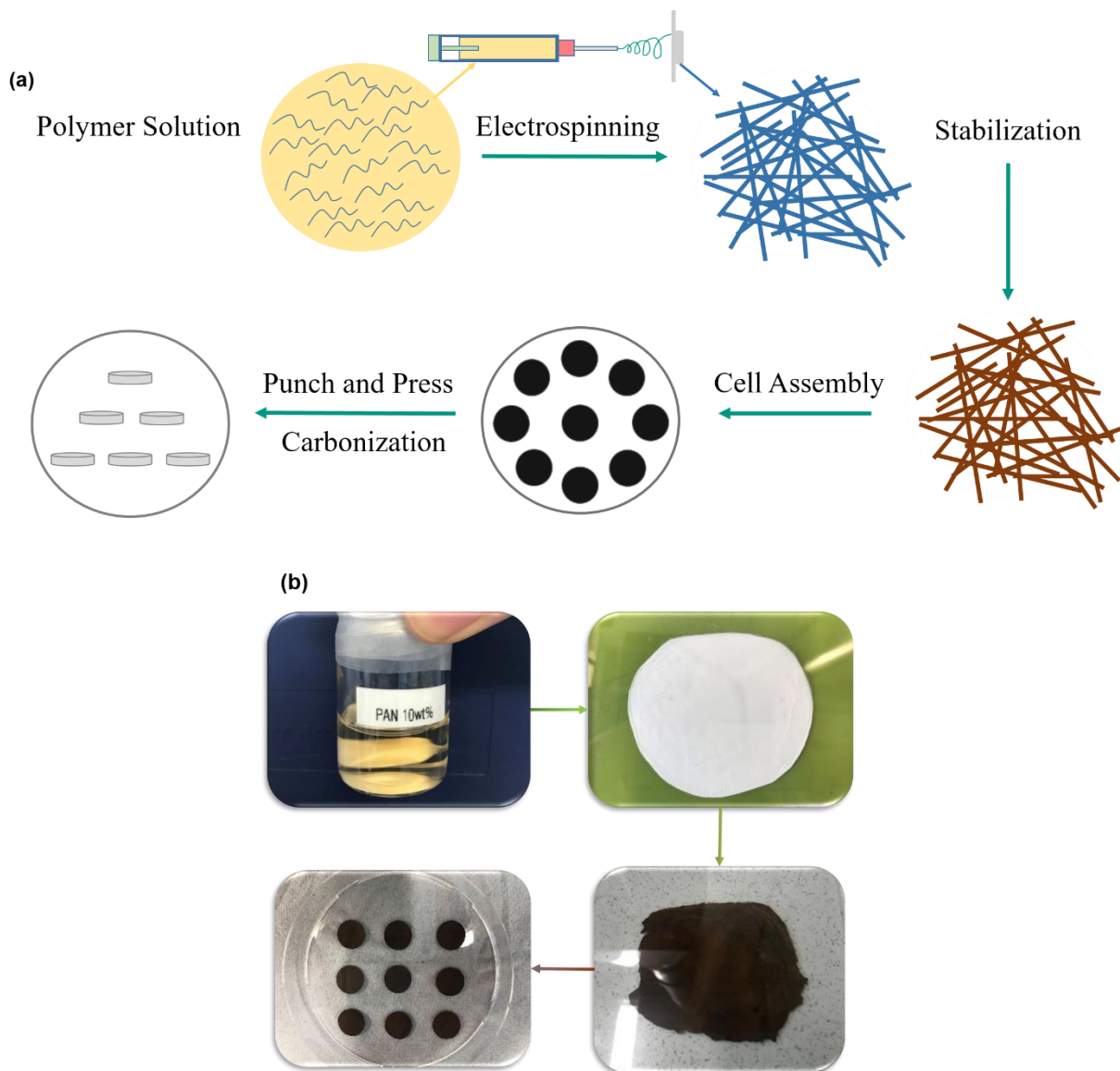


**Figure 4.1** (a) Schematic synthesis route of self-standing carbon nanofibers electrode applied in coin cell and (b) pictures of electrospun self-standing electrodes at each preparation stage.

The morphology of each CNF sample carbonized at different temperatures was analyzed by SEM, as shown in Figure 4.2. All samples consisted of randomly arranged nanofibers with no preferential alignment detectable. The fiber diameters and porous structures varied with the different carbonization temperatures. From 600 °C to 1000 °C, the average diameters of the fibers decreased, with CNF<sub>600</sub> having an average diameter of 275 nm, while CNF<sub>800</sub> (average of 173nm) and CNF<sub>1000</sub> (average of 142 nm) exhibited smaller diameters. Moreover, CNF<sub>600</sub>

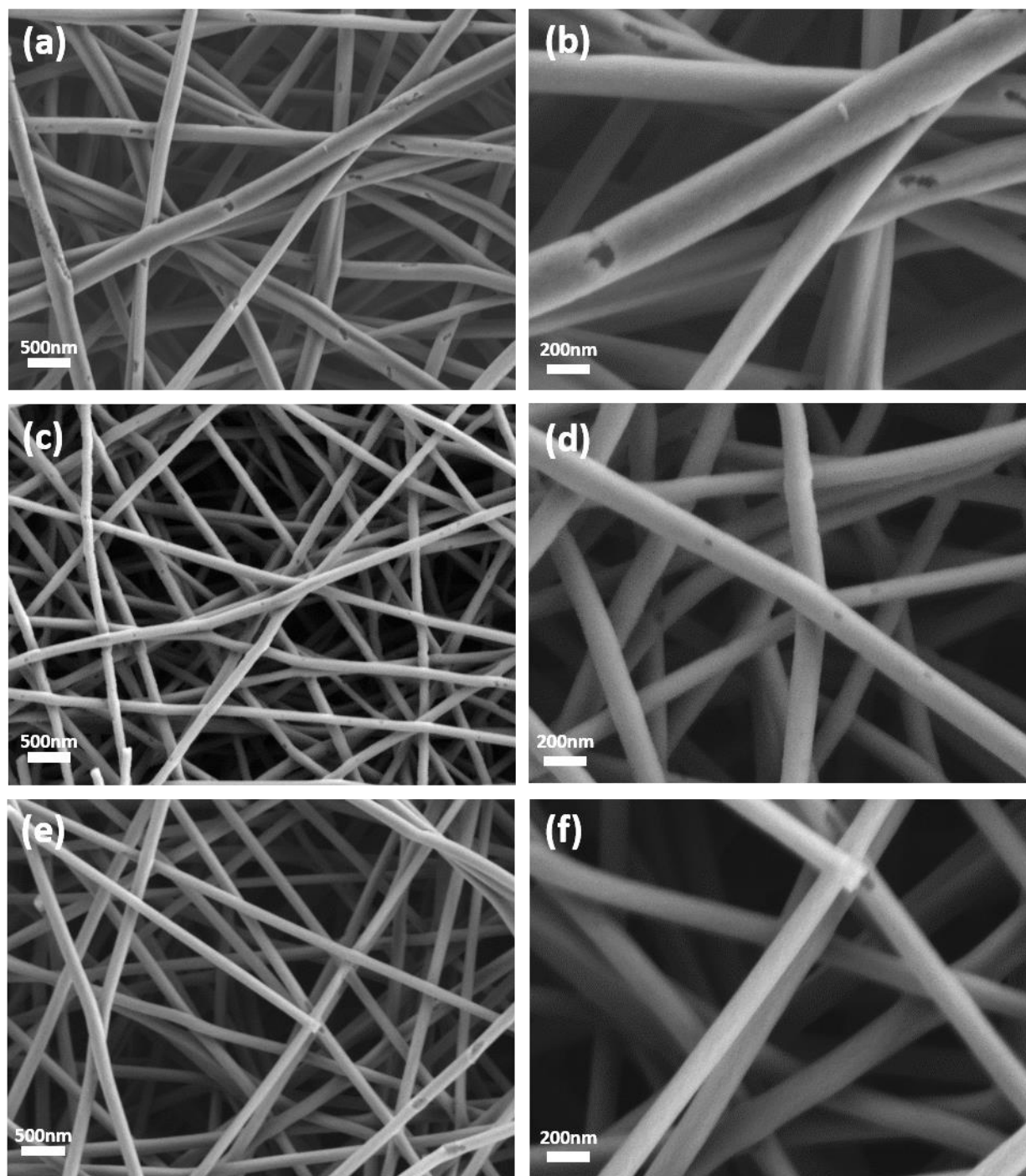


**Figure 4.2** SEM pictures of CNF electrodes carbonized at different temperatures: (a-b) CNF\_600, (c-d) CNF\_800, and (e-f) CNF\_1000.

contained macropores with an average pore size of 140 nm (longer sides), where the defects appeared smaller in CNF\_800 with an average value of 12 nm in diameter. In CNF\_1000, the fiber surface was smoother and showed much less defect sites. This correlates with previously published studies where a significant weight loss and structure change was observed at temperature higher than 700 °C.<sup>137,138</sup> The carbon content and other heteroatom compositions, except oxygen (O), of each CNFs were determined by elemental analysis, with C/H/N/S contents shown in Table 4.1. The high-temperature treatment led to a decrease in heteroatom concentration as expected. At low carbonization temperature (600 - 700 °C), it is believed that the stabilized fibers still undergo further cyclization in the uncyclized parts with further cross-linking and chain-scission reactions.<sup>138</sup> With increasing temperatures higher than 700 °C, condensation reactions start to be dominant with detectable gas formation of HCN and N<sub>2</sub>.<sup>138</sup> Thus, CNF\_600 stands out with a different morphology compared to CNF\_800 and CNF\_1000, which share a similar fiber morphology and chemical compositions with only small variations.

**Table 4.1** Element C/H/N/S composition of CNF\_600, CNF\_800, and CNF\_100 determined by elemental analysis.

Sample	N (wt%)	C (wt%)	H (wt%)	S (wt%)
CNF_600	22.56	63.75	2.25	0.08
CNF_800	10.30	72.99	2.00	0.12
CNF_1000	5.53	87.99	1.24	0.08

The structures of the carbon content in electrospun CNFs were further investigated by Raman spectroscopy and the results are shown in Figure 4.3. There are two main peaks observed for each sample (black), predominately originating from the sp<sup>2</sup> contributes.<sup>139</sup> The D peak at ~1356 cm<sup>-1</sup> is assigned to disordered turbostratic carbon, corresponding to a disordered structure, while the G peak at ~1576 cm<sup>-1</sup> is assigned to graphitic carbon, representing the graphitic domains.<sup>140</sup> It is obvious to conclude that carbonization at higher temperature will lead to a more graphitic structure in the electrospun CNFs. Moreover, after fitting one can observe two broad peaks at around 1200 cm<sup>-1</sup> and 1500 cm<sup>-1</sup>, referred to as D<sub>4</sub> (red line, Figure 4.3) and D<sub>3</sub> (green line, Figure 4.3),

respectively. These D<sub>4</sub> and D<sub>3</sub> peaks are commonly present in highly defective carbon structures, where D<sub>4</sub> refers to hydrocarbons, while D<sub>3</sub> is indicative for amorphous carbon.<sup>141,142</sup>

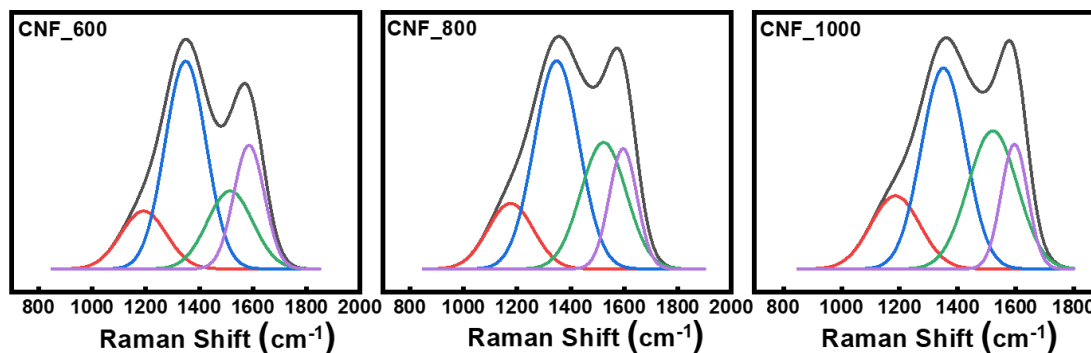


**Figure 4.3** Deconvolution Raman spectra of CNF\_600, CNF\_800, and CNF\_1000.

## 4.2.2 Electrochemical performance

Carbon nanomaterials have been extensively studied as anode materials in LIBs as alternative options to offer higher energy densities than graphite.<sup>84,143</sup> In former studies, it was proved that the lithiation/delithiation process in carbon nanotube fibers (CNTFs) is substantially different from that in traditional graphite electrodes.<sup>144</sup> In contrast, with the inability of graphite being applied as anode for SIBs, a critical, deeper and fundamental study of the mechanism of CNF for SIBs is necessary.

The electrochemical sodiation of CNFs was first investigated by CV in coin cells against sodium metal with CNF\_1000, as shown in Figure 4.4. Cyclic voltammetry was carried out at  $0.1 \text{ mV s}^{-1}$  in the voltage range of 0.01 – 2 V. In the cathodic scan of the first cycle, two strong broad peaks were observed at 0.81 V (Ic) and 0.45 V (IIc), respectively. Below 0.1 V, the cathodic current increased monotonically until the vertex potential reached 0.015 V where a sharp peak appeared (IIIc). During the corresponding anodic scan, one weak broad peak and one intensive peak were observed at 0.75 V (Ia) and 0.11 V (IIa), respectively. In the following cycles, the cathodic peaks Ic and IIc disappeared. Moreover, the intensity of peak IIIc decreased with increasing cycles, while the anodic peak at 0.11V shifted slightly to a higher potential compared to the first cycle.

The two peaks of Ic and IIc can be ascribed to an irreversible process, as they disappeared in the second cycle. A solid electrolyte interphase (SEI) is known to allow for the reversible Na insertion into hard carbon.<sup>145</sup> In the subsequent scans, these two irreversible reduction peaks disappeared, which implies that the SEI film mainly formed during the initial cycle.<sup>146</sup> The pair of sharp peaks (IIIc and IIa) showed up in every scan, hence, corresponding to the Na<sup>+</sup> ion insertion/deinsertion at low potentials. Different viewpoints about Na<sup>+</sup> intercalation have been proposed. Some believe that Na<sup>+</sup> ion intercalate into the graphitic domains with enlarged d-spacing, while others suggested that Na<sup>+</sup> ions are absorbed in nanopores in the carbonaceous structure.<sup>147</sup> The peak Ia grew less noticeable with increasing cycles and disappeared at 5<sup>th</sup> cycle, indicating that this anodic peak was probably from some unexpected side reactions with the electrolyte during the initial cycles.

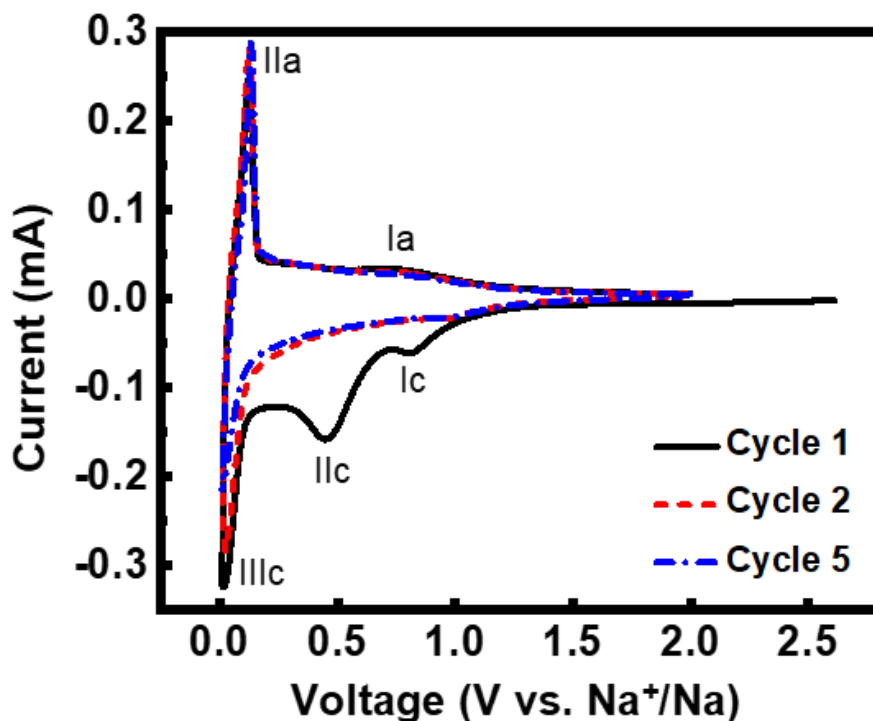


**Figure 4.4** Cyclic voltammograms of CNF\_1000 vs Na at 0.1 mV s<sup>-1</sup> at 1<sup>st</sup>, 2<sup>nd</sup>, and 5<sup>th</sup> cycles.

To obtain a deeper knowledge of the peaks, CV curves of CNF\_600 and CNF\_800 were recorded with the same scan rate and are shown in Figure 4.5. In the first reduction cycle, only one broad peak showed up in both electrodes, similarly to other studies.<sup>148,149</sup> It can be concluded that the IIc

peak appeared at a similar potential and is likely to be ascribed to the SEI formation, while the  $I_c$  peak only existed in CNF\_1000, which can be ascribed to the irreversible reaction of the electrolyte with functional surface groups.<sup>150</sup> Noticeably, the anodic peaks at low potential around 0.1 V become less distinctive in CNF\_800 and invisible in CNF\_600. Therefore, the theory where the sodium ions intercalate and extract from graphite layers is more favorable due to a lower graphitization degree in the electrodes with decreasing carbonization temperatures. Moreover, the insertion/deinsertion peaks were weaker compared to CNF\_1000 showing a more sluggish kinetic in the carbon structures. Constant sodium ion insertions were observed in all samples near 0.01 V, which is attributed to  $\text{Na}^+$  ion insertion into porous carbon. However, with sodium metal as the counter electrode offering a continuous sodium source, these cathodic peaks need to be dealt with care.

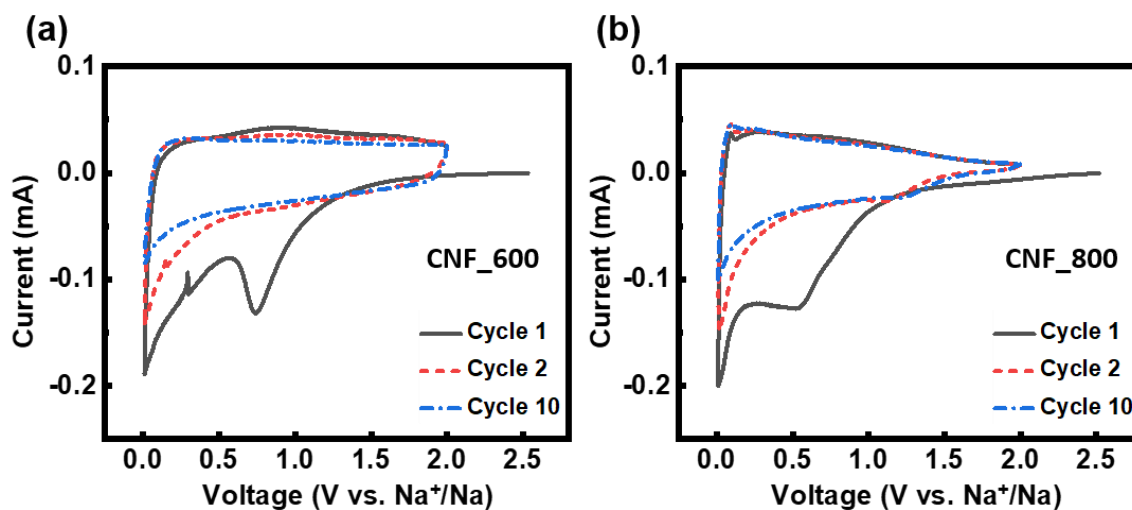


**Figure 4.5** Cyclic voltammograms of (a) CNF\_600 and (b) CNF\_800 vs Na at  $0.1 \text{ mV s}^{-1}$  at 1<sup>st</sup>, 2<sup>nd</sup>, and 10<sup>th</sup> cycles.

To determine the effect from carbonization temperatures and whether the sodiation/desodiation of CNFs has a predominantly diffusive or capacitive character, extensive CVs were measured at different scan rates between  $0.1$  and  $100 \text{ mV s}^{-1}$ , as shown in Figure 4.6. First, we can directly see that the CV curves from CNF\_600 (Figure 4.6b) exhibit in more rectangular-like shapes, which is similar to a capacitor behavior, while the CV curves from CNF\_1000 (Figure 4.6f) show more pro-

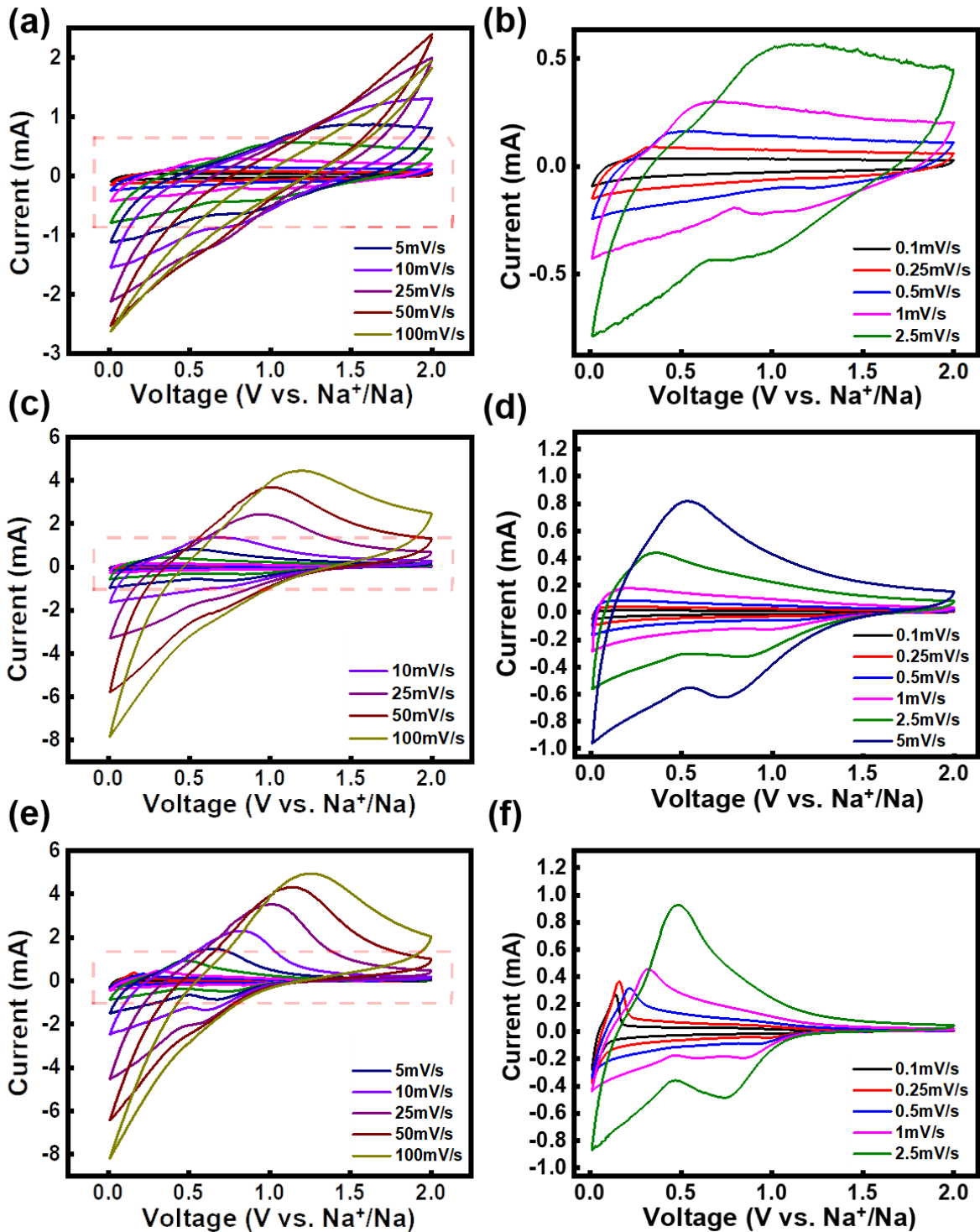


**Figure 4.6** CV curves of each electrode at the voltage window of 1.5 – 4.5 V: (a-b) CNF\_600, (c-d) CNF\_800, (e-f) CNF\_1000. On the right side enlarged regions of the red dashed area from the left side are shown.

found peaks. In CNF\_800, broad peaks are shown with less intensities as CNF\_1000. The voltammogram shifted to higher voltage due to overpotential with increasing scan rates.

Detailed study can be conducted following equation (4.1) where the current ( $i$ ) follows a power law relationship on the scan rate ( $v$ ) at a fixed potential

$$i = av^b \quad (4.1)$$

where  $a$  and  $b$  are adjustable parameters, with the  $b$  value determined from the slope of the plot of  $\log i$  vs  $\log v$ . For diffusion-controlled redox reactions, the current is proportional to the square root of the scan rate with  $b = 0.5$ , based on the following equation:

$$i = nFAC^*D^{1/2}v^{1/2}(\alpha nF/RT)^{1/2}\pi^{1/2}\chi(bt) \quad (4.2)$$

where  $C^*$  is the surface concentration of the electrode material,  $\alpha$  is the transfer coefficient,  $D$  is the chemical diffusion coefficient,  $n$  is the number of electrons involved in the electrode reaction,  $A$  is the surface area of the electrode materials,  $F$  is the Faraday constant,  $R$  is the molar gas constant,  $T$  is the temperature and the  $\chi(bt)$  function represents the normalized current for a totally irreversible system as indicated by the cyclic voltammetric response. In the other condition, where  $b = 1$ , the current  $i$  is defined according to the following equation:

$$i = vC_dA \quad (4.3)$$

Where  $C_d$  is the capacitance. The current in this case is capacitive-controlled and proportional to the sweep rate.<sup>151</sup>

The intensity of the peak current is analyzed as a function of scan rate for CNF\_800 and CNF\_1000. The CV curves of CNF\_600 show no obvious peaks, hence displaying a capacitive character during the process. The  $b$  values were calculated from the slope of the double-logarithmic plot shown in Figure 4.7. For CNF\_1000,  $b$  was calculated as 0.63 from the linear fitting between 0.5  $\text{mV s}^{-1}$  to 10  $\text{mV s}^{-1}$ , hence suggesting a mixed diffusive/capacitive control. On the contrary, for CNF\_800  $b = 1$  after fitting, hence showing a surface-controlled mechanism. CNF\_1000, which was carbonized at the highest temperature among three samples, presents a good deintercalation mechanism with sodium. Amorphous carbon from low-carbonized temperature interact with  $\text{Na}^+$  ion following a different mechanism, where the large surface area can absorb  $\text{Na}^+$  ion to some extent.

Meanwhile, galvanostatic cycling profiles of each electrode were recorded and are shown in Figure 4.8, at a current density of  $100 \text{ mA g}^{-1}$  in a potential range of  $0.01 - 2.0 \text{ V}$ . The active material was calculated based on the carbon content of each sample to focus on the role and the effect of carbon structures. The first discharge curves relating to the SEI formation and electrolyte decomposition were different for the three different cells. CNF\_600 starts to exhibit a sloping curve at a high voltage of  $1.5 \text{ V}$ , while in CNF\_800 and CNF\_1000, the slope starts at lower voltages of  $1.2 \text{ V}$  and  $1.0 \text{ V}$ , separately. A plateau at lower potential of CNF\_1000 appears at around  $0.01 \text{ V}$ . The slope

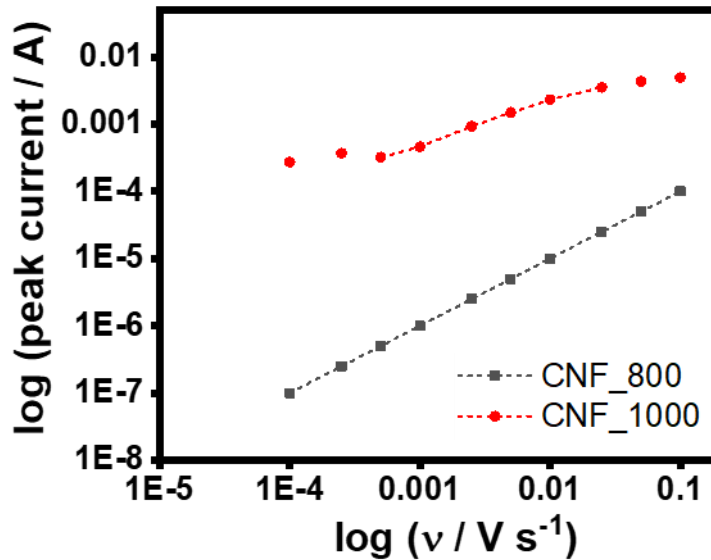


**Figure 4.7** Log-log plot of the intensities of CV peaks for CNF\_800 and CNF\_1000.

region correlates with a capacitive surface absorption behavior, while the plateau indicates the intercalation of  $\text{Na}^+$  ions which is consistent with the previous analysis of the CV curves. Another reason for a high-slope region in CNF\_600 is that the heteroatoms interact with sodium at a potential higher than  $1 \text{ V}$ , affecting the final voltage profile.<sup>146</sup> In the second cycles, all samples possessed less than half of their initial capacity. It shall be noted that the initial irreversible capacity loss has been an obstacle for high surface area carbon anode materials. In CNF\_1000, the charge-discharge curves exhibited a mixed shape of slope regions and plateau at low potential around  $0.1 \text{ V}$ , indicating a combined behavior of  $\text{Na}^+$  ions absorbing on the surface of CNFs and intercalating

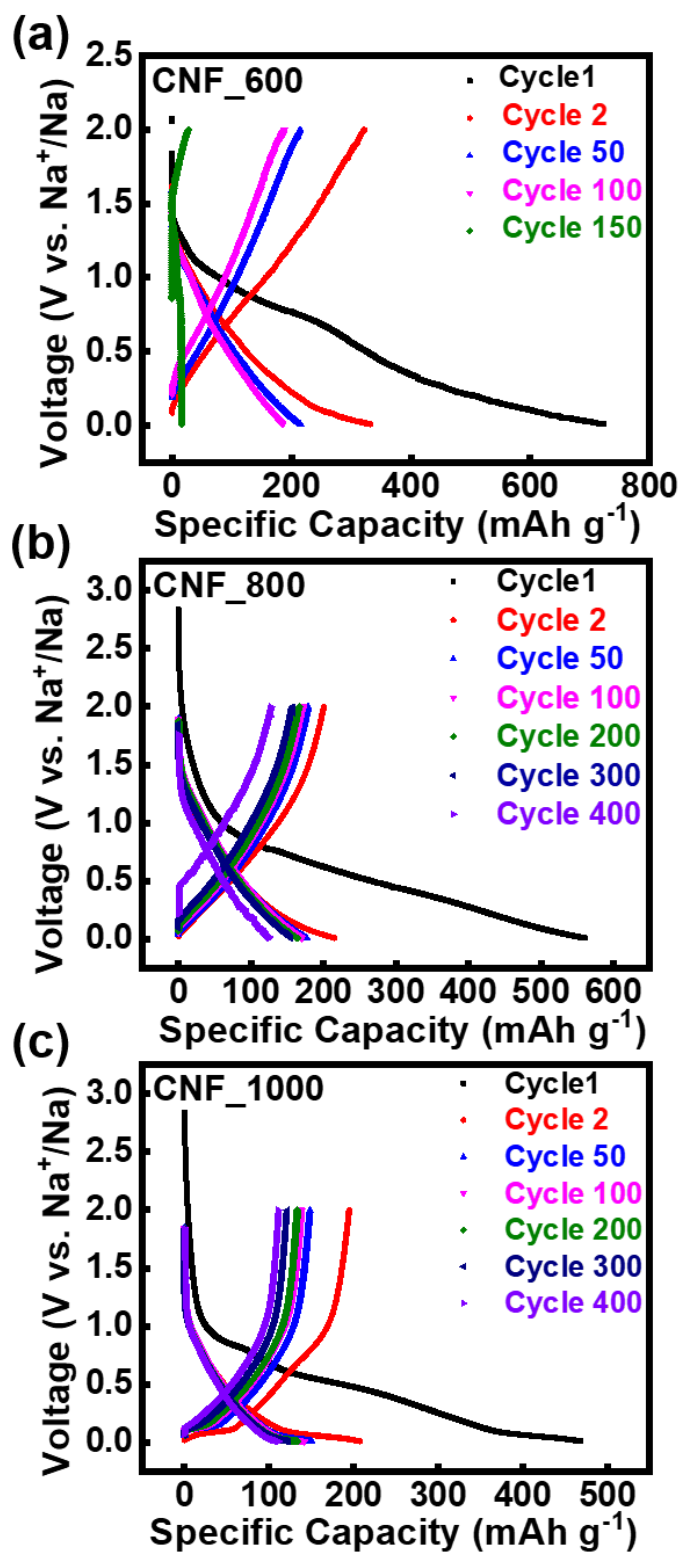


**Figure 4.8** Charge-discharge profiles of (a) CNF\_600, (b) CNF\_800, and (c) CNF\_1000 at a current density of 100 mA g<sup>-1</sup>

into the graphitic domains from the high temperature carbonization. In analogy to studies of LIBs, this is an evidence for electrospun CNFs carbonized at higher temperature evolving more graphitic structures.

Long cycle performances are presented in Figure 4.9a, cycling at  $100 \text{ mA g}^{-1}$ . From the 150<sup>th</sup> cycle on, CNF\_600 experienced a fast capacity decay. This cell failure of CNF\_600 can be attributed to the low electrical conductivity as reported in LIBs applications.<sup>137</sup> The reversible capacity of CNF\_600 decreased from  $325 \text{ mAh g}^{-1}$  to  $193 \text{ mAh g}^{-1}$ , i.e. 40.6% decrease, in the initial 100 cycles, showing a fast decay and a final cell failure at around 150<sup>th</sup> cycle. Same decrease in capacity also occurred for CNF\_800, but it was relatively small with 83.5% retention after 200 cycles. Surprisingly, the long-term cycle performance in CNF\_1000 was not satisfactory compared with CNF\_800 with a higher capacity loss of 68.1% retention in the initial 200 cycles.

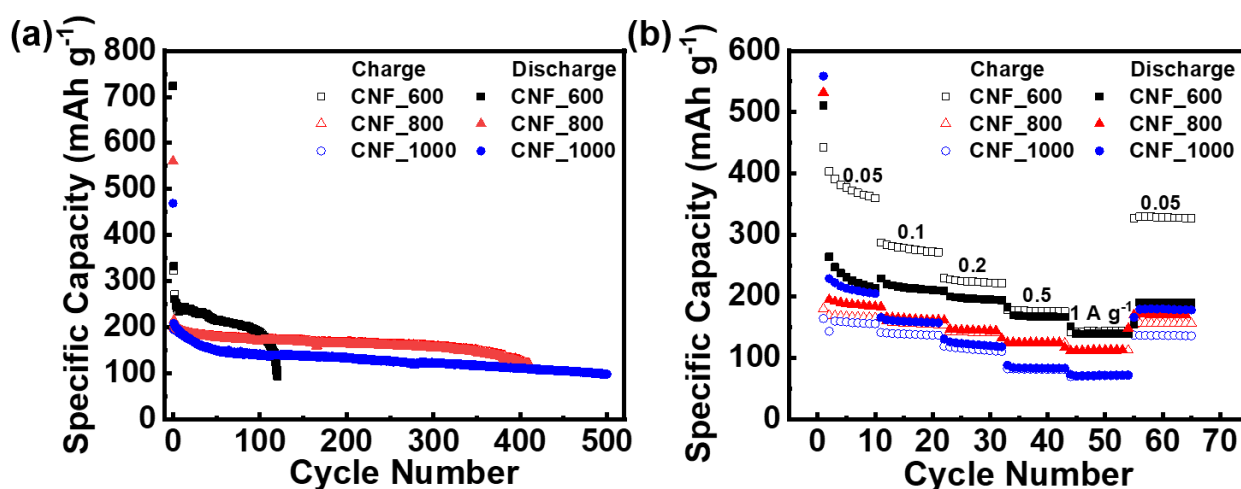


**Figure 4.9** (a) Charge - discharge curves of each electrode at  $100 \text{ mA g}^{-1}$  and (b) rate capability at different current rates of three anode materials.

The rate capability of each electrode with higher current densities was also measured (Figure 4.9b). Despite the capacity loss, when the cells were again cycled at a low current rate of  $50 \text{ mA g}^{-1}$  after higher current rates, reversible capacities of CNF\_600, CNF\_800 and CNF\_1000 were recovered by 76.6%, 91.3%, and 86.6%, respectively, with CNF\_800 showing the best overall performance among three different samples. In CNF\_600, high specific charge capacities along with low

coulombic efficiencies showed up at low current rates. This explains the absorption effect on the surface of nanofibers where a slow charging current rate allows more charges to be transferred and deposited, while the coulombic efficiency is much higher at higher current rate ( $1 \text{ A g}^{-1}$ ).

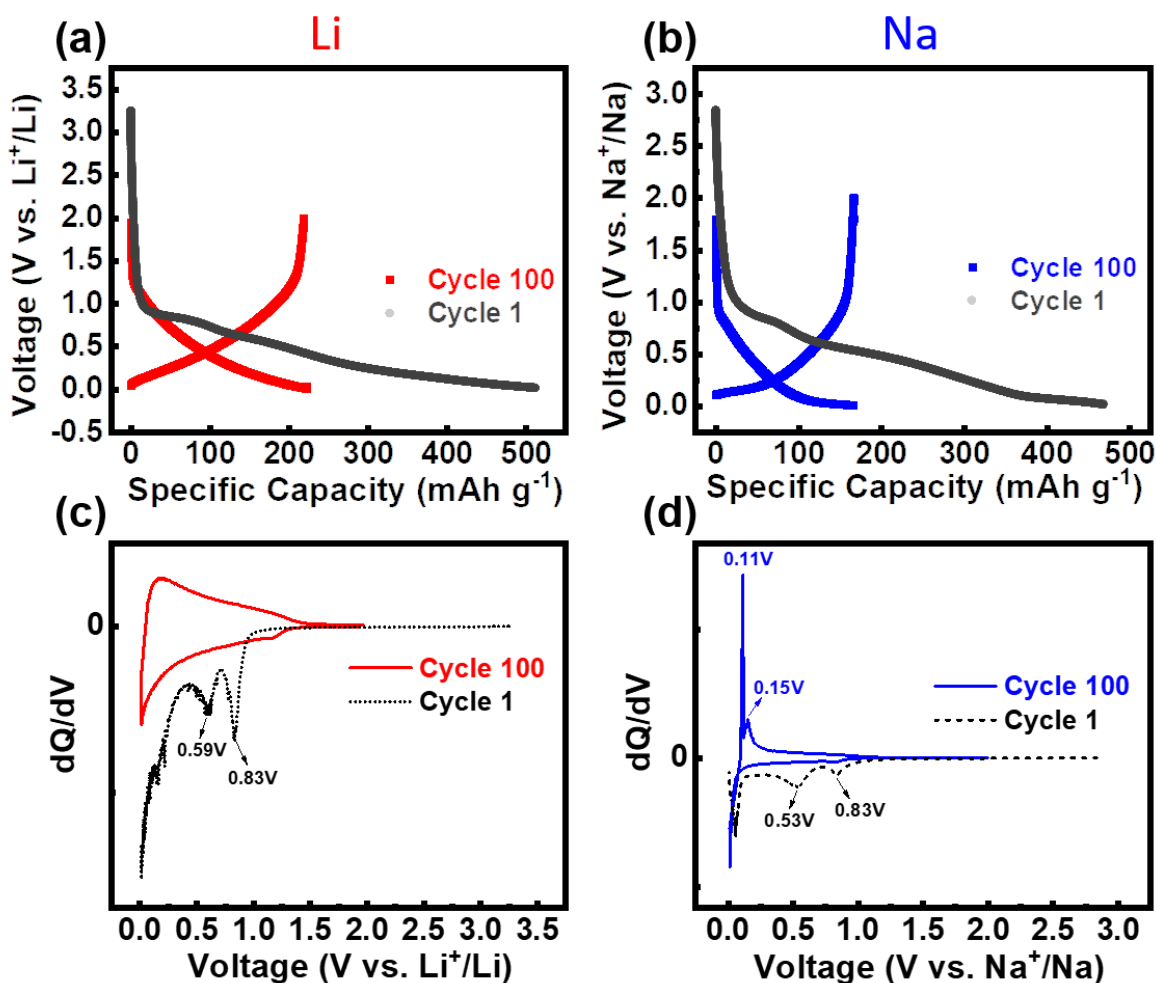


**Figure 4.10** Comparison of charge-discharge profiles of CNF\_1000 for (a) LIBs and (b) SIBs at a current density of  $100 \text{ mA g}^{-1}$  between 0.01 V and 2.0V. Corresponding  $dQ/dV$  plots for (c) LIBs and (d) SIBs.

To obtain an overall knowledge on the difference of CNFs utilized for LIBs and SIBs, the charge-discharge profiles of CNF\_1000 with differential capacity profiles were plotted accordingly and the initial and 100<sup>th</sup> cycle are shown in Figure 4.10. In both batteries, we observe some similarities in the initial cycle with a high first-cycle irreversible capacity. Peaks at 0.83 V and 0.53 – 0.59 V relate to SEI formation and other possible side reactions such as electrolyte decomposition. Plotting the  $dQ/dV$  as a function of the voltage (Figure 4.10c and 4.10d) revealed at low potentials a much

more prominent peak in SIBs instead of a broad peak in LIBs, suggesting that  $\text{Na}^+$  ions interact with CNFs following a diffusion-controlled redox reaction to a much higher extent than  $\text{Li}^+$  ions under the same conditions.

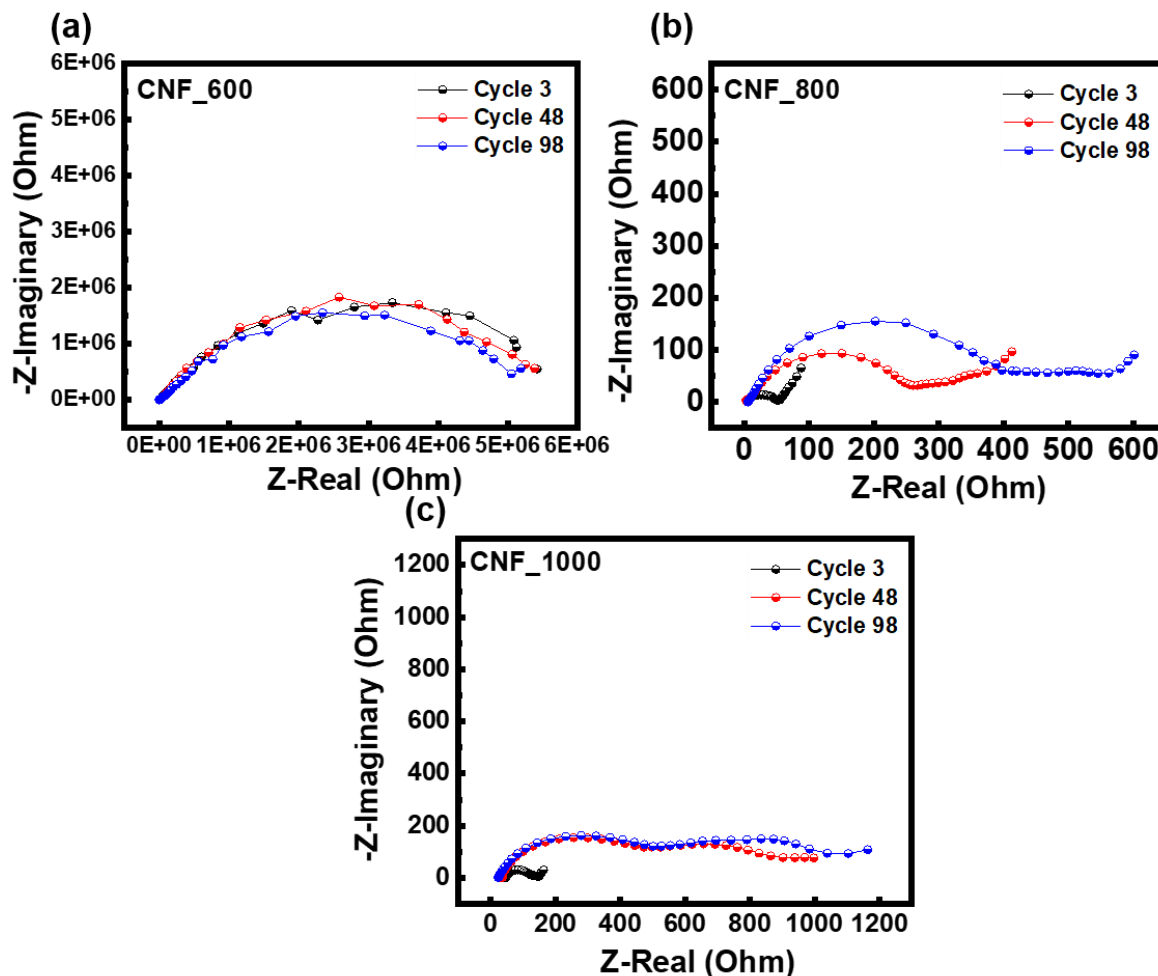


**Figure 4.11** Impedance spectroscopy plots at different cycle numbers at discharged state (0.01 V): (a) CNF\_600, (b) CNF\_800, and (c) CNF\_1000.

The Nyquist plots ( $-Z''$  vs  $Z'$ ) for CNF\_600, CNF\_800 and CNF\_1000 are shown in Figure 4.11. The cycled cells were all tested at the discharged state at 0.01 V. In CNF\_600 cells, we can observe one semi-circle, which indicates a high impedance due to the low conductivity resulting from the lower carbonization temperature. Both CNF\_800 and CNF\_1000 exhibited a good electric conductivity as the real part of the impedance was below 600  $\Omega$  and 1200  $\Omega$  even after 98 cycles. CNF\_800 showed a better electrical conductivity than CNF\_1000, which contributes to the already

discussed better electrochemical performance. In both electrodes, the resistance kept increasing within the first 100 cycles. However, the enlargement of semicircle of CNF\_1000 reached a stable phase earlier than CNF\_800, displaying a better electronic contact of electrospun CNFs with the electrolyte.

The plots of CNF\_1000 (Figure 4.11c) show two semicircles, which were fitted based on the impedance circuit shown in Figure 4.12a. The circuit consists of three resistance elements including  $R_1$ , which corresponds to a bulk resistance that may arise from the electronic conductivity of carbon and ionic conductivity of the electrolyte.  $R_2$  is due to SEI formation and  $R_3$  is from charge transfer resistance.<sup>137</sup> From Figure 4.12b, we can see that  $R_1$  decreased slowly and became stable with cycling, which is beneficial for an ionic and electronic transfer as electrode material. A rapid increase of  $R_2$  and  $R_3$  was observed in the initial cycles and  $R_2$  showed minor changes in the following cycles. SEI formation and other side effects occurred in the beginning and grew stable upon cycling. But the continuous increase of  $R_3$  is a phenomenon that may correlate to some unknown side reactions.

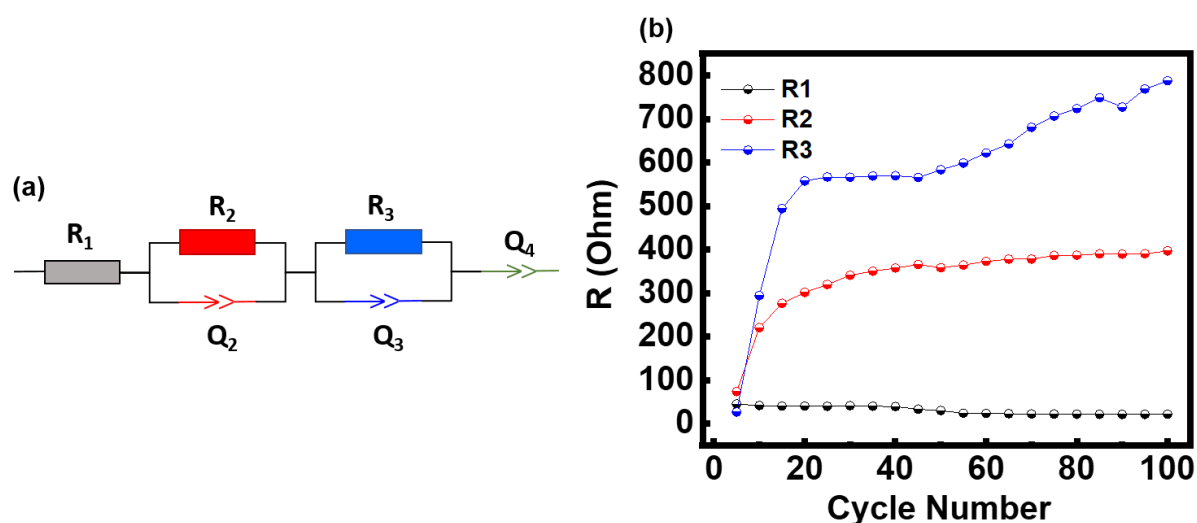


**Figure 4.12** (a) Equivalent electrical circuit used to fit the data of Figure 4.11c CNF\_1000 and (b) changes of  $R_1$ ,  $R_2$ , and  $R_3$  over cycles.

### 4.2.3 *In situ* and *ex situ* studies

In operando Raman can offer a detailed look at the  $\text{Na}^+$  storage process in CNFs (CNF\_1000 as representative). The cell was first discharged to 0.01 V at a low current density of  $5 \text{ mA g}^{-1}$  from OCV. Until 0.25 V, two peaks were observed representing the D-band and G-band, which is a typical spectrum of defect-containing graphite as introduced above (Figure 4.13). However, the G-band starts to show an obvious shift to lower energies from 1.0 V on where the sloping region started. This behavior is in analogy to the study in hard carbon for SIBs, where it indicates that the G-band shift is directly linked to the sloping region of the potential curve.<sup>152</sup> From 0.25 V on, the G-band stopped shifting and stayed constant during the charging process, while the D-band started to disappear. In a similar study, the G-band shifting indicated that initially sodium is intercalated between  $\text{NaC}_{24}$  and  $\text{NaC}_{12}$ , and the insertion stopped when a saturation was reached.<sup>153</sup> However, the disappearance of D-band still remains a complicate and debatable issue to explain.

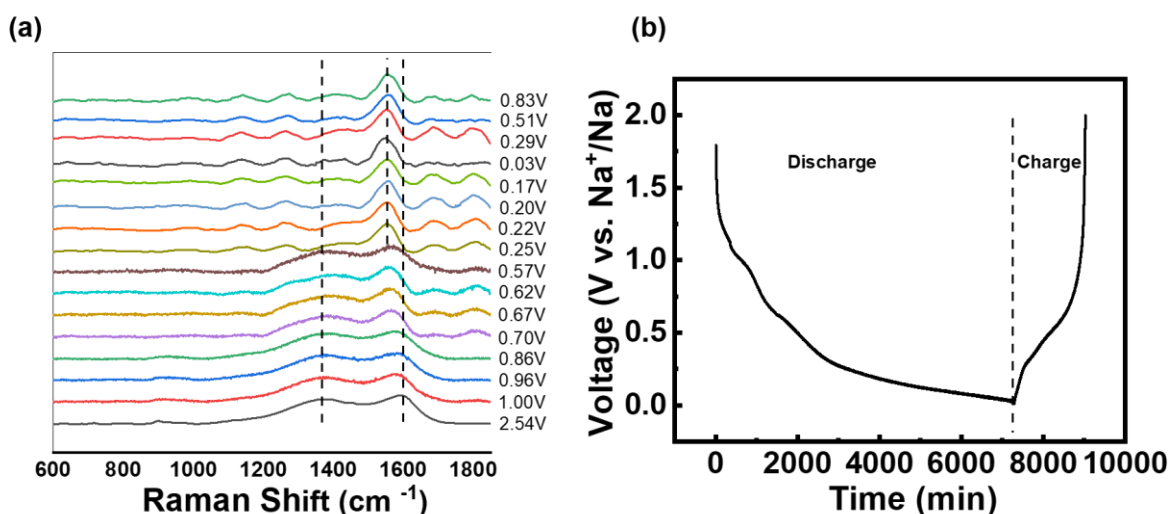


**Figure 4.13** *In situ* Raman studies: (a) Selections of Raman spectra collected in operando mode, discharge from OCV to 0.01 V and charge to 2.0 V. (b) Charge-discharge curves, at a current density of  $5 \text{ mA g}^{-1}$  (discharge) and  $10 \text{ mA g}^{-1}$  (charge) in the voltage window of 0.01 V-2.0 V vs.  $\text{Na}^+/\text{Na}$ .

The morphology of the CNF\_1000 anode was also analyzed by SEM after cycling, as shown in Figure 4.14. The average diameter of the fibers increased from 142 nm to 245 nm after cycling

along with a larger surface at the cross sections of fibers. However, the overall fibrous structure of the electrode remained intact indicating a good stability of the electrospun CNFs of the fibers upon cycling.

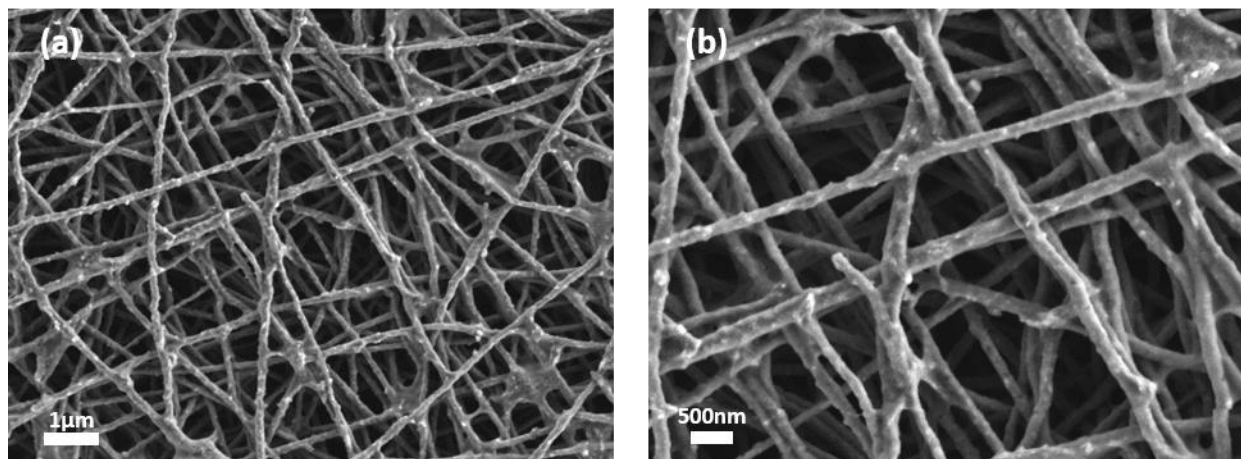


**Figure 4.14** SEM pictures of cycled CNF\_1000 electrode after 200 cycles.

### 4.3 Summary

Self-standing carbon nanofibers were successfully prepared via electrospinning and applied directly for SIBs as binder-free and collector-free anodes. Different carbonization temperatures were used for the electrospun nanofibers and the effects on electrochemical performance were studied. The interactions of  $\text{Na}^+$  ions with CNFs follow very different mechanisms depending on the carbon structures developed at different temperatures. CNF\_600 and CNF\_800 both showed surface capacitive characters based on cyclic voltammograms and CVs at different scan rates. The interaction of  $\text{Na}^+$  ions with CNF\_1000 was proved to behave in a mixed mechanism of diffusion-controlled and surface-controlled behavior. Among all the CNFs, CNF\_800 showed the best electronic conductivity and the overall best electrochemical performance. The intercalation into the graphitic domains of CNF\_1000 was also proved by *in situ* Raman and other studies. Electrospun self-standing CNFs are not suitable for application due to the fast capacity decay, modification and improvement need to be further carried out.

## 5 Self-standing NaFePO<sub>4</sub> / carbon nanofiber cathode for SIBs

### 5.1 Experimental part

#### 5.1.1 Material preparation

Na<sub>2</sub>CO<sub>3</sub> (99.95%, Acros), FeC<sub>2</sub>O<sub>4</sub>·2H<sub>2</sub>O (99%, Alfa Aesar) and NH<sub>4</sub>H<sub>2</sub>PO<sub>4</sub> (99.99%, Sigma-Aldrich) with the molar ratio of 0.5: 1: 1 were used as starting materials for the synthesis of maricite NaFePO<sub>4</sub> nanoparticles. All starting materials were ground manually for half an hour and then loaded in a ball-milling container with ZrO<sub>2</sub> milling balls (Ø 3 mm) at a weight ratio of 4:1. The ball milling was performed with a planetary ball mill (Pulverisette 7 Premium Line, Fritsch) for 99 cycles at 500 rpm without any milling agent with parameters of milling for 5 minutes and resting for 10 minutes, alternatively. The obtained yellowish powders were then carefully ground and calcined at 350 °C under argon atmosphere for 5 hours before being re-ground and pressed into pellets (Ø 14 mm). The pellets underwent a second calcination at 600 °C under argon for 10 hours and then were ground for further use.

Afterward, the NaFePO<sub>4</sub> nanoparticles were dispersed in a 10 wt% PAN / DMF solution under strong stirring for overnight with a mass ratio of NaFePO<sub>4</sub>:PAN in 1:2. The preparation of PAN / DMF solution was done as described in section 4.1.1. The composite solution was then loaded into a 1 mL syringe with the setup also introduced in 4.1.1. The temperature and humidity were set to 25 °C and 20%. A high voltage of 13 - 16 kV was applied with a 15 cm tip-to-collector distance and a 0.5 mL/h feeding rate. In total, the 1 mL solution was spun two times into one fiber mat. The fiber mat was then vacuum dried at 60 °C for 6 hours, stabilized in air with the same heating steps introduced in 6.1.1 before being carbonization under argon at 600 °C for 1 hour. Self-standing NaFePO<sub>4</sub>/CNF electrodes can be directly assembled in laboratory coin cells. Higher carbonization temperature at 800 °C conducted for 1 hour was also performed for comparison study, with the product named as NaFePO<sub>4</sub>/CNF-800.

## 5.1.2 Material characterization

### *SEM*

The morphology of all the samples was observed with a Merlin thermal field emission scanning electron microscope (FE- SEM) (Carl Zeiss SMT AG). Carbon tapes were used as substrates. Self-standing NaFePO<sub>4</sub>/CNF cathodes were directly attached to the carbon tape without any coating. Cycled samples were obtained after cell disassembly, washed with DMC, and then dried under vacuum at 65 °C in a glovebox for at least 2 hours prior to the test. A vacuum transport tube was used for transferring the cycled *ex situ* samples.

### *EDX*

Energy-dispersive X-ray spectroscopy (EDX) was performed to confirm the elemental compositions (Brucker Quantax, 400 SDD). The accelerating voltage was 10 kV which is high enough to excite the K $\alpha$  line of iron (6.398 keV). No sputtering was used to coat any of the samples.

### *XRD*

The structures of NaFePO<sub>4</sub>/CNF cathode were investigated by means of X-ray diffraction (XRD). The measurements were carried out on an STOE STADI P X-ray powder diffractometer with a Mythen 1K detector and Mo K $\alpha$ <sub>1</sub> radiation ( $\lambda = 0.7093 \text{ \AA}$ ). Self-standing electrodes were ground and filled into capillaries ( $\varnothing 0.5 \text{ mm}$ ) measured in Debye-Scherrer mode in a  $2\theta$  range of 3 – 42°.

### *Raman Spectroscopy*

Raman measurements were performed on a LabRam Evolution HR instrument (HORIBA Jobin Yvon) applying a 532 nm wavelength laser. Each spectrum was taken as the average of three 45-second accumulations.

### *Mössbauer Spectroscopy*

Mössbauer spectroscopy was performed at room temperature with a constant acceleration spectrometer in transmission mode and a <sup>57</sup>Fe(Rh) source. All isomer shifts are given relative to that of  $\alpha$ -Fe metal. The cells were charged to 4.5 V, discharged to 1.5 V in the initial cycle and in the 100<sup>th</sup> cycle, separately. The cells were afterwards disassembled, cathode materials were washed

with dimethyl carbonate (DMC), dried at 60 °C for 12 h and then sealed in polyethylene/aluminum bags in an argon-filled glovebox (O<sub>2</sub>, H<sub>2</sub>O < 0.1 ppm).

### *TGA*

Thermogravimetric analysis (TGA) was performed to determine the content of carbon and active material NaFePO<sub>4</sub> in the composite electrode. It was carried out on an STA 449 C Jupiter instrument (NETZSCH) with a heating rate of 10 °C/min up to 1200 °C in an oxygen atmosphere.

### *HT-XRD*

*In situ* high temperature XRD (HT - XRD) was carried out at synchrotron at Paul Scherer Institute (PSI), Villigen, Switzerland. NaFePO<sub>4</sub> powders were heated in air with a heating rate of 20 °C/min from 90 °C up to 400 °C and then cooled down to 90 °C. During heating and cooling, 53 XRD spectra were recorded. The wavelength ( $\lambda$ ) was 0.5106 Å and a MYTHEN II detector was used.

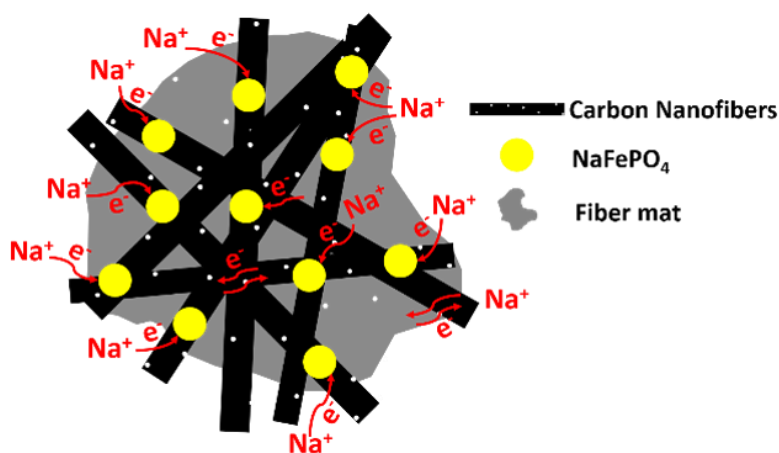
## **5.1.3 Electrochemical performance**

The electrochemical performance was studied in coin cells (CR2032) with sodium metal as the counter/reference electrode, glass fiber (Whatman, GF/D) as the separator and 0.8M NaClO<sub>4</sub> in EC:DEC 1:1 w:w as electrolyte. The electrospun self-standing electrodes were punched into the right size ( $\varnothing = 12$  mm) and directly assembled in the coin cells without any additional current collector. Galvanostatic cycling, cyclic voltammetry (CV) and electrochemical impedance spectroscopy (EIS) were carried out on a multichannel potentiostat (VMP3, Bio-Logic). The voltage ranges of galvanostatic cycling and CV tests are 4.5 - 1.5 V vs. Na<sup>+</sup>/Na. The galvanostatic mode was a CC-CV charging mode at 0.1C, with the voltage of 4.5 V holding for 5 hours with a current limit of 0.05C. The calculation of the specific capacity of NaFePO<sub>4</sub>/CNF is based on the mass of NaFePO<sub>4</sub>. EIS tests were carried out at charged state (4.5 V) and discharged state (1.5 V) with an alternating current signal of a 5 mv amplitude ranging from 1MHz and 0.01Hz.

## 5.2 Results and discussions

### 5.2.1 Morphology and structure

Maricite  $\text{NaFePO}_4$  nanoparticles were first prepared via mechanical ball milling and then dispersed in the polymer solution under strong stirring for further electrospinning.<sup>37</sup> Under high voltages, the nanofibers got collected onto an aluminum foil and then treated with a two-step heating procedure resulting in a flexible, black-colored, self-standing mat which can be cut into electrodes and directly assembled in coin cells without further handlings. It is generally known that maricite  $\text{NaFePO}_4$  is electrochemically inactive due to the lack of pathways for  $\text{Na}^+$  ion transportation. By integrating maricite  $\text{NaFePO}_4$  particles onto carbon nanofiber (CNF) mats, the obtained network can offer diffusion channels for  $\text{Na}^+$  ions and electrons during a charge-discharge process as shown in Scheme 5.1. Moreover, the carbon content can improve the electrical conductivity facilitating a better electrochemical performance of such a hybrid electrode. A 30 wt% weight percentage of  $\text{NaFePO}_4$  within the hybrid electrode was determined by TGA measurement (Figure 5.1). The morphology of the obtained self-standing electrode is shown in Figure 5.2, with the  $\text{NaFePO}_4$



**Scheme 5.1** Schematic illustration of the possible  $\text{Na}^+$  ion pathways in the carbon nanofibers matrix.  
(White spots illustrate pores and defects on the nanofibers.)

particles dispersed homogeneously in the carbon nanofibers. Clusters of the active material due to agglomeration can also be observed. The EDX results in Figure 5.3(a-g) show that the active material particles consist of Na, Fe, P, and O and are embedded in the nanofibers, which consist of C and N. Noteworthy, the traces of nitrogen are the residue from the low temperature carbonization process of PAN.<sup>154</sup>

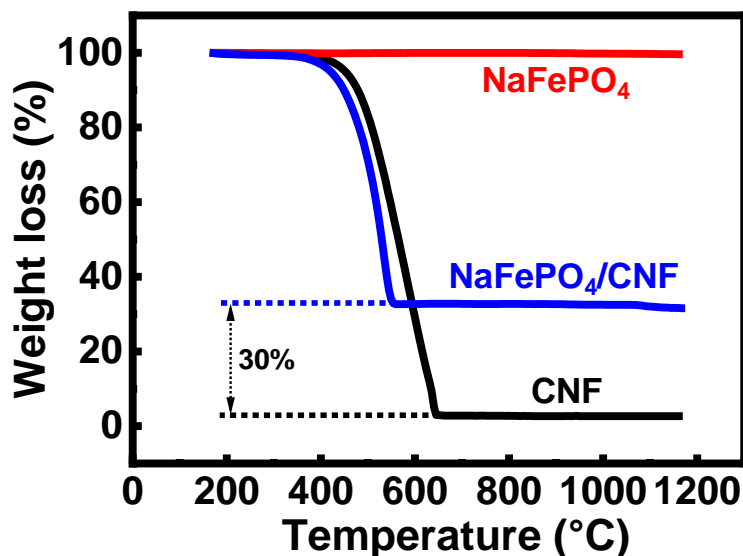


**Figure 5.1** TGA curves of NaFePO<sub>4</sub>, CNF and NaFePO<sub>4</sub>/CNF under oxygen to determine the content of NaFePO<sub>4</sub>.

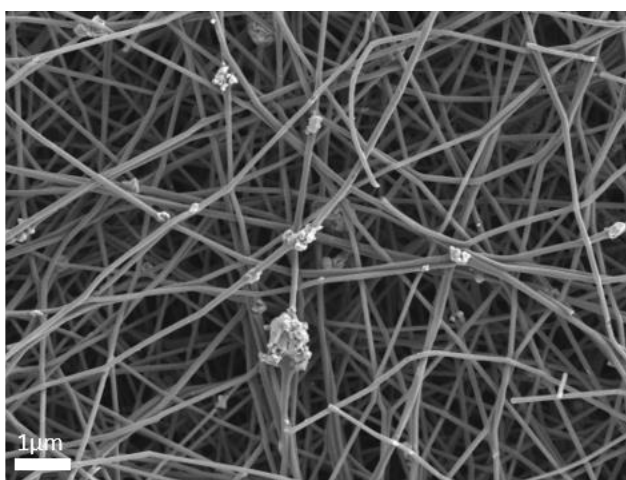


**Figure 5.2** SEM images of the electrospun NaFePO<sub>4</sub>/CNF electrodes.

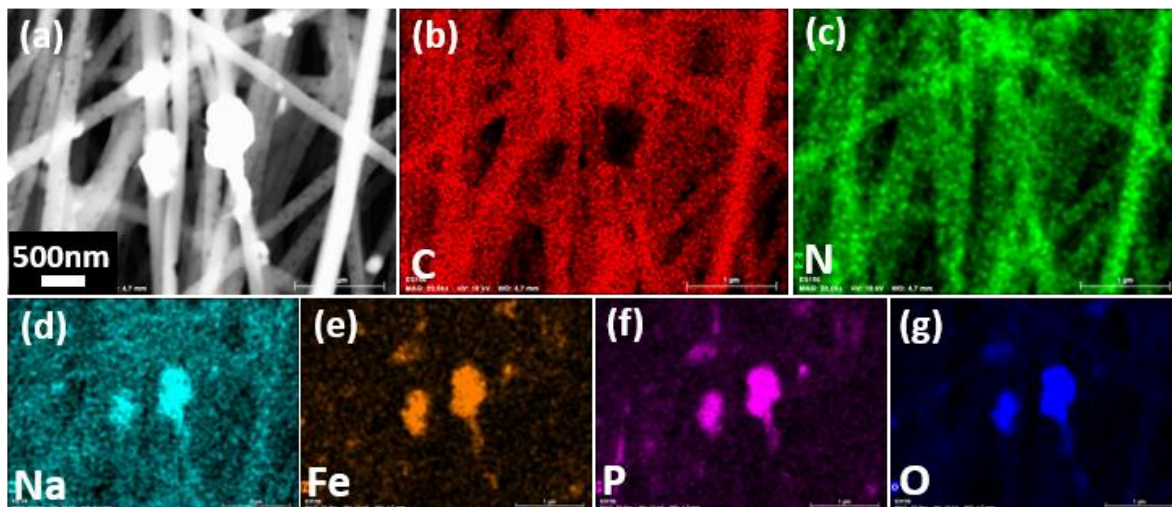


**Figure 5.3** (a) SEM picture, and corresponding EDX mappings of elements: (b) C (carbon); (c) N (nitrogen); (d) Na (sodium); (e) Fe (iron); (f) P (phosphorous) and (g) O (oxygen).

The structures of  $\text{NaFePO}_4$  and  $\text{NaFePO}_4/\text{CNF}$  electrodes were also investigated by XRD. As shown in Figure 5.4, a phase-pure maricite structure of  $\text{NaFePO}_4$  indexed based on a  $Pmnb$  orthorhombic model was obtained. With a Rietveld refinement, the lattice parameters of  $\text{NaFePO}_4$  were determined as  $a = 6.8659(2)$ ,  $b = 8.9761(2)$ , and  $c = 5.0412(2)$  Å. The presence of carbon nanofibers in the composites with CNF introduced an obvious amorphous phase underlying the reflections from crystalline  $\text{NaFePO}_4$ . Fortunately, the  $\text{NaFePO}_4$  lattice parameters in the  $\text{NaFePO}_4/\text{CNF}$  composites show minor changes without size broadening with  $a = 6.8669(2)$ ,  $b = 8.9820(2)$ , and  $c = 5.0432(2)$  Å, which indicate that the structure of the active material  $\text{NaFePO}_4$  was not affected during the high temperature procedures of carbon nanofibers formation.

However, some new reflections appeared for the  $\text{NaFePO}_4/\text{CNF}$  electrodes at low angles ( $5^\circ - 7^\circ$  and  $11^\circ - 14^\circ$ , respectively), which may refer to some impurity phases. According to the high temperature XRD measurement (HT-XRD) of  $\text{NaFePO}_4$  in air, some new reflections start to show up at around  $230^\circ\text{C}$ , as shown in Figure 5.5. To gain a deeper knowledge of these new reflections, Rietveld refinement was conducted on the HT-XRD patterns. Accordingly, a new NASICON phase  $\text{Na}_3\text{Fe}_2(\text{PO}_4)_3$  (space group  $R-3c$ ) was detected (Figure 5.6a). Lattice parameters of  $a$  and  $c$  were determined as  $8.7317(2)$  and  $21.6663(2)$  Å, respectively. Partial oxidization of  $\text{NaFePO}_4$  was proposed to occur during the heating under air. The lattice parameters were determined as a

function of temperature (Figure 5.6b), where  $a$ ,  $b$ , and  $c$  first increased with increasing temperature and again decreased to  $a = 6.8783(2)$ ,  $b = 8.9831(2)$ , and  $c = 5.0478(2)$  Å when the temperature was cooled down, showing a reversible structural stability of the main phase.

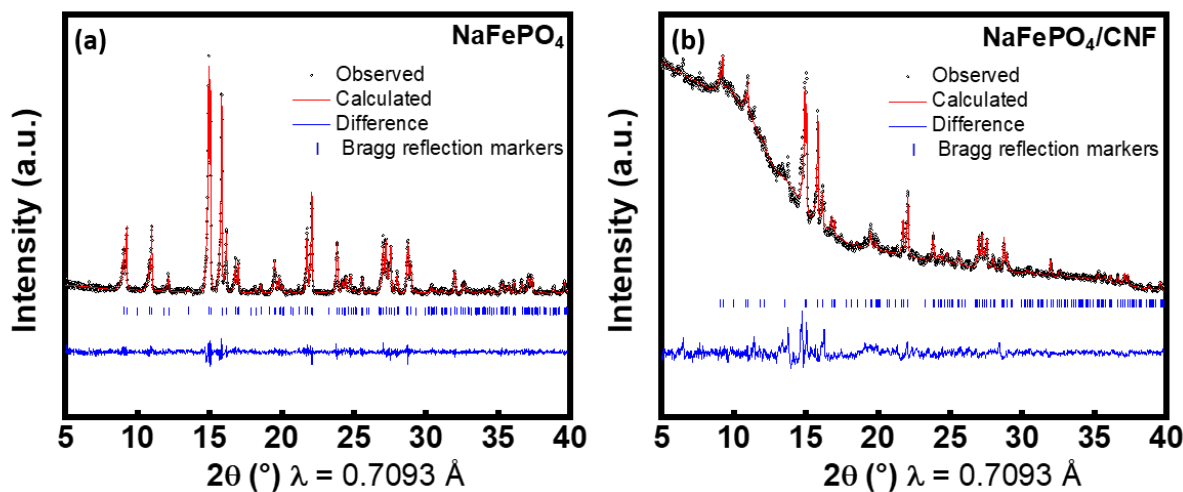


**Figure 5.4** XRD patterns of (a) pristine NaFePO<sub>4</sub> nanoparticles and (b) NaFePO<sub>4</sub>/CNF cathodes.

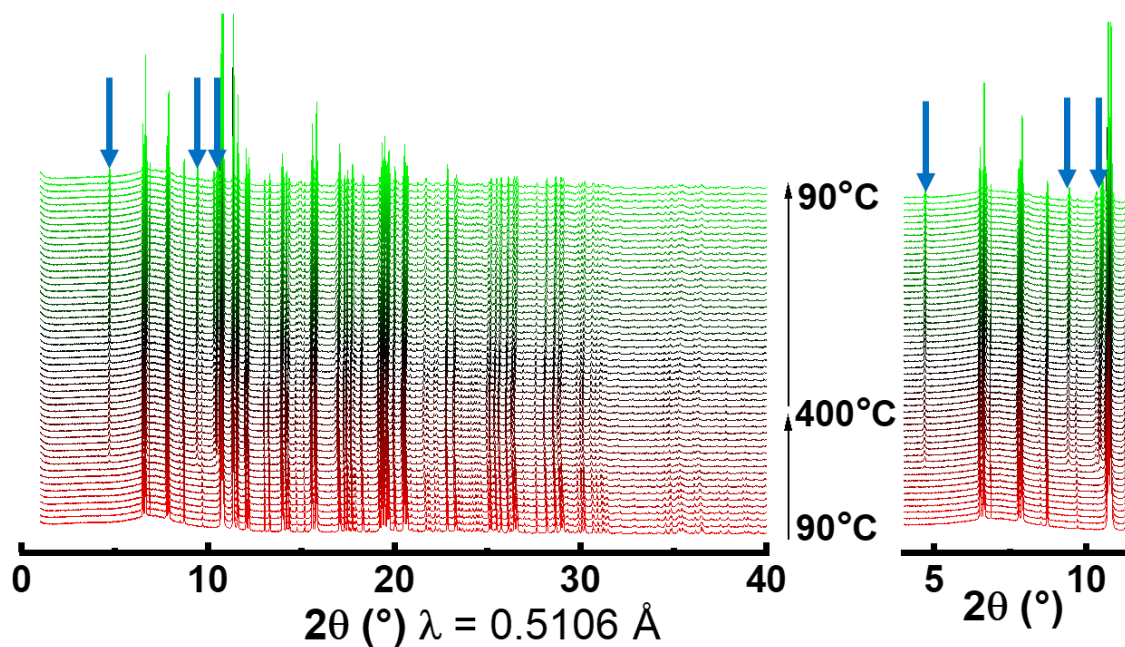


**Figure 5.5** High temperature XRD patterns of pristine NaFePO<sub>4</sub> nanoparticles heated in air. On the right is the enlarged area to emphasize the appearance of the new reflections upon heating, indicated by the blue arrows.

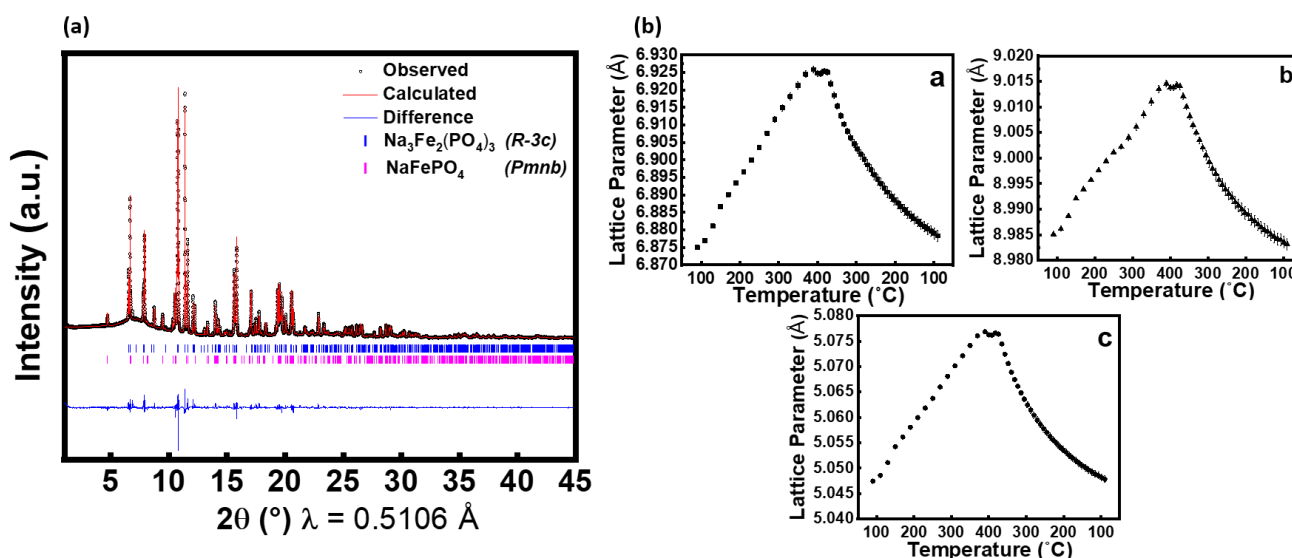


**Figure 5.6** (a) XRD pattern recorded after the sample had been cooled down from 400 °C to 90 °C and (b) lattice parameters  $a$ ,  $b$ , and  $c$  of  $\text{NaFePO}_4$  ( $Pmnb$ ) as a function of temperature.

## 5.2.2 Electrochemical performance

To obtain a fundamental knowledge of the electrochemical mechanism of the composite  $\text{NaFePO}_4/\text{CNF}$  cathode, it is important to study each component's contribution to the total capacity. With the high surface area resulting from carbon nanofibers and nanoparticles, the electrospun  $\text{NaFePO}_4/\text{CNF}$ 's electrochemical behavior followed a different charge storage mechanism from a typical diffusion-controlled intercalation material.<sup>155</sup> The energy storage mechanism of such materials can usually be divided into two parts: a charging process occurring at the surface of the material which is referred to as the pseudocapacitive effect and the sodium ion intercalation process along with redox reactions.<sup>151</sup> Cyclic voltammetry (CV) curves at different sweep rates can provide information on the surface-controlled (capacitive) and diffusion-controlled (bulk) processes.<sup>156</sup> Voltammetry at scan rates from  $0.05 \text{ mV s}^{-1}$  to  $1 \text{ mV s}^{-1}$  at a voltage window of 1.5 - 4.5 V were performed. From the CV curves shown in Figure 5.7, a pair of broad redox peaks appears at 3.1 V and 2.7 V indicating the redox reaction of  $\text{Fe}^{2+} \rightleftharpoons \text{Fe}^{3+} + \text{e}^-$ . The capacitive effect in the system can again be analyzed based on equation (4.1).

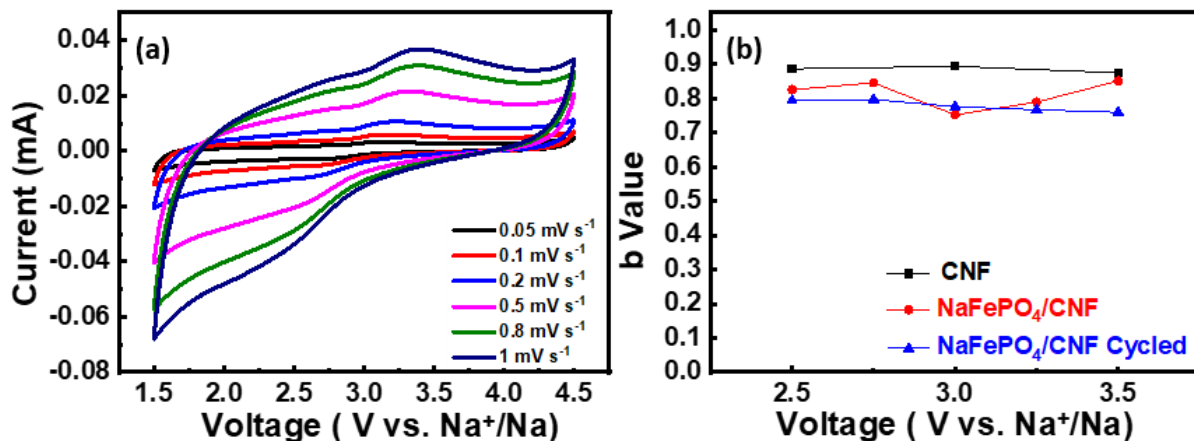


**Figure 5.7** (a) CV curves at various scan rates from 0.05 mV s<sup>-1</sup> to 1 mV s<sup>-1</sup> and (b) *b* values at different potentials of pure CNF, pristine NaFePO<sub>4</sub>/CNF electrodes and cycled NaFePO<sub>4</sub>/CNF electrodes.

In the well-defined conditions, when  $b = 0.5$ , the current is diffusion-controlled indicating a faradaic intercalation process; while, for  $b = 1$ , the current is surface-controlled indicating a capacitive process.<sup>157</sup> The  $b$  values as a function of potentials for NaFePO<sub>4</sub>/CNF and pure CNF are shown in Figure 5.7b. We can see that, at 3.0 V, the  $b$  value for NaFePO<sub>4</sub>/CNF is 0.75 while for CNF it is 0.89. This indicates that in NaFePO<sub>4</sub>/CNF, the current originates partially from the Na<sup>+</sup> ion intercalation reaction other than surface charging effect. Thus, the storage mechanism of the electrospun NaFePO<sub>4</sub> is a mixed type with both diffusion-controlled and capacitive-controlled contributions.

In addition, a detailed examination of the voltammetry enables the quantitative calculation of the contribution of capacitive energy storage according to equation (5.1), with  $k_{1V}$  and  $k_2V^{0.5}$  corresponding to the current contributions from the capacitive surface effect and diffusion-controlled intercalation process. By determining  $k_1$  and  $k_2$ , one can quantify the fraction of the current from each contribution. As shown in Figure 5.8, the capacitive effects contribute to about 32.5%, 49.9%, and 60.0% at scan rates of 0.25 mV s<sup>-1</sup>, 0.5 mV s<sup>-1</sup>, and 1 mV s<sup>-1</sup>, respectively. Hence, as expected, the capacitive effect becomes more dominant with increasing scan rate.

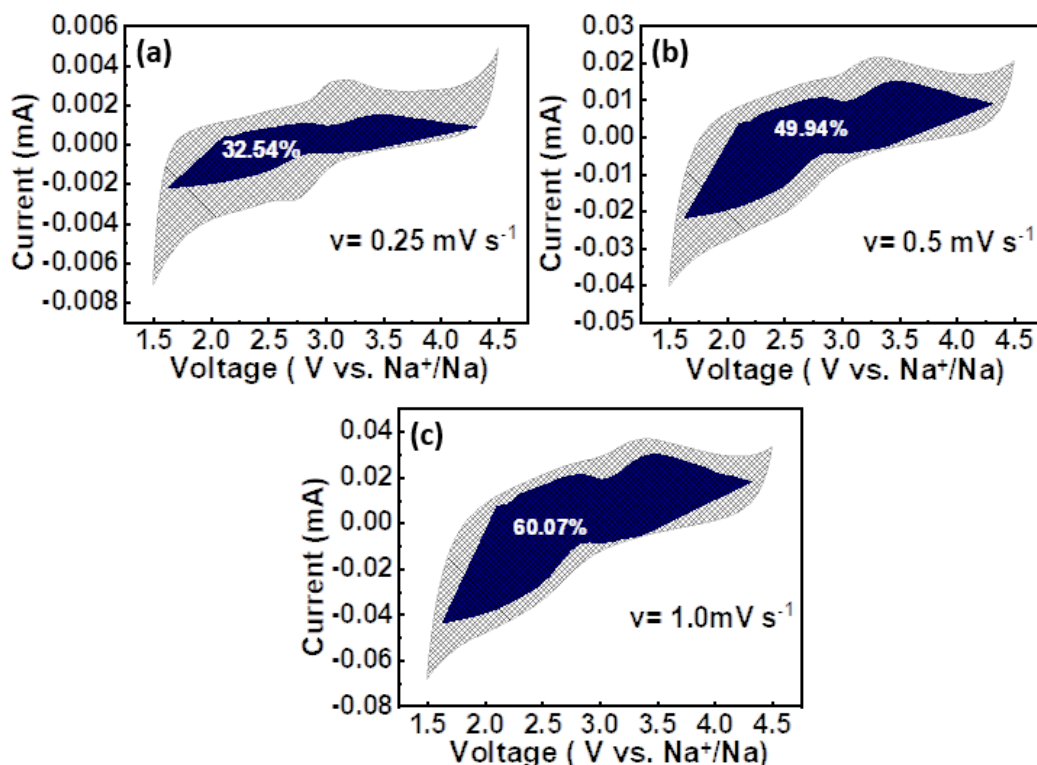


**Figure 5.8** The contribution of capacitive (blue) and diffusion-controlled (grey) capacities to the total capacity for NaFePO<sub>4</sub>/CNF electrodes at different scan rates: (a) 0.25 mV s<sup>-1</sup>, (b) 0.5 mV s<sup>-1</sup>, and (c) 1.0 mV s<sup>-1</sup>.

$$|i_v| = k_1 v + k_2 v^{0.5}$$

$$|i_v|/v^{0.5} = k_1 v^{0.5} + k_2 \quad (5.1)$$

The charge-discharge profiles of the electrospun electrodes are shown in Figure 5.9 at a C rate of 0.1C at a potential range between 1.5 V and 4.5 V. Different from olivine LiFePO<sub>4</sub> and NaFePO<sub>4</sub>, which have a voltage plateau from first phase transition, this sloping curve of maricite NaFePO<sub>4</sub> is indicative of a different sodium-ion insertion/extraction mechanism, which can result from solid-solution behavior or second order phase transitions.<sup>52</sup> The specific discharge capacities are calculated based on the mass of active material NaFePO<sub>4</sub>, which is 30% of the full electrode weight. As we can see, the discharge capacity is increasing from 42 mAh g<sup>-1</sup> in the initial cycle up to 108 mAh g<sup>-1</sup> in the 200<sup>th</sup> cycle and then it is almost constant. Such an increasing capacity phenomenon was observed in many carbon containing cathode material in SIBs with high surface

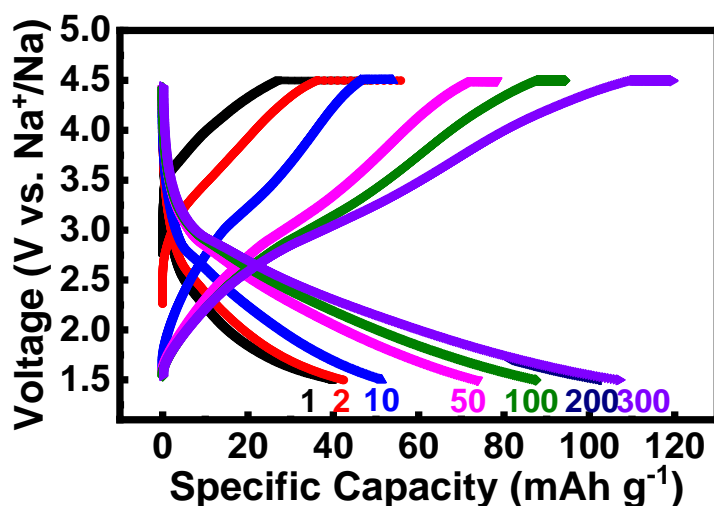


**Figure 5.9** Charge-discharge curves of the NaFePO<sub>4</sub>/CNF electrodes at a current of 0.1C.

areas.<sup>46,111,158</sup> Unfortunately, the observed increase of capacities during initial cycles lack possible suggestions and explanations. The following reasons for this increasing capacity phenomenon can be considered: 1) carbon nanofibers break upon cycling which generates more defects and storage sites for electrons. 2) with active material particles embedded in the carbon nanofibers, the mechanical breakdown of fibers increases contact between NaFePO<sub>4</sub> particles and electrolyte hence further facilitates the accessibility of particles by ions.

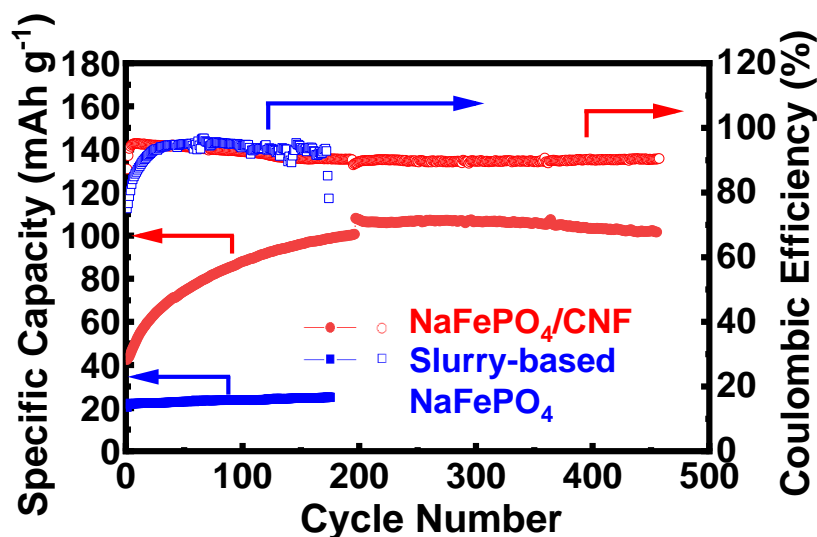


**Figure 5.10** Cycling stability of NaFePO<sub>4</sub>/CNF with the comparison of slurry-based NaFePO<sub>4</sub> at 0.1C.

Other than electrospun NaFePO<sub>4</sub>/CNF, a slurry made of NaFePO<sub>4</sub>, Super P and poly (vinylidene fluoride) (PVdF) with the same 30 wt% weight percentage of NaFePO<sub>4</sub> was also prepared and coated onto the surface of Al foil, labelled as slurry-NaFePO<sub>4</sub>. The long-term performances of NaFePO<sub>4</sub>/CNF and slurry-NaFePO<sub>4</sub> are shown in Figure 5.10 with columbic efficiencies. After the initial increase in capacity, the NaFePO<sub>4</sub>/CNF electrode reaches a capacity of 108 mAh g<sup>-1</sup> after 200 cycles at 0.1C (≈ 15 mA g<sup>-1</sup>). In the following cycles, the electrode showed a good long-term cycling stability with 94.4% retention after 450 cycles, compared with the maximum value of 100% after 200 cycles. In comparison, a capacity of only 24 mAh g<sup>-1</sup> was achieved for slurry-NaFePO<sub>4</sub> and a cell failure occurred within 200 cycles demonstrating the positive role of carbon nanofibers in electrochemical performance enhancement of maricite NaFePO<sub>4</sub>.

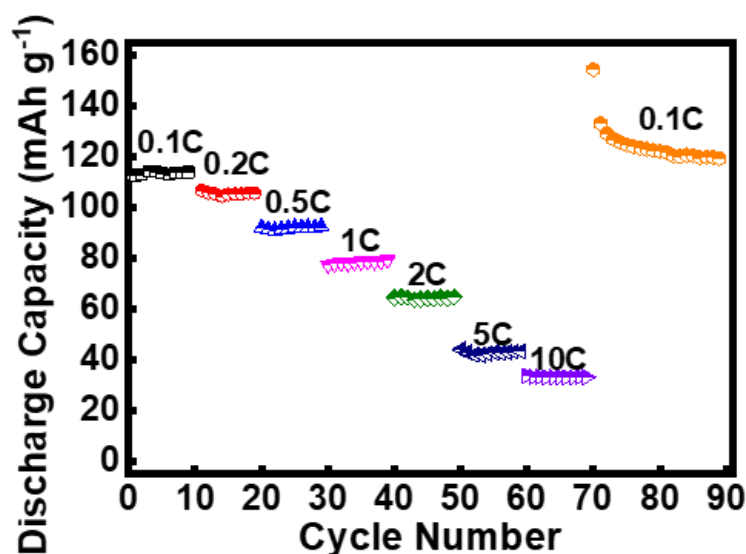


**Figure 5.11** Rate capability of NaFePO<sub>4</sub>/CNF at different current rates: 0.1C, 0.2C, 0.5C, 1C, 2C, 5C and 10C.

The rate capability of the electrospun electrodes was also investigated shown in Figure 5.11. Considering the increasing capacity in the first cycles, the electrode was cycled for over 150 cycles until the capacity reached a stable specific discharge capacity of 113.6 mAh g<sup>-1</sup> at 0.1C. Afterwards, different C rates were applied delivering reversible capacities of 106.3 mAh g<sup>-1</sup> at 0.2C, 92.0 mAh g<sup>-1</sup> at 0.5C, 78.6 mAh g<sup>-1</sup> at 1C, 64.4 mAh g<sup>-1</sup> at 2C, 43.0 mAh g<sup>-1</sup> at 5C and 33.3 mAh g<sup>-1</sup> at 10C, respectively. Importantly, when the cells were cycled back at 0.1C afterwards, a higher capacity up to an average of 124.7 mAh g<sup>-1</sup> was recovered, which indicates a good high rate capability and

a reasonable tolerance of rapid Na<sup>+</sup> ion insertion/extraction process. The specific capacity increased when the cell was brought back to 0.1C from higher currents (124.7 mAh g<sup>-1</sup>) compared to the first cycles at 0.1C (113.6 mAh g<sup>-1</sup>). This increase may be caused by an ongoing activating process.

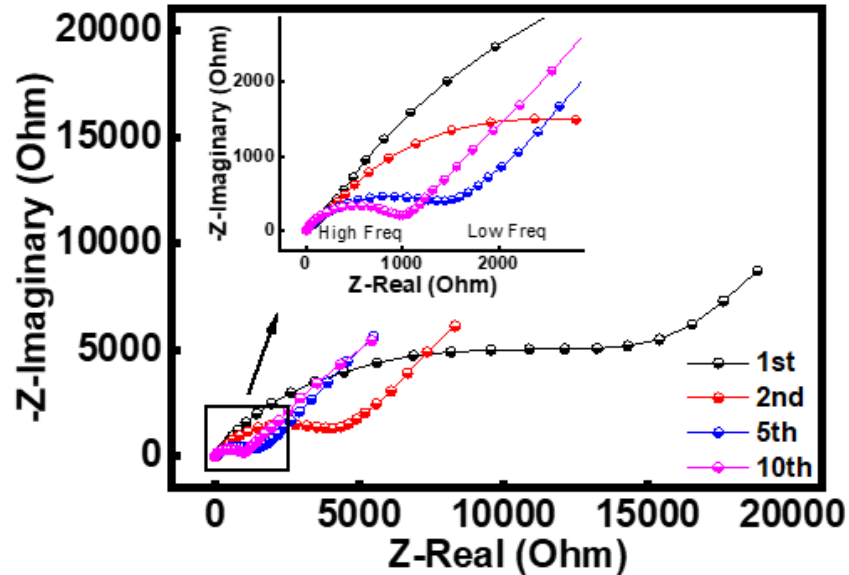


**Figure 5.12** Electrochemical impedance spectroscopy of the NaFePO<sub>4</sub>/CNF electrodes at discharged state (0.01 V): at 1<sup>st</sup>, 2<sup>nd</sup>, 5<sup>th</sup>, and 10<sup>th</sup> cycle.

The electronic conductivity and its changes during cycling of the NaFePO<sub>4</sub>/CNF electrode were analyzed by EIS. The Nyquist plots in Figure 5.12 are consisting of a semicircle in high frequency range, which is due to the ohmic resistance and charge transfer resistance, and a short inclined line in low frequency range, which is from the ionic diffusion within the electrodes.<sup>159</sup> The first part of the semicircles from each cycle at high frequency are overlapping, which can be from the solid electrolyte interface (SEI) formation within the first cycles. We can also observe that in the Nyquist plots, the diameters of the semicircle of the electrodes decrease noticeably over cycles, which demonstrates that the charge transfer grows faster and easier upon cycling within the first 10 cycles. The increasing conductivity also indicates an activation process of the electrodes upon charge-discharge.

Furthermore, differential capacity diagrams (dQ/dV) shown in Figure 5.13 were plotted by processing the constant current charge-discharge data in the 1<sup>st</sup>, 2<sup>nd</sup>, 50<sup>th</sup>, 100<sup>th</sup>, 200<sup>th</sup>, and 300<sup>th</sup>

cycle. In the initial cycles, no reduction/oxidation reaction peaks show up, indicative of a dominant capacitive behavior of the NaFePO<sub>4</sub>/CNF electrode. Upon cycling, an increasing intensity of broad peaks at around 3 V can be observed, which is well recognized with the gradual interaction of NaFePO<sub>4</sub> in the electrochemical behavior of the composite electrode, again confirming the gradual redox activation of Fe<sup>3+</sup>/Fe<sup>2+</sup> in NaFePO<sub>4</sub>. Moreover, the separation of oxidation/reduction peaks is reduced in the first 100 cycles indicating a reduced polarization.

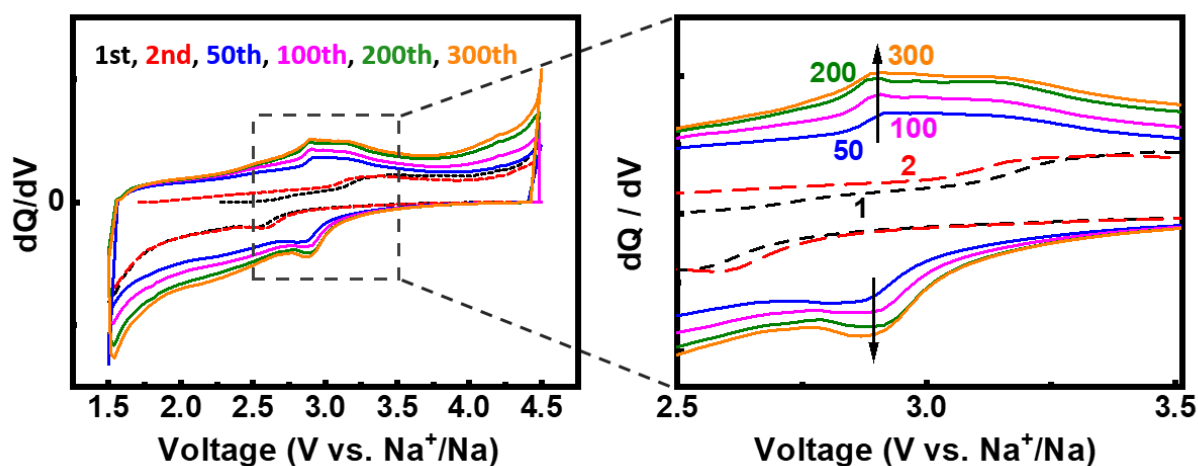


**Figure 5.13** dQ/dV plots of NaFePO<sub>4</sub>/CNF electrodes at initial, 2<sup>nd</sup>, 50<sup>th</sup>, 100<sup>th</sup>, 200<sup>th</sup> and 300<sup>th</sup> cycles processed from charge-discharge curves with enlarged area on the right.

Additionally, the NaFePO<sub>4</sub>/CNF electrodes carbonized at a higher temperature were also briefly studied. The intention was to increase the electronic conductivity of the self-standing electrode by introducing a higher graphitic carbon structure of CNFs from a higher temperature. However, seen from Figure 5.14, the XRD patterns showed a dramatic phase change compared to NaFePO<sub>4</sub>/CNF prepared at 600 °C. Accordingly, the morphology presented an agglomeration of the nanoparticles, losing their original crystalline boundaries. The CV curves showed no redox peaks at around 3 V indicating the active material has changed its structure and became inactive in the electrochemical behavior. Thus, the temperature of 600 °C was proved to be suitable for preparing maricite NaFePO<sub>4</sub>/CNFs composite electrodes.

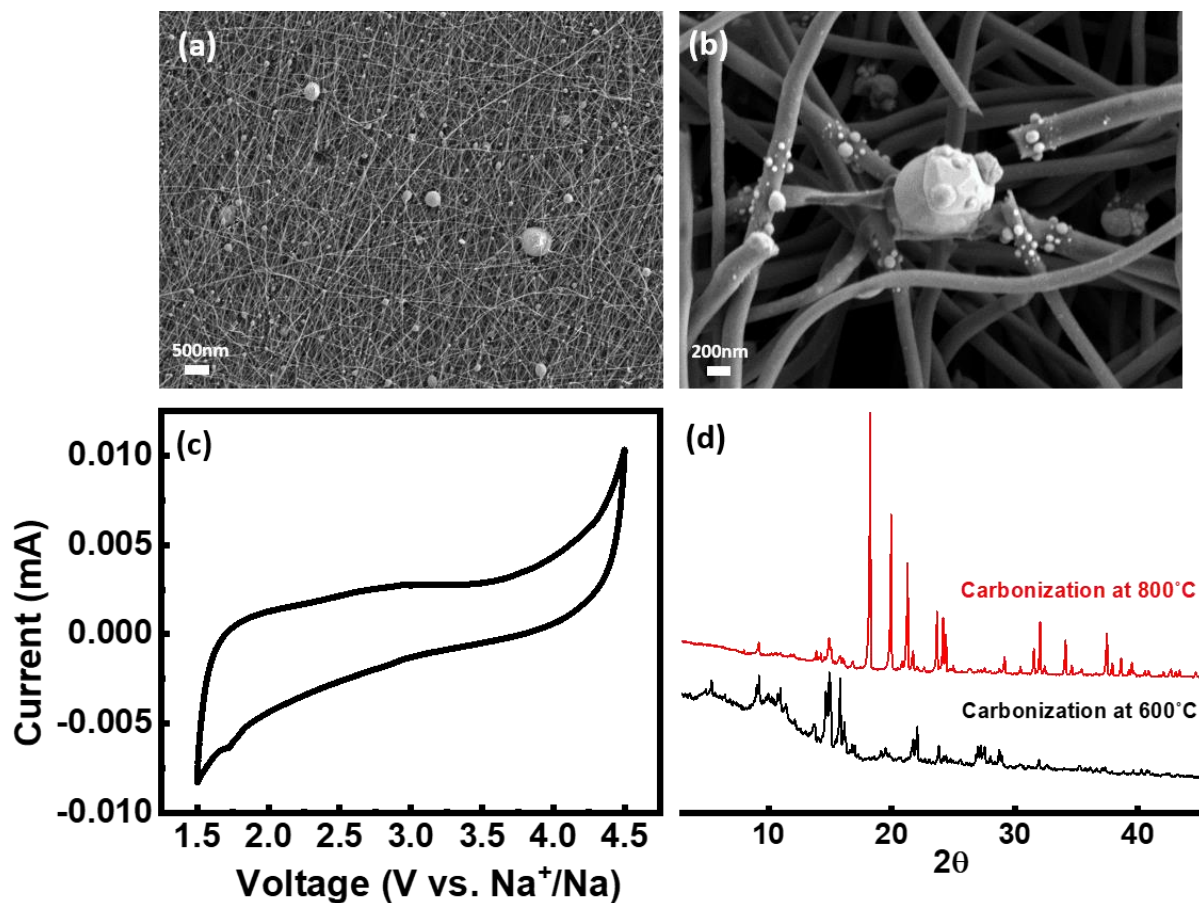


**Figure 5.14** NaFePO<sub>4</sub>/CNF electrodes carbonized at 800 °C: (a-b) SEM pictures, (c) CV curves at the scan rate of 0.1 mV s<sup>-1</sup> and (d) XRD patterns compared with the electrode carbonized at 600 °C.

### 5.2.3 *Ex situ* studies

The activation of NaFePO<sub>4</sub> in NaFePO<sub>4</sub>/CNF electrodes was further confirmed by *ex situ* analysis of the samples after cycling. The Mössbauer spectra shown in Figure 5.15 demonstrate distinguished phases or sites in the respective samples. The intensities of Fe<sup>2+</sup> and Fe<sup>3+</sup> peaks were fitted to estimate the amount of each oxidation state in the samples of pristine, initial charged, initial discharged, 100<sup>th</sup> cycles charged and 100<sup>th</sup> cycles discharged electrodes. As shown, an average of 36.5% Fe<sup>3+</sup> exists in the pristine electrodes, which is in agreement with the results from HT-XRD showing an impurity phase of oxidized Fe<sup>3+</sup> in Na<sub>3</sub>Fe<sub>2</sub>(PO<sub>4</sub>)<sub>3</sub>. An increase in Fe<sup>2+</sup> content

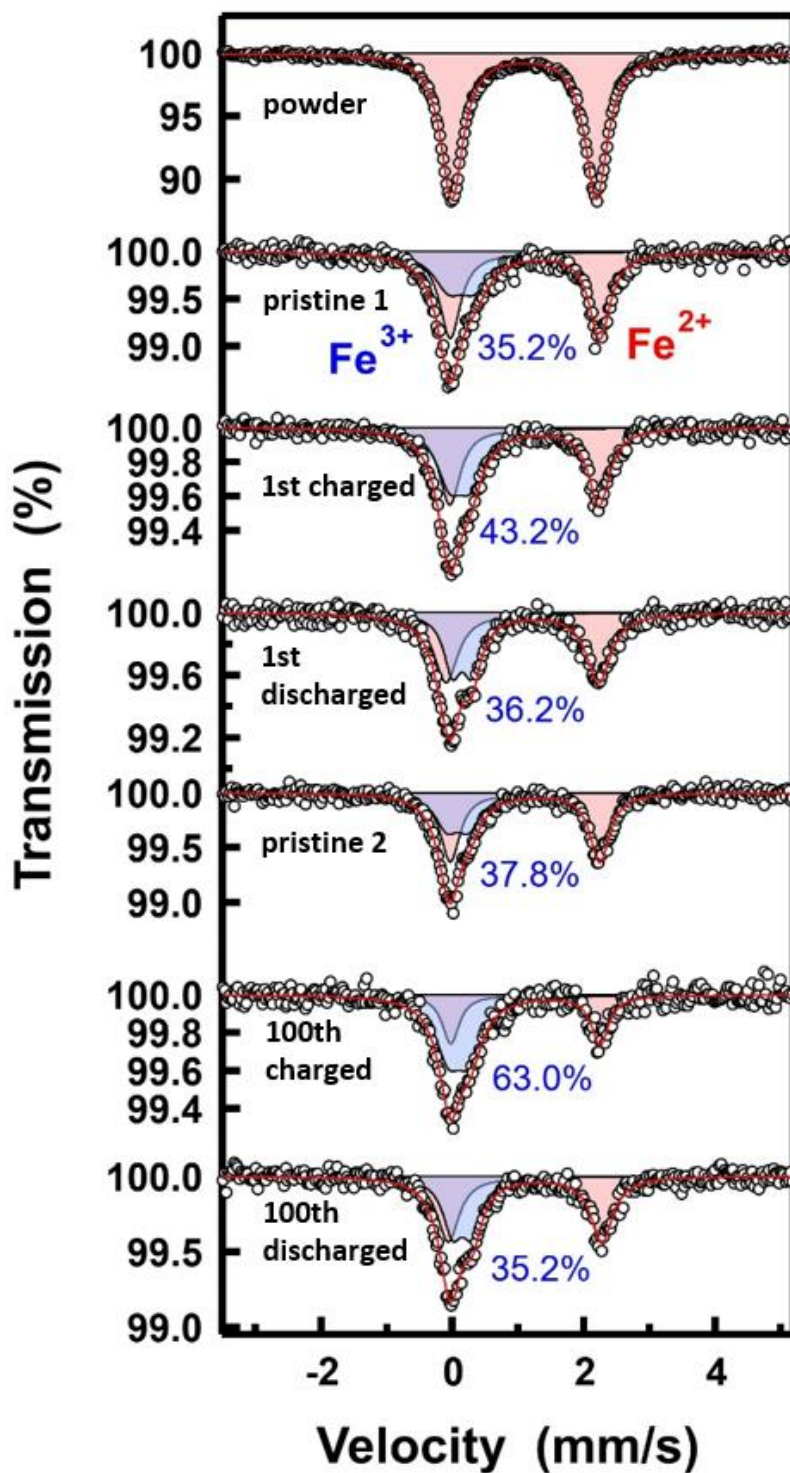


**Figure 5.15** Fe Mössbauer spectra of NaFePO<sub>4</sub>/CNF at different charge states in the first cycle (top) and 100<sup>th</sup> cycle (bottom). Experimental data points are shown as circles, the overall fit as red line and, the Fe<sup>2+</sup> and Fe<sup>3+</sup> sub-spectra are shown as red and blue doublets, respectively.

from 36.2% to 43.2% appears in the first cycle while an increase from 35.2% to 63.0% is observed in the 100<sup>th</sup> cycle, which clearly demonstrates an increased Fe<sup>3+/2+</sup> activity upon extended cycling. This correlates with the results from Figure 5.7b showing smaller *b* values of cycled NaFePO<sub>4</sub>/CNF electrodes compared to the ones of non-cycled NaFePO<sub>4</sub>/CNF, demonstrating a more active Fe<sup>2+</sup> ⇌ Fe<sup>3+</sup> + e<sup>-</sup> redox reaction along cycling.

Raman spectra shown in Figure 5.16 illustrate the structural changes before and after cycling with fitted D and G peaks of carbon. The ratio between I<sub>D</sub> and I<sub>G</sub> is often used as an indication of the degree of disorder/defects in carbonaceous materials.<sup>160</sup> In NaFePO<sub>4</sub>/CNF the intensity ratio of I<sub>D</sub>/I<sub>G</sub> decreased from 0.86 in the pristine state to 0.85 after 100 cycles. A significant structural change did not take place upon charge-discharge cycles, specifying a stable structure of the NaFePO<sub>4</sub>/CNF electrode. The minor decrease of the I<sub>D</sub>/I<sub>G</sub> intensity correlates with the morphology observed by SEM in the cycled electrodes, as shown in Figure 5.17, more cracks and partial defects allowing more NaFePO<sub>4</sub> particles to become exposed and getting in contact with the electrolyte.

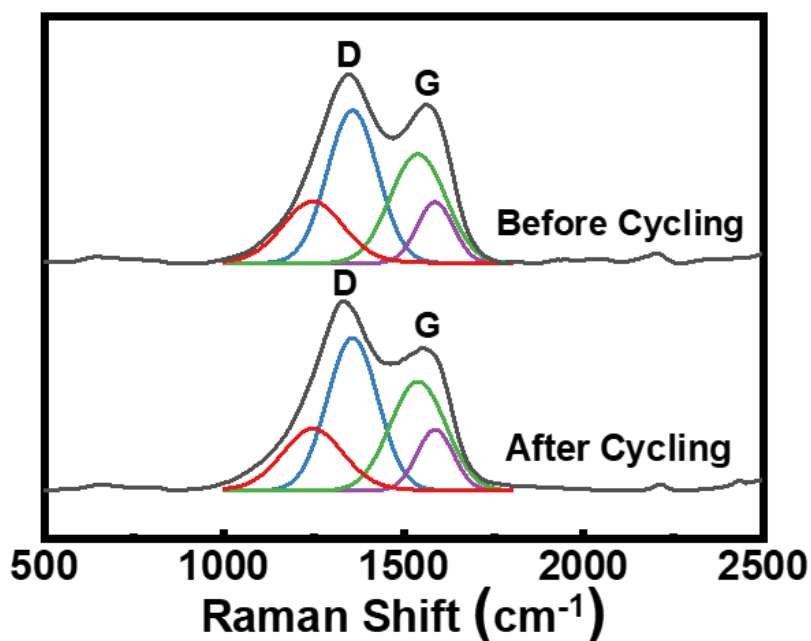


**Figure 5.16** Raman spectra of the NaFePO<sub>4</sub>/CNF electrodes before and after cycling.

Moreover, more defects allow more  $\text{Na}^+$  ion transfer channels for an increased electrochemical performance. Furthermore, as we can see from the SEM images, nanoparticle clusters with clear crystalline boundaries can be observed in pristine electrodes before cycling. However, after cycling the sharp boundaries of the crystalline particles disappeared and transform to an agglomerated morphology. This further proves the involvement of  $\text{NaFePO}_4$  particles in the electrochemical activity. Amorphous phases are observed in the XRD patterns of the samples charged and discharged in the 100<sup>th</sup> cycle, as shown in Figure 5.18: areas marked with orange and green dashed rectangles include reflections with decreasing intensities. By amplifying the reflections in the green marked area, we observe no shift of reflections in the cycled electrodes. A transformation of maricite  $\text{NaFePO}_4$  into a total amorphous phase has been observed from the XRD patterns of the electrodes charged up to 4.5 V or 4.7 V.<sup>37,53</sup> In our  $\text{NaFePO}_4/\text{CNF}$  composite, the gradual activation of  $\text{NaFePO}_4$  should theoretically lead to a gradual structural change. This perfectly explains the incomplete amorphization with retention of a high intensity of crystalline reflections in the electrodes after 100 cycles.

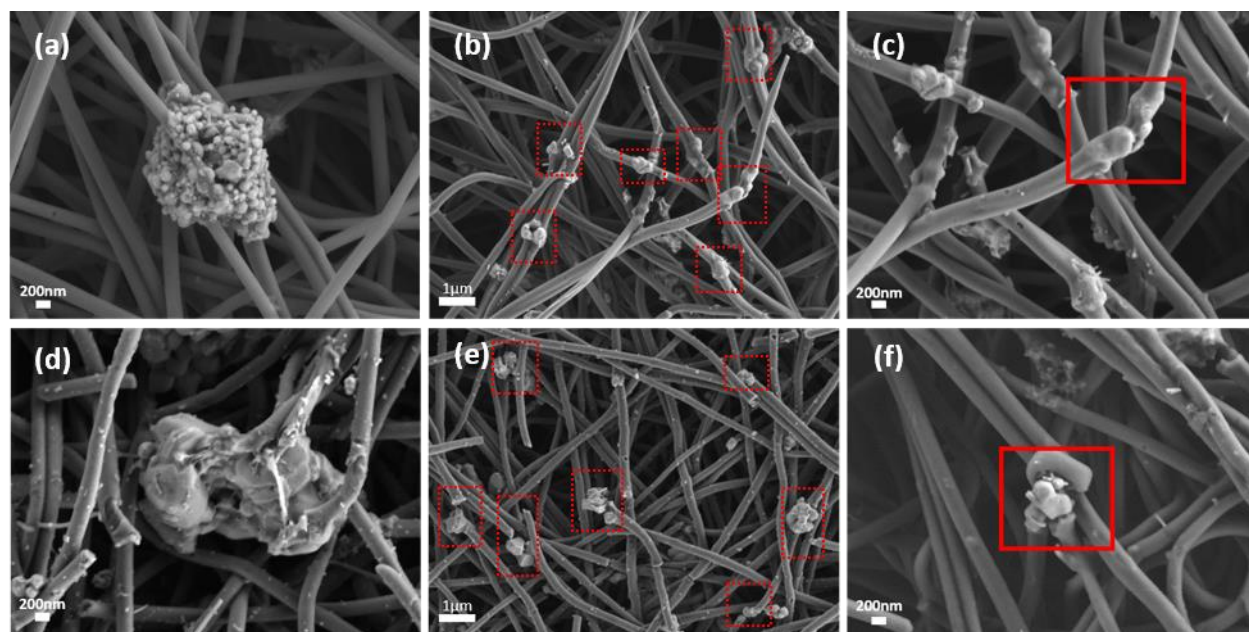


**Figure 5.17** SEM pictures of pristine and cycled  $\text{NaFePO}_4/\text{CNF}$  electrodes.

By comparing the electrodes before and after cycling, we were able to observe the gradual changes in the activity of  $\text{Fe}^{2+} \rightleftharpoons \text{Fe}^{3+} + e^-$  redox reactions and the structures of both the carbon fiber and the maricite NaFePO<sub>4</sub> particles by various experimental methods. These *ex situ* results confirm an activation process of the maricite NaFePO<sub>4</sub> involving the electrochemical behavior with the mechanical breakdown and defect formation of the carbon nanofibers. The activation process corresponds to an increased capacity appearing in the charge-discharge performance of NaFePO<sub>4</sub>/CNF, which provides an insight into the mechanism and the unique behavior of such self-standing carbon integrated maricite NaFePO<sub>4</sub> electrodes.

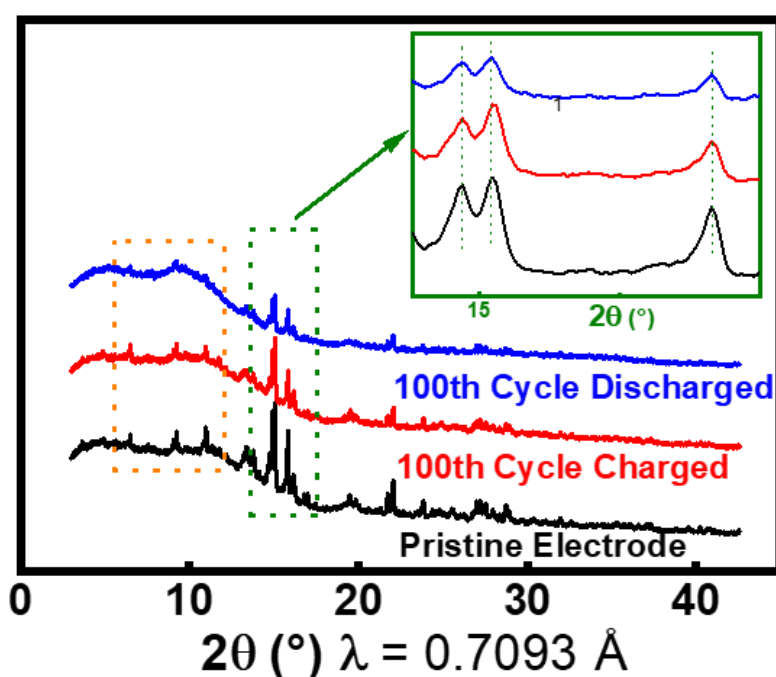


**Figure 5.18** XRD patterns of the pristine and 100<sup>th</sup> cycled NaFePO<sub>4</sub>/CNF electrodes SEM pictures of pristine and cycled NaFePO<sub>4</sub>/CNF electrodes.

### 5.3 Summary

Though the maricite NaFePO<sub>4</sub> is considered as electrochemically inactive, the addition of an electrical conductive carbon nanofiber network results in a long-term cycling stability of NaFePO<sub>4</sub> by offering more diffusion channels for Na<sup>+</sup> ions and electrons. With the help of electrospinning, a self-standing, collector-free, and binder-free maricite NaFePO<sub>4</sub>/carbon nanofiber composite electrode was successfully prepared. A hybrid electrochemical mechanism of capacitive charge

storage and intercalated redox reaction of  $\text{Fe}^{2+} \rightleftharpoons \text{Fe}^{3+} + \text{e}^-$  was confirmed by cyclic voltammograms at different scan rates. The phenomenon of an initially increasing capacity was explained along with *ex situ* measurements demonstrating an activation process of  $\text{NaFePO}_4$  particles in such composite electrodes. Even though a very high capacity was not delivered, this work presents a comprehensive study of such hybrid  $\text{NaFePO}_4$  electrodes for the first time and enlightens the potential of self-standing electrodes in future applications.

## 6 Polyoxometalate/carbon-based modified separator for Mg-S batteries

### 6.1 Experimental part

#### 6.1.1 Material preparation

##### *Chemical preparation*<sup>§</sup>

All the samples were handled in an argon-filled glove box (MBraun) with a recirculation system under a controlled argon atmosphere ( $O_2$ ,  $H_2O < 0.1$  ppm). The chemical operations were carried out either on the bench under Ar (99.9999%) using standard Schlenk techniques (with vacuum  $< 0.1$  Pa) or in a glove box. The glassware was heated with heat gun under vacuum prior to use. Dimethoxy ethane (DME) was distilled over sodium under argon atmosphere and stored over 3 Å molecular sieves in the glove box. The solid  $Mg[B(hfip)_4]_2 \cdot 3DME$  was prepared according to previous works<sup>161,162</sup> and dissolved in a volumetric flask with proper amount of DME for the desired concentration. The molar concentration of the electrolyte is based on the molar mass of  $Mg[B(hfip)_4]_2 \cdot 3DME$ .

##### *Synthesis of $TBA_3[H_3V_{10}O_{28}]$ cluster (= $TBA_3\{V_{10}\}$ )*<sup>§</sup>

$TBA_3[H_3V_{10}O_{28}]$  (V-10 type POM) was synthesized based on the reference.<sup>163</sup> Aqueous HCl (25.0 mL, 3 mol L<sup>-1</sup>) was added drop by drop to an aqueous solution of  $Na_3VO_4$  (5.00 g, 35.0 mL) under stirring. The orange solution was slowly added in an aqueous solution of (*n*-C<sub>4</sub>H<sub>9</sub>)<sub>4</sub>NBr (= TBABr, 20.00 g, 30.0 mL), resulting in a large amount of yellow-orange precipitates. The yellow precipitates were collected by suction filtration, washed successively with 20.0 mL of H<sub>2</sub>O, 20.0 mL of ethanol and 50.0 mL of ether, and finally dried for 3 h under vacuum to yield 3.50 g of yellow-orange solid. The crude material was purified by recrystallization from acetonitrile using diethyl ether diffusion. The yellow-orange crystals were collected by suction filtration, washed with ether, and dried overnight under vacuum to yield 1.00 g (22% based on V) of yellow-orange product.

##### *Preparation of magnesium polysulfide ( $MgS_n$ ) solution*<sup>§</sup>

The mixture of 2.053 g (64.0 mmol) of sulfur powder and 0.194 g (8.0 mmol) of Mg powder was ball-milled at 200 rpm for 10 hours using silicon nitride vial and balls under Argon. Subsequently, the powders were transferred to a glass vial in glove box and added with 30 ml of tetraglyme. The suspension was then stirred at 60 °C for 3 days.  $\text{MgS}_n$  was under formation when the almost clear upper liquid layer started to turn orangey red with some solid residues left after stirring.

#### *Preparation of Ketjen black/sulfur composites<sup>§</sup>*

The composite was prepared by the melt diffusion method. Ketjen black (KB) was dried in a rotating oven at 230 °C under vacuum for at least 24 hours prior to use. Sulfur powder was ball-milled with the KB at a mass ratio of 6:4. Then, the mixture was heated in an autoclave reactor at 160 °C for 20 hours. To remove the bulk sulfur on the surface of the carbon material, the composite was further heated in a closed quartz tube at 300 °C for 1 hour. Subsequently, the sulfur cathode was prepared by casting after mixing the KB/S composite, Super P and PVdF binder in a ratio of 7.5:1.5:1 in N-methyl-2-pyrrolidone (NMP), then coated onto a carbon-coated aluminum foil with a doctor blade. The electrodes were dried under ambient conditions for 24 hours, then under vacuum at 55 °C overnight. The final loadings of active material on the current collector were controlled in a range of 0.8 to 1.2 mg cm<sup>-2</sup>.

#### *Modification of Separator*

POM, Super P and Polyvinylidene (PVdF) were mixed at a mass ratio of 1:6:3 and then dispersed in NMP with the help of a magnetic stirrer for 24 hours. POM and Super P were ground in an agate mortar for 30 minutes beforehand. The mixed solution was then loaded into a 1 mL syringe and then set in a climate-controlled electrospinning machine described in section 4.1.1. The temperature was set at 25 °C, and the humidity was 20%. A high voltage of 18 kV was applied with a flow rate at 0.1 mL/h and 10 cm needle-to-collector distance. A Whatman C type glass fiber separator was taped on aluminum foil covering the collector. The POM contained solution was then dispersed on the surface of the glass fiber separator. Modified separators were then dried in vacuum oven at 80 °C and then punched into smaller size with a diameter of 16 mm for future use. The mass loading of coated material can be controlled by the volume of the injected solution. Samples of es.-5% POM/C and es.-20% POM/C were prepared under the same conditions with a POM, Super P and PVdF mass ratio at 0.5:6.5:3 and 2:5:3 separately.

§ was conducted by Dr. Yuanchun Ji from Helmholtz Institute Ulm (HIU).

## 6.1.2 Material characterization

### *SEM*

The morphology of all the samples was observed with a Merlin thermal field emission scanning electron microscope (FE- SEM) (Carl Zeiss SMT AG). Carbon tapes were used as substrates. The surface of POM-coated separator was peeled off and a 5 nm thick gold/platinum sputtering was applied on top due to its low electrical conductivity. Cycled samples were obtained after cell disassembly, washed with DME, and then dried under vacuum at 65 °C in a glovebox for 2 hours prior to the test. A vacuum transport tube was used for transferring the cycled *ex situ* samples.

### *EDX*

Energy-dispersive X-ray spectroscopy (EDX) was performed to confirm the elemental compositions (Brucker Quantax, 400 SDD). The accelerating voltage was 10 kV which is high enough to excite the  $K\alpha$  line of vanadium (4.949 keV). No sputtering was used to coat any of the samples.

### *TGA*

Simultaneous thermogravimetric analysis, differential scanning calorimetry and mass spectrometry (TGA-DSC-MS) were conducted with a Setaram thermal analyzer SENSYS evo TGA-DSC equipped with a Pfeiffer OmniStar mass spectrometer for the analysis of the evolved gas to determine the sulfur loading of the cathode material for Mg-S batteries.

### *ICP-OES*

The concentration of  $MgS_n$  solution used in H-cells and immersion experiment was determined for three times by inductively coupled plasma optical emission spectroscopy (ICP-OES, OPTIMA 4300 DV, PerkinElmer). The solution was first prepared in a 10-fold dilution with tetraethylene glycol dimethyl ether and then dissolved in  $HNO_3$  in a microwave.

### *XPS*

The XPS spectra were acquired using a Thermo Scientific K-alpha spectrometer. The samples were analyzed using a microfocused, monochromated Al  $K\alpha$  X-ray source (1486.6 eV, 400  $\mu m$  spot size). XPS spectra were recorded with a concentric hemispherical analyzer at a pass energy of 50

eV and fit with one or more Voigt profiles (binding energy uncertainty:  $\pm 0.2$  eV) and Scofield sensitivity factors were applied for quantification using the Avantage software package.<sup>164</sup> All spectra were referenced to the S 2p peak (S-S bond) at 164.0 eV binding energy controlled by means of the photoelectron peaks of metallic Cu, Ag, and Au, respectively. To check for sample degradation during the measurements, repeated Sulfur (S2p) spectra were recorded. The measurements were performed on samples from the second electrochemical cycle.

### 6.1.3 Electrochemical performance

The fabrication of all electrodes and the construction of the electrochemical cells were carried out in an argon-filled glovebox. Cyclic voltammetry (CV) and linear sweep voltammetry (LSV) were measured using a Biologic VMP-3 potentiostat using a three-electrode PAT-Cell with Mg foil (99.9%) as both the reference and counter electrodes. The cells were operated using galvanostatic methods at various current densities. The Mg-S batteries were assembled using coin-type cells with the KB/S cathode with a sulfur loading of approximately  $1 \text{ mg cm}^{-2}$ , a borosilicate glass fiber (Whatman GF/C) or a POM-coated separator soaked with liquid electrolyte, and Mg foil as the anode. The cells were placed in an incubator to maintain a constant temperature of  $25 \pm 0.1$  °C and tested using an Arbin battery cycling unit.

## 6.2 Results and discussions

### 6.2.1 Morphology and structure

Mg-S batteries (MSBs) with electrospun modified POM/C glass fiber separator (abbreviated as es.-POM/C hereafter) were assembled by using Ketjen black/sulfur composite as cathode,  $\text{Mg}[\text{B}(\text{hfip})_4]_2/\text{DME}$  as electrolyte<sup>161,162</sup> and magnesium metal disc as anode. Specifically, the Ketjen black (KB) was used as conductive carbon matrix to host elemental sulfur through a well-known “heat impregnation” process at the temperature of 160 °C. Then the KB/S composite was heated at 300 °C for 1 h to remove the superficial sulfur, resulting in a S-loading of around 50 wt% shown in Figure 6.1. The non-corrosive and highly efficient  $\text{Mg}[\text{B}(\text{hfip})_4]_2$  electrolyte, developed by Zhao-Karger *et al.*, was dissolved in pure DME solvent with a concentration of 0.3 M. Before electrospinning, mixture of POM, Super P and Polyvinylidene (PVdF) was ground manually at a

mass ratio of 1:6:3 for 30 minutes, then dispersed in *N*-methyl-2-pyrrolidone (NMP). The mixture solution was then loaded and electrospun onto a Whatman C type separator. A homogeneous coating on the glass fiber separator was observed with a mass loading of 20 mg (10 wt% POM, 60 wt% Super P and 30 wt% PVdF), namely es.-POM/C. As illustratively shown in Scheme 6.1, a proposed “Polysulfide-phobic” mechanism was attributed by the synergistic effect of V-rich decavanadate clusters and conductive carbon. Theoretically, the coated side of the separator was immobilized with polysulfides through an intramolecular V-S<sub>n</sub><sup>2-</sup> interaction, which hence acted as a shielding layer towards further released long-chain polysulfides upon discharging from cathode S<sub>8</sub>. In this circumstance, the confined long-chain polysulfides in the area between cathode and es.-POM/C side went through a reutilization process, which significantly promoted the redox activities of sulfur species and enhanced the coulombic efficiency of battery cycling.

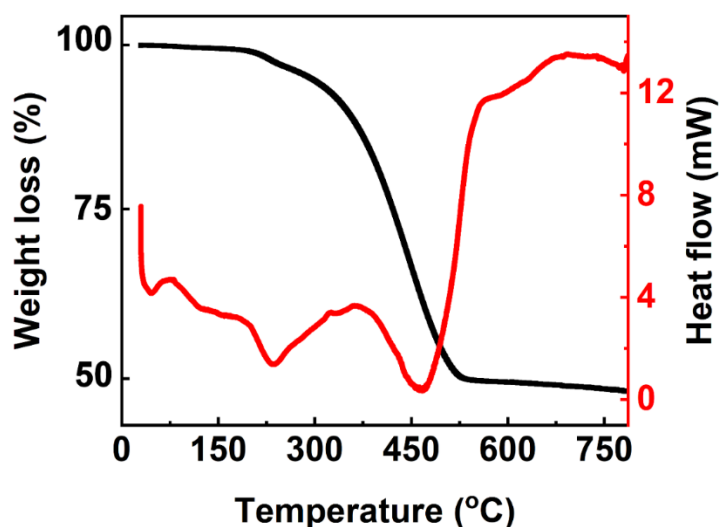
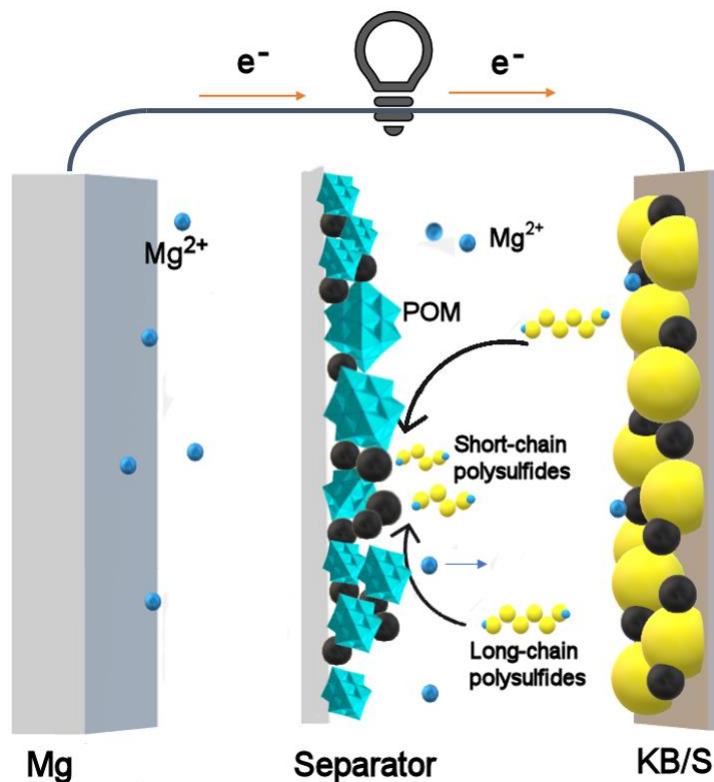


**Figure 6.1** Thermogravimetric analyses (TGA) of KB/S cathode material.



**Scheme 6.1** Schematic illustration of inhibiting “shuttle effect” by electrospun POM/Carbon separator in MSBs.

As shown in Figure 6.2, SEM images showed the structure of the as-fabricated functional separator. Compared with pristine glass fiber (Figure 6.2a), the coated surface of es.-POM/C was homogeneously covered with well-defined nanoparticles (Figure 6.2b and c), which is further confirmed by EDX mapping of elements C, O and V, the compositions of POM and Super P carbon. Nanofibers from the polymer PVdF serve as skeletons for particle dispersion. In addition, Figure 6.3 shows the particle size distribution of observed Super P and POM composites indicating an average size of 50 nm.

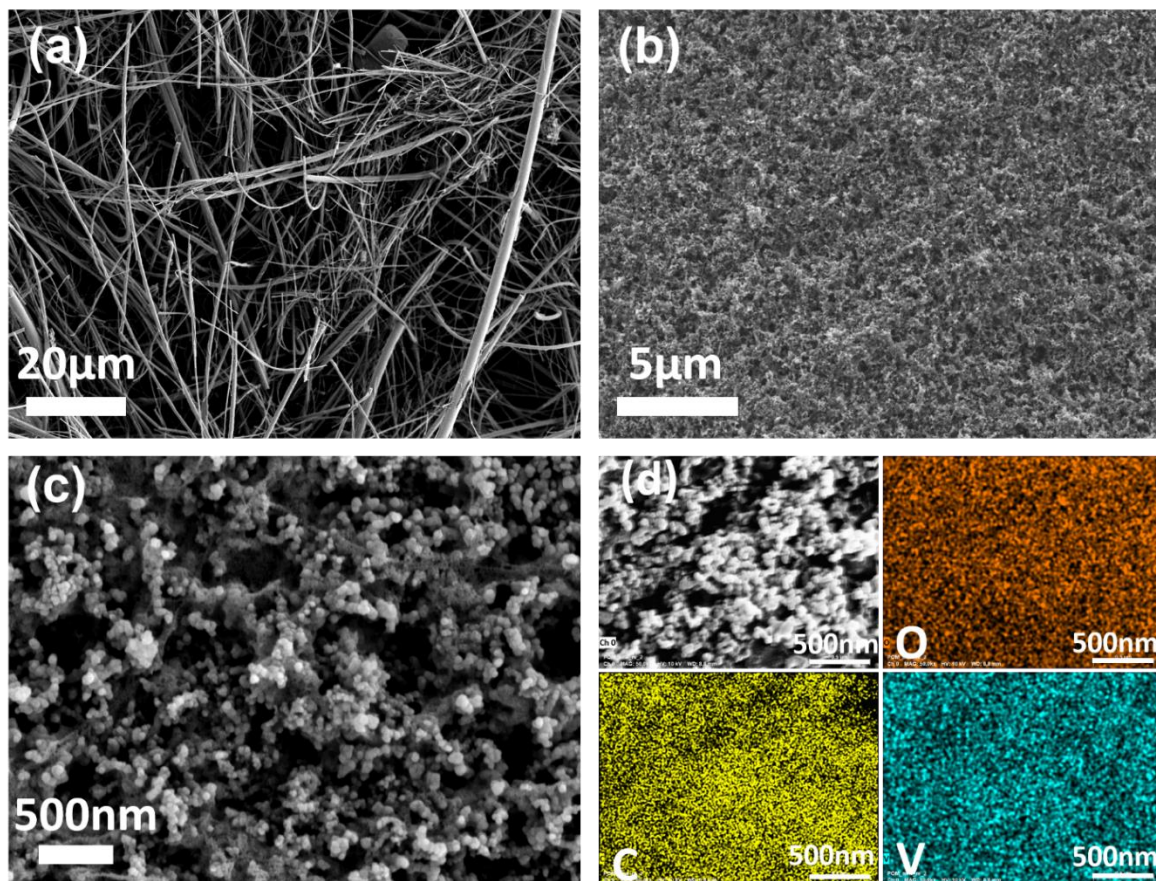


**Figure 6.2** SEM images of (a) pristine Whatman glass fiber; (b,c) es.-POM/C separator and (d) EDX mapping of element oxygen, carbon and vanadium of a selected area in es.-POM/C separator.

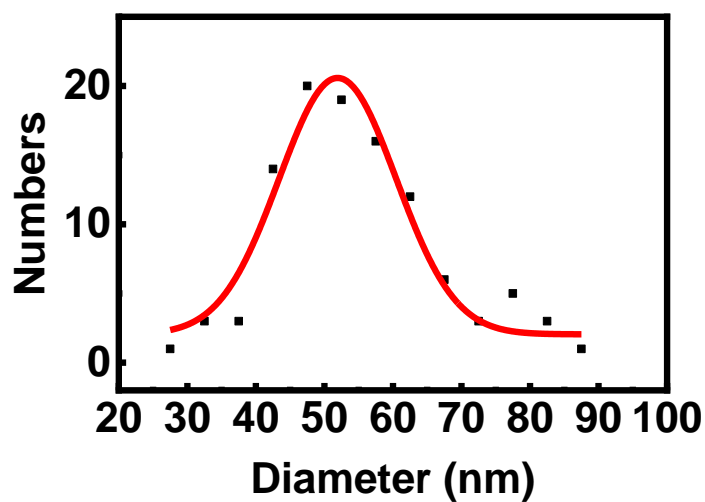


**Figure 6.3** Particle size distribution of nanoparticles observed on the coating layer.

Visualized H-type glass devices were designed and assembled to demonstrate the feasibility of es.-POM/C separator on the suppression of polysulfide shuttling. As shown in Figure 6.4, tetraglyme solution of  $\text{MgS}_n$  (0.04 M, based on  $\text{Mg}^{2+}$ ) was injected in the left chamber and pure tetraglyme solvent on the right. The concentration of  $\text{MgS}_n$  in the solution was determined with ICP measurement. The H-type cells in the upper row were assembled with a pristine Whatman glass fiber separator, while the ones in the lower row were implemented with an es.-POM/C separator. In the cells with pristine glass fiber, the red-brown polysulfides gradually passed through the separator from left to right and reached a high level after 24 h. In the contrary, no obvious polysulfide diffusion was observed from the H-type cells with es.-POM/C separators after the same period of time. After 96 h, a slight color change in the right chamber can be seen, which indicated that the es.-POM/C separators exhibited a better suppression of polysulfide diffusion than pristine glass fibers.

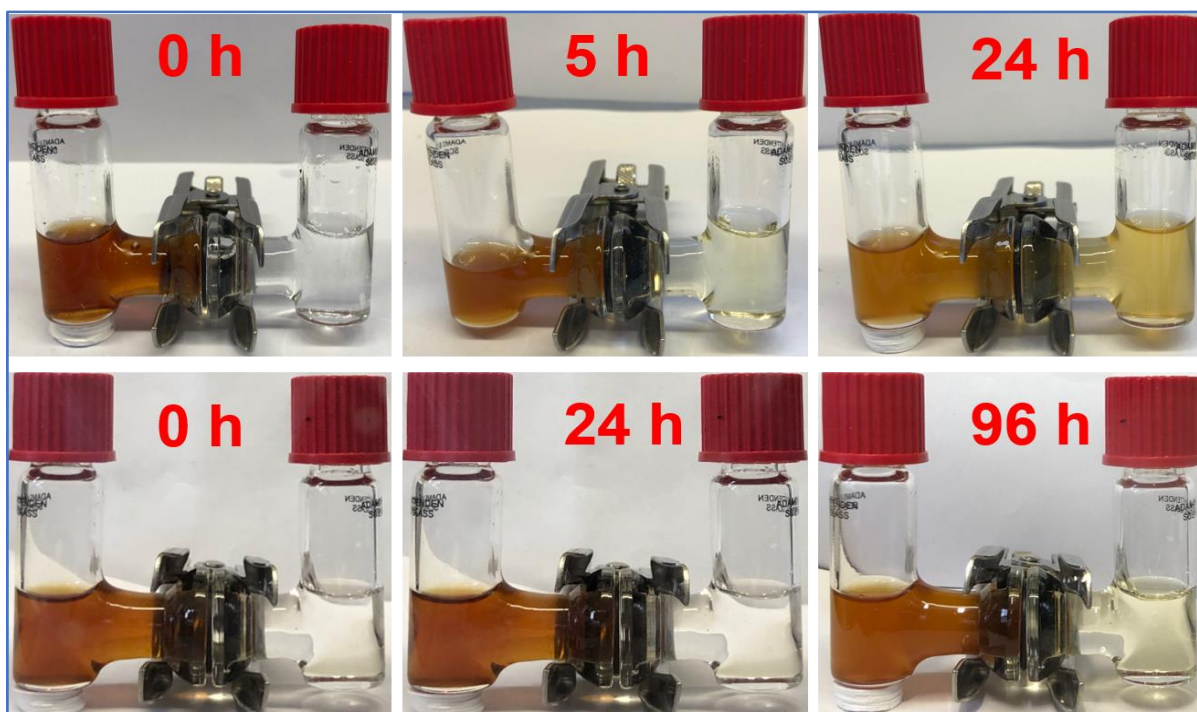


**Figure 6.4** Permselectivity of the es.-POM/C separator. Optical images of the diffusion of polysulfides: visualized H-type glass devices with a pristine Whatman glass fiber separator (top) and a es.-POM/C separator (bottom). The tetraglyme solvent with 0.04M  $\text{MgS}_n$  was injected in the left chamber and the solvent without polysulfides was injected in the right chamber.

## 6.2.2 Electrochemical performance

To verify the function of the es.-POM/C separator in enhancing battery cycling stability, different coin-type cells were assembled with pristine glass fiber, es.-Super P carbon (es.-C) and es.-POM/C as separators, respectively. The KB/S slurry was coated on an aluminum foil by doctor blade method with sulfur loading of approximately  $1 \text{ mg cm}^{-2}$ . The initial cycles of galvanostatic charge-discharge profiles with pristine glass fiber displayed a relatively flat discharge voltage plateau at about 1.5 V, followed by a sloping region until a cutoff voltage of 0.5 V, indicating a stepwise reaction pathway (Figure 6.5a). Notably, the discharge potential plateau slightly increased after the first cycle, accompanied with an obviously increased coulombic efficiency. However, the battery decayed very quickly after 10<sup>th</sup> cycle from an initial capacity of  $460 \text{ mAh g}^{-1}$  to finally  $\sim 310 \text{ mAh g}^{-1}$  at 0.1C ( $\sim 167 \text{ mA g}^{-1}$ ).

Figure 6.5b shows the discharge-charge profiles of the MSB with es.-C as separator indicating a promoted cycling performance, even though the battery cycling ended up with a discharge capacity of  $190 \text{ mAh g}^{-1}$  at 30<sup>th</sup> cycle. Same as the battery with pristine glass fiber, the one with es.-C also showed a flat discharge voltage plateau at about 1.5 V and followed by a sloping region until 0.5 V. Besides, the voltage gap between the charge and discharge curves remained almost identical in these two cells, which implied that the carbon coating on the separator did not lead to any changes of inner resistance. The discharge-charge profiles and the long-term cycling performance of the Mg-S battery with es.-POM/C as separator are shown in Figure 6.5c and Figure 6.6. Notably, after initial 15 cycles of capacity increase (from  $360 \text{ mAh g}^{-1}$  at 1<sup>st</sup> cycle to  $450 \text{ mAh g}^{-1}$  at 15<sup>th</sup> cycle), which might be ascribed to an activation process, the battery displayed a stable capacity performance of above  $400 \text{ mAh g}^{-1}$  until 50<sup>th</sup> cycle. In the following cycles, the battery showed a slight capacity decay to  $320 \text{ mAh g}^{-1}$  until 100<sup>th</sup> cycle with a capacity retention about 90%, which is much higher than the battery assembled with pristine glass fiber (67.4%) and es.-C (47.5%) respectively. In addition, except the first cycle, the coulombic efficiency of the battery with es.-POM/C remained around 95% indicating an efficient polysulfide inhibition, and hence a promoted redox chemistry of sulfur species in the as-designed MSB prototype during battery cycling.

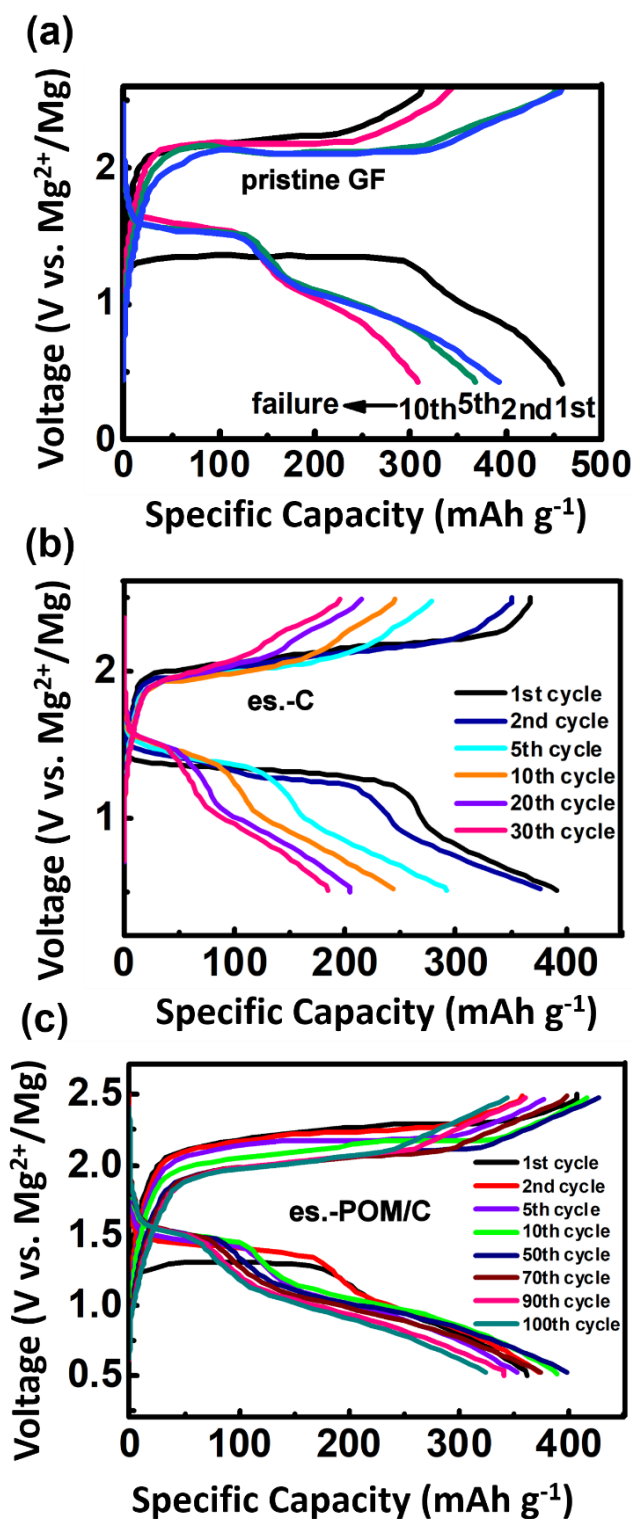


**Figure 6.5** Charge-discharge profiles of Mg-S batteries with (a) pristine Whatman glass fiber as separator, (b) electrospun-Super P carbon based glass fiber separator (abbreviated as es.-C), and (c) electrospun-POM/C based glass fiber separator (es.-POM/C).

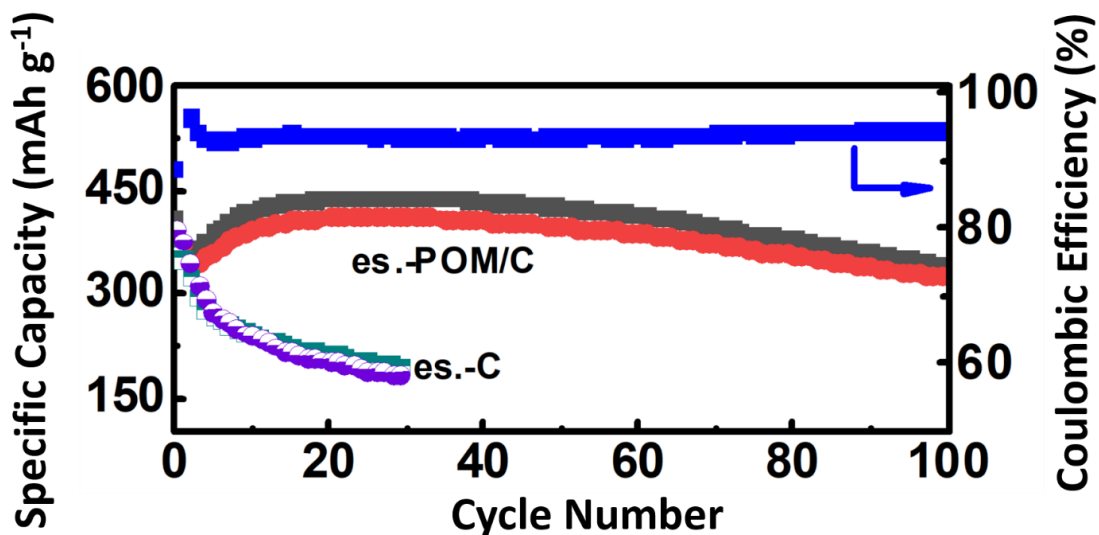


**Figure 6.6** Comparison of cycling performance of Mg-S batteries equipped with separators es.-C and es.-POM/C.

Further we explored the rate capability of the MSB with es.-POM/C as separator at current densities from 0.05C to 1C (Figure 6.7). The battery showed good reversible capacities at all C-rates with specific capacities between  $650 \text{ mAh g}^{-1}$  (at 0.05C) and  $50 \text{ mAh g}^{-1}$  (at 1C). The discharge-charge profiles at the current density of 0.05C, 0.1C and 0.2C present well-defined discharge voltage plateau at around 1.5 V and charge voltage plateau at around 2.0 V, respectively. At the current density of 0.5C and 1C, the discharge-charge profiles did not indicate clear voltage plateaus, which might be due to the sluggish kinetics of conversion reactions of magnesium polysulfide species. Moreover, it was noted that a voltage hysteresis of as-assembled MSB is about 0.65 V, which will lead to a relatively lower energy efficiency in potential applications. To investigate its origin, the CV was measured with a three-electrode cell (PAT-Cell from EL-CELL) using KB/S as working electrode (WE) and Mg foil as the counter and reference electrodes ( $\text{Mg}_{\text{CE}}$  and  $\text{Mg}_{\text{RE}}$ ), respectively. Typical CVs of the Mg-S batteries with pristine glass fiber separator and es.-POM/C for first two cycles are shown in Figure 6.8. For the battery with pristine glass fiber, during the first anodic scan, the main reduction peak of sulfur appeared at 1.20 V, and the oxidation peaked at 1.69 V in the reverse scan. In the subsequent CV cycles, both the cathodic and anodic procedures occurred at higher potentials (1.41 V and 1.73 V, respectively), which is consistent with the discharge/charge profiles with slightly increased voltages after the first cycle. The small shoulder signals in the CVs

indicate a multistep reaction in Mg-S cells. The redox signals at 1.41 and 1.73 V (*vs.* Mg<sub>RE</sub>) in the second cycle represent a voltage hysteresis of about 0.32 V between the reduction and oxidation of sulfur in the Mg-S system with pristine glass fiber. In the meanwhile, the potentials *vs.* Mg<sub>CE</sub> were recorded. As shown in Figure 6.8a, the representative CV curve for the second cycle indicates that the reduction peak for sulfur is located at a slightly lower potential of 1.35 V compared with the peak value *vs.* Mg<sub>RE</sub>. However, the oxidative signal substantially shifted up to 2.31 V (with a voltage difference of 0.58 V), implying that the recharge of the sulfur cathode was restricted by the half-reaction at the Mg<sub>CE</sub>. In contrast, the CVs of the MSB with es.-POM/C (Figure 6.8b) show that the voltage difference of oxidation peak in the second cycle (*vs.* Mg<sub>RE</sub> and *vs.* Mg<sub>CE</sub>, respectively) is about 0.27 V, which indicates a much less polarization of Mg anode and hence the improved battery cycling performance.

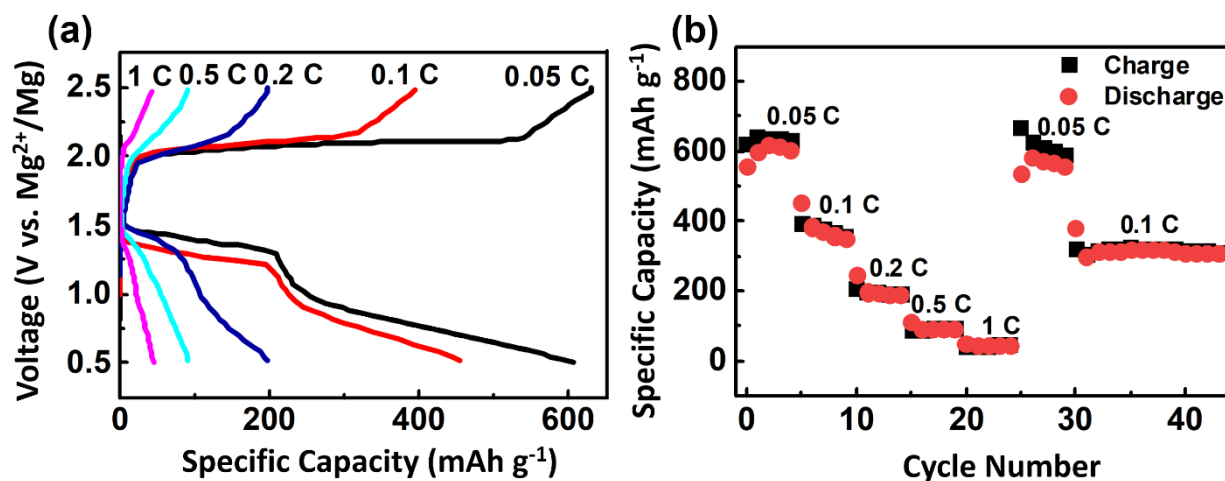


**Figure 6.7** (a) Voltage profiles of MSBs with different separators under various current densities and (b) The rate performance of MSBs with different separators;

To investigate whether the concentration of POM plays a role in influencing the battery performance, different separator coating layers with 5 wt% of POM (es.-5% POM/C) and 20 wt% of POM (es.-20% POM/C) were also fabricated by electrospinning under the same condition. The charge-discharge profiles and cycling stability of the MSBs with the as-prepared separators are shown in Figure 6.9 (es.-5% POM/C) and Figure 6.10 (es.-20% POM/C). Except for the first cycle which is determined by OCV, all the other cycles showed well-defined voltage plateaus in discharge curves (~1.5 V) and charge curves (~2.1 V). The discharge capacity shown in Figure

6.9b went through a comparatively quick drop from  $420 \text{ mAh g}^{-1}$  in 2<sup>nd</sup> cycle to  $200 \text{ mAh g}^{-1}$  in 30<sup>th</sup> cycles after an initial increase and an ongoing drop until  $100 \text{ mAh g}^{-1}$  in 100<sup>th</sup> cycle. Besides, compared with es.-POM/C, the coulombic efficiency of es.-5% POM/C was lower and less stable. In the case of es.-20% POM/C (Figure 6.10) the initial 20 cycles indicated a coulombic efficiency above 100%, which might be attributed to the “overdosed” POM that participated in the redox chemistry of sulfur species. After the 20<sup>th</sup> cycle, the coulombic efficiency went down to a value above 92%, which suggested a good reversible capacity. Except for the abnormally high coulombic efficiency in the first 20 cycles, the fluctuation of discharge and charge capacities implied an unstable chemical reactions during battery cycling. In addition, the quick capacity decay starting from 21<sup>st</sup> cycle to 100<sup>th</sup> cycle also intimated a less-competitive option by using a higher content of POM in separator coating. To sum up, the as-fabricated es.-POM/C that contained 10 wt% of POM constructed a most performance-enhanced separator coating layer, which led to excellent coulombic efficiency and cycling stability for MSBs.

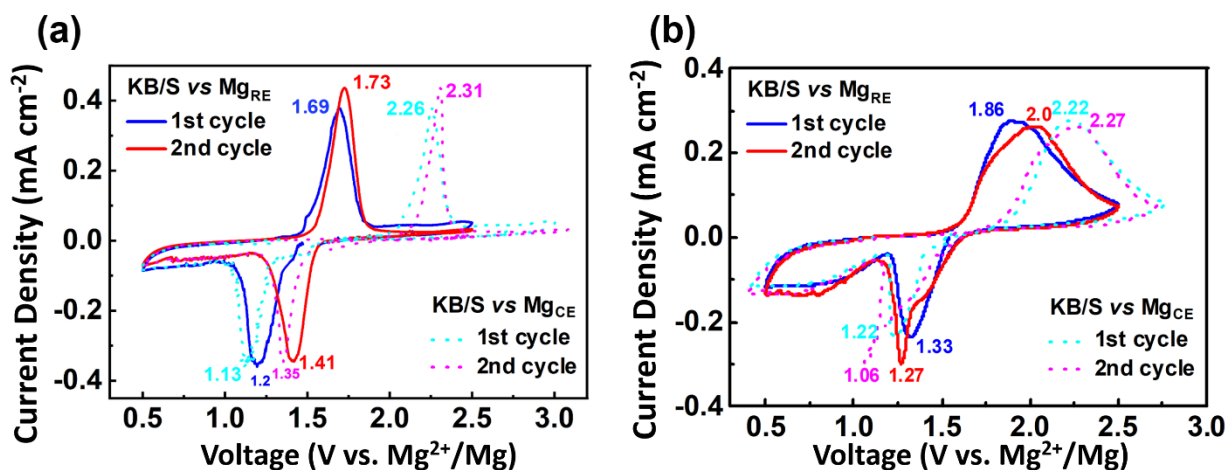


**Figure 6.8** CV curves of MSBs in a three-electrode setup at a scan rate of  $0.1 \text{ mV s}^{-1}$  (a) with pristine glass fiber as separator and (b) with es.-POM/C modified glass fiber as separator.

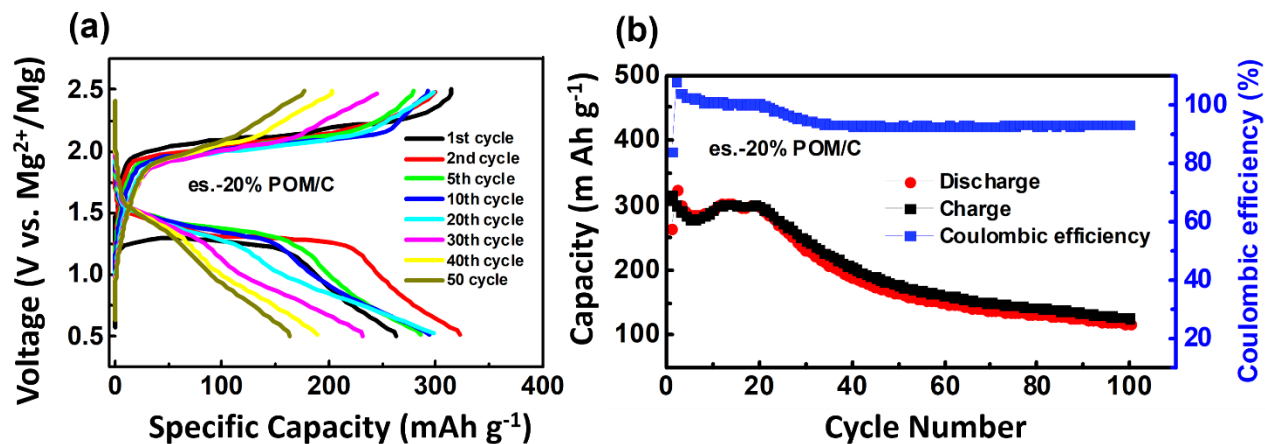


**Figure 6.9** (a) Charge-discharge profiles of Mg-S batteries with es.-5% POM/C as separator and (b) cycling stability of Mg-S batteries with es.-5% POM/C as separator.

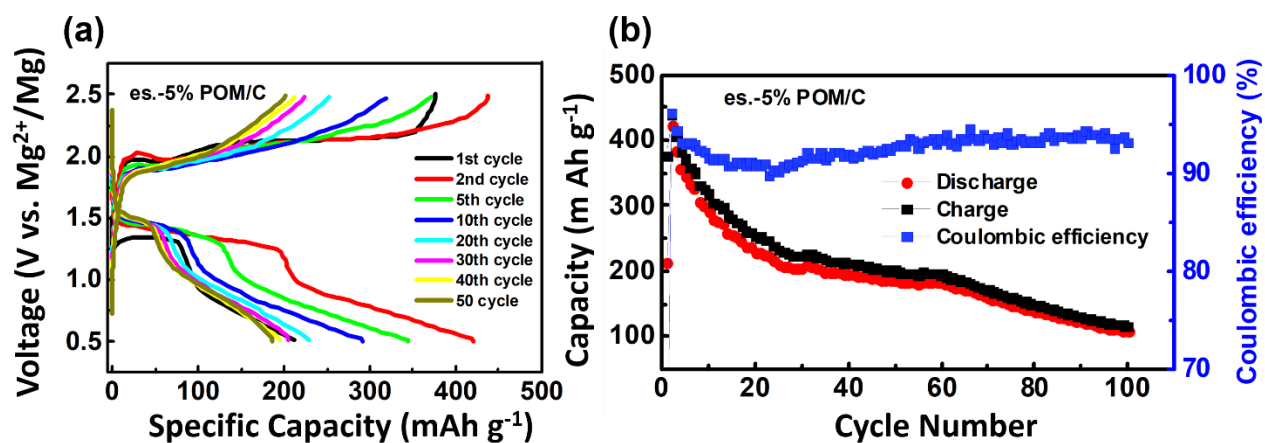


**Figure 6.10** (a) Charge-discharge profiles of Mg-S batteries with es.-20% POM/C as separator and (b) cycling stability of Mg-S batteries with es.-20% POM/C as separator.

### 6.2.3 *Ex situ* studies

To further substantiate the “polysulfide-phobic” mechanism, XPS was implemented in our study. The XPS spectra of  $\text{MgS}_n$  powder, pristine es.-POM/C and es.-POM/C immersed in  $\text{MgS}_n$  solution with tetraglyme as solvent are shown in Figure 6.11. Before XPS analysis the latter sample was washed with tetraglyme in order to remove excess of  $\text{MgS}_n$  powder. All the samples were dried before measurements. S 2p spectra have been fitted with  $2p_{3/2}$ - $2p_{1/2}$  doublets separated by 1.2 eV

with 2/1 intensity ratio due to spin-orbit coupling. The as-synthesized  $\text{MgS}_n$  exhibited three characteristic S 2p spin-orbit-splitting doublets (Figure 6.11a). Those are terminal sulfur S1 (drawn in blue, indicating  $\text{MgS}$ , polysulfides) with binding energy at 161.1 and 162.4 eV, bridging sulfur S2 (drawn in red, indicating polysulfides and elemental S) with binding energy at 164.0 and 165.1 eV, as well as S3 (drawn in pink, indicating  $\text{SO}_x$  species), which may come from oxidation of surface sulfur during sample preparation.<sup>165,166</sup> As shown in Figure 6.11a, after immersion in  $\text{MgS}_n$  solution, all the S species were recognized accordingly. Specifically, the terminal S with the S 2p<sub>3/2</sub> and S 2p<sub>1/2</sub> peaks shifted from 164.0 and 165.2 eV to 162.4 eV and 163.7 eV, respectively. However, the bridging S with the S 2p<sub>3/2</sub> and S 2p<sub>1/2</sub> peaks is located constantly at 164.0 and 165.1 eV with almost no shifting. These results suggested that the adsorption of Magnesium polysulfides by es.-POM/C was successful and the shifting in binding energy indicated an interaction between

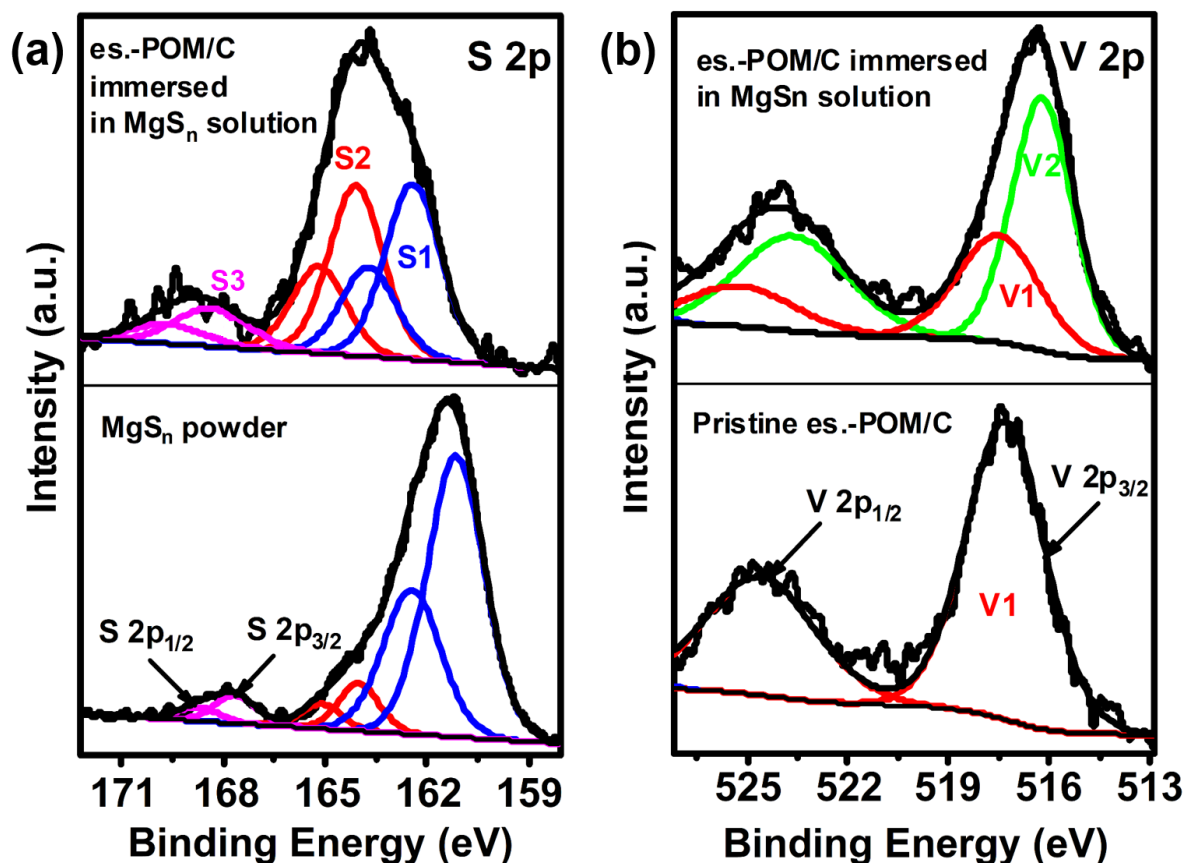


**Figure 6.11** High-resolution XPS analysis. S 2p spectra of (a) the as-synthesized  $\text{MgS}_n$  powder (bottom) and es.-POM/C separator immersed in  $\text{MgS}_n$  solution (top); V 2p spectra of (b) as-fabricated es.-POM/C separator (bottom) and es.-POM/C separator immersed in  $\text{MgS}_n$  solution (top).

POM and polysulfides.<sup>117,167,168</sup> Next, as shown in Figure 6.11b, V 2p spectrum of as-fabricated es.-POM/C displayed characteristic V 2p<sub>3/2</sub> and V 2p<sub>1/2</sub> peaks at 517.3 and 524.7 eV respectively, which were ascribed to V<sup>5+</sup>, the highest oxidation state of vanadium in POM shown in Figure 6.12. However, after immersion in MgS<sub>n</sub> solution two new V 2p peaks appeared at 516.2 and 523.8 eV respectively, which stemmed from the reduction of V<sup>5+</sup> to V<sup>4+</sup>.<sup>169,170</sup> To rule out the influence of solvent in this valence changing, es.-POM/C was soaked in the pure tetraglyme solvent for a same duration as in abovementioned immersion experiments. As shown in Figure 6.12, the XPS V 2p spectrum showed only signals of V<sup>5+</sup>. This above results further implied an intramolecular interaction between polysulfide species and POM clusters. Aligned with the enhanced battery cycling stability, the notorious polysulfide “shuttle effect” was efficiently suppressed due to the “bonded layer” of polysulfide species through intermolecular V-S<sub>n</sub><sup>2-</sup> interaction, which functioned as shields in blocking the further released polysulfides.

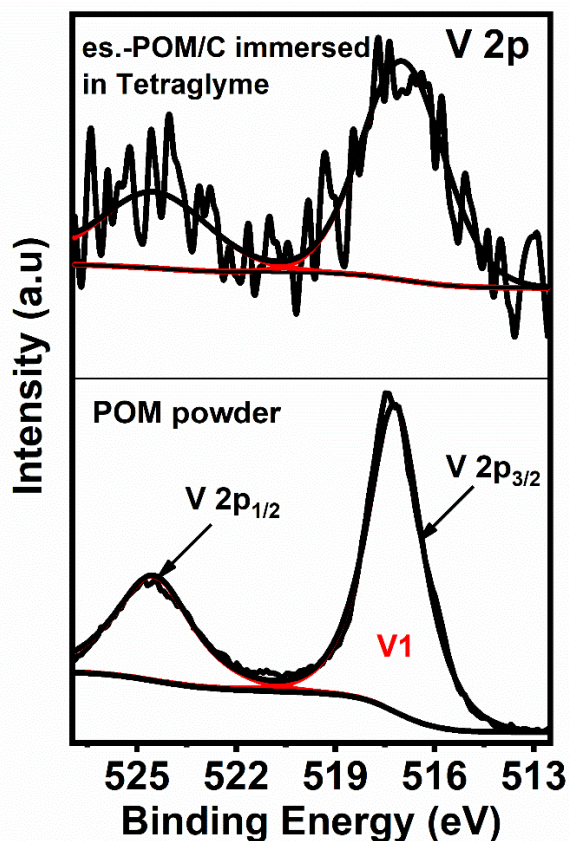


**Figure 6.12** V 2p elemental XPS spectrum of pristine POM powder (bottom) and es.-POM/C immersed in tetraglyme solvent (top).

### 6.3 Summary

In summary, we have developed an electrospinning-assisted separator coating strategy by using redox active polyoxometalate clusters and cost-effective conductive carbon material. For the first time a “neat” MSB configuration (Ketjen black/S as cathode, non-Cl<sup>-</sup> and non-additive containing electrolyte, Mg foil as anode as well as functional separator) delivered a reversible discharge capacity of around 320 mAh g<sup>-1</sup> in the 100th cycle with a coulombic efficiency higher than 95%. Furthermore, cyclic voltammetry, XPS *etc.* have revealed a polysulfides repulsion mechanism contributed by intramolecular V-S<sub>n</sub><sup>2-</sup> bond built up a shielding layer against bulk long-chain sulfur species. Due to the synergistic effect of conductive carbon and POM clusters, highly efficient reutilization of polysulfide species was achieved leading to the superb discharge capacity, high coulombic efficiency as well as excellent cycling stability. This rational Mg-S setup with electrospun functionalized separator strategy not only provided a guideline for future design of Metal-Sulfur battery systems, but also made a leap towards practical applications.

## 7 Conclusions and outlook

With the development of post-LIBs due to their high abundance and low cost, new materials and new chemistries started to show potentials in bringing the next leap in energy storage system. The applications of nanomaterials and functionality such as conductive coating of active materials have been widely investigated in rechargeable batteries. Electrospinning, as an easy, controllable and scalable method to fabricate nanostructures such as nanofibers and nanoparticles, has been often utilized in the study of post-LIBs. In this work, electrospinning was applied in three different aspects in post-LIBs: anode material for SIBs, cathode material for SIBs, and modified separator for Mg-S batteries. Self-standing electrode materials with the concept of binder-free and collector-free systems were successfully prepared. Electrospun coating on glass fiber separators was proved to effectively inhibit shuttle effect of polysulfides for Mg-S batteries.

Conclusions of each parts are summarized as following:

(i) Self-standing CNFs were used as anode material for SIBs. The mechanism of CNFs with different structures can be divided into two categories when it comes to the interaction with  $\text{Na}^+$  ions: intercalation (diffusion-controlled) and surface capacitive effects. The electrospun CNFs contain disordered structures with an increasing content of graphitic domains and decreasing amount of heteroatoms with the increasing carbonized temperature. CNFs carbonized at 600 °C and 800 °C showed a capacitance contribution while CNFs carbonized at 1000 °C exhibited mainly an intercalation behavior of  $\text{Na}^+$  ions along with capacitive contribution. A high irreversible capacity in the initial cycle from SEI formation and a fast capacity decay limited the self-standing CNFs to be applied in real-life practice. However, this study of the mechanism of CNFs as anode material for SIBs inspired a careful look into similar materials, especially nanostructures, with high surface area when applied in post-LIBs.

(ii) Maricite  $\text{NaFePO}_4/\text{CNF}$  composite was studied as self-standing cathode material for SIBs. Within the CNF network, the originally inactive maricite  $\text{NaFePO}_4$  showed a gradual involvement in electrochemical behavior upon cycles. Compared to a traditional slurry cathode with a capacity around 20 mAh  $\text{g}^{-1}$ , this self-standing electrode showed a much higher reversible capacity up to 108 mAh  $\text{g}^{-1}$  after initial increase. The strongly interacting nanofibers were proposed to facilitate the diffusion of  $\text{Na}^+$  ions and electronic conductivity of the active materials. Nevertheless, the

capacitive contributions originating from the high surface area were also studied, amounting up to 60% of the whole current contributions at  $1 \text{ mV s}^{-1}$ . This electrospun hybrid electrode offered some new aspects of improving the performance of active materials with poor electrical conductivity.

(iii) A coated separator for Mg-S batteries was prepared with the help of electrospinning. The functional coating was prepared by electrospinning a mixture of decavanadate clusters and Super P carbon on a commercial glass fiber separator, aiming to serve as a “polysulfide-phobic” layer. MSBs showed a capacity around  $350 \text{ mAh g}^{-1}$  for over 100 cycles with capacity retention of 90% with the functionalized separator, compared to a fast deteriorate performance of the ones using pristine separators. XPS measurement indicated an intramolecular interaction between polysulfide species and decavanadate clusters. The front-bonded layer of polysulfides was proposed to act as a shielding layer that inhibited the further shuttling of polysulfide species. This achievement has shown great potentials of electrospinning applied in metal sulfur batteries, and also in enhancement of other inactive components for a rechargeable battery.

It is positive to see that the method has brought some new opportunities into electrode preparation, material improvement and functionality of passive components. In recent years, a new concept was brought out as *supercapattery* where a combined mechanism of diffusion and capacitor was brought out.<sup>171</sup> With diverse nanostructures introduced in the rechargeable battery research, great care needs to be taken considering the high surface area which may cause more side reactions. And the surface charge effect from nanomaterials should not be neglected. Moreover, it is hard to deny that electrospinning is a time consuming method with limited product efficiency, where the development of a continuous producing system for industrial applications is highly demanded.<sup>172,173</sup>

## 8 References

- 1 Hubbert, M. K. Energy from Fossil Fuels. *Science*, 109 (2823): 103–109, 1949.
- 2 Yoda, S., Ishihara, K. Global Energy Prospects in the 21st Century: A Battery-Based Society. *J. Power Sources*, 68 (1): 3–7, 1997.
- 3 Larcher, D., Tarascon, J. M. Towards Greener and More Sustainable Batteries for Electrical Energy Storage. *Nat. Chem.*, 7 (1): 19–29, 2015.
- 4 Momirlan, M., Veziroglu, T. N. The Properties of Hydrogen as Fuel Tomorrow in Sustainable Energy System for a Cleaner Planet. *Int. J. Hydrogen Energy*, 30 (7): 795–802, 2005.
- 5 Panwar, N. L., Kaushik, S. C., Kothari, S. Role of Renewable Energy Sources in Environmental Protection: A Review. *Renew. Sustain. Energy Rev.*, 15 (3): 1513–1524, 2011.
- 6 Liming, H. Financing Rural Renewable Energy: A Comparison between China and India. *Renew. Sustain. Energy Rev.*, 13 (5): 1096–1103, 2009.
- 7 Hwang, J. Y., Myung, S. T., Sun, Y. K. Sodium-Ion Batteries: Present and Future. *Chem. Soc. Rev.*, 46 (12): 3529–3614, 2017.
- 8 Ould Amrouche, S., Rekioua, D., Rekioua, T., Bacha, S. Overview of Energy Storage in Renewable Energy Systems. *Int. J. Hydrogen Energy*, 41 (45): 20914–20927, 2016.
- 9 Dunn, B., Kamath, H., Tarascon, J. M. Electrical Energy Storage for the Grid: A Battery of Choices. *Science*, 334 (6058): 928–935, 2011.
- 10 Van Schalkwijk, W., Scrosati, B. Introduction. *Advances in Lithium-Ion Batteries*. Springer US: Boston, 2002.
- 11 Goodenough, J. B. General Concepts. *Lithium Ion Batteries: Fundamentals and Performance*. Kodansha, Ltd: Tokyo, 1998.
- 12 Park J. K. Introduction. *Principles and Applications of Lithium Secondary Batteries*. John Wiley & Sons, Ltd: Weinheim, 2012.
- 13 Deimede, V., Elmasides, C. Separators for Lithium-Ion Batteries: A Review on the Production Processes and Recent Developments. *Energy Technol.*, 3 (5): 453–468, 2015.
- 14 Yamada, M., Watanabe, T., Gunji, T., Wu, J., Matsumoto, F. Review of the Design of Current Collectors for Improving the Battery Performance in Lithium-Ion and Post-Lithium-Ion Batteries. *Electrochem.*, 1 (2): 124–159, 2020.

- 15 Kraytsberg, A., Ein-Eli, Y. Higher, Stronger, Better ... A Review of 5 Volt Cathode Materials for Advanced Lithium-Ion Batteries. *Adv. Energy Mater.*, 2 (8): 922–939, 2012.
- 16 Manthiram, A. Materials Aspects: An Overview. *Lithium Batteries: Science and Technology*. Springer US: Boston, 2003.
- 17 Middlemiss, L., Holland, A Review of Post-Lithium-Ion Batteries Lithium-Ion. A., *Applications, I.*, 1–15, 2018.
- 18 Sawicki, M., Shaw, L. L. Advances and Challenges of Sodium Ion Batteries as Post Lithium Ion Batteries. *RSC Adv.*, 5 (65): 53129–53154, 2015.
- 19 Choi, J. W., Aurbach, D. Promise and Reality of Post-Lithium-Ion Batteries with High Energy Densities. *Nat. Rev. Mater.*, 1 (4): 16013, 2016.
- 20 Kim, H., Kim, J. C., Bianchini, M., Seo, D. H., Rodriguez-Garcia, J., Ceder, G. Recent Progress and Perspective in Electrode Materials for K-Ion Batteries. *Adv. Energy Mater.*, 8 (9): 1–19, 2018.
- 21 Zhang, Z., Zhao, M., Xia, M., Qi, R., Liu, M., Nie, J., Wang, Z. L., Lu, X. Magnesium Anodes with Extended Cycling Stability for Lithium-Ion Batteries. *Adv. Funct. Mater.*, 29 (41): 1–9, 2019.
- 22 Aurbach, D., Suresh, G. S., Levi, E., Mitelman, A., Mizrahi, O., Chusid, O., Brunelli, M. Progress in Rechargeable Magnesium Battery Technology. *Adv. Mater.*, 19 (23): 4260–4267, 2007.
- 23 Yoo, H. D., Shterenberg, I., Gofer, Y., Gershinshy, G., Pour, N., Aurbach, D. Mg Rechargeable Batteries: An on-Going Challenge. *Energy Environ. Sci.*, 6 (8): 2265–2279, 2013.
- 24 Palmer, N.J. Secondary Metal/Air Cell. United States Patent : 3,650,837, 1972.
- 25 Shao, Y., Ding, F., Xiao, J., Zhang, J., Xu, W., Park, S., Zhang, J.-G., Wang, Y., Liu, J. Making Li-Air Batteries Rechargeable: Material Challenges. *Adv. Funct. Mater.*, 23 (8): 987–1004, 2013.
- 26 Park, J., Lee, J., Alfaruqi, M. H., Kwak, W. J., Kim, J., Hwang, J. Y. Initial Investigation and Evaluation of Potassium Metal as an Anode for Rechargeable Potassium Batteries. *J. Mater. Chem. A*, 8 (33): 16718–16737, 2020.
- 27 Yabuuchi, N., Kubota, K., Dahbi, M., Komaba, S. Research Development on Sodium-Ion Batteries. *Chem. Rev.*, 114 (23): 11636–11682, 2014.

- 
- 28 Vaalma, C., Buchholz, D., Weil, M., Passerini, S. A Cost and Resource Analysis of Sodium-Ion Batteries. *Nat. Rev. Mater.*, 3 (4): 18013, 2018.
- 29 Murray, J. L. The Al–Na (Aluminum-Sodium) System. *Bull. Alloy Phase Diagrams*, 4 (4): 407–410, 1983.
- 30 Zhao, Y., Adair, K. R., Sun, X. Recent Developments and Insights into the Understanding of Na Metal Anodes for Na-Metal Batteries. *Energy Environ. Sci.*, 11 (10): 2673–2695, 2018.
- 31 Dou, X., Hasa, I., Saurel, D., Vaalma, C., Wu, L., Buchholz, D., Bresser, D., Komaba, S., Passerini, S. Hard Carbons for Sodium-Ion Batteries: Structure, Analysis, Sustainability, and Electrochemistry. *Mater. Today*, 2387–104, 2019.
- 32 Moriwake, H. Why Is Sodium-Intercalated Graphite Unstable? *RSC Adv.*, 736550–36554, 2017.
- 33 Li, Z., Jian, Z., Wang, X., Rodríguez-Pérez, I. A., Bommier, C., Ji, X. Hard Carbon Anodes of Sodium-Ion Batteries: Undervalued Rate Capability. *Chem. Commun.*, 53 (17): 2610–2613, 2017.
- 34 Stevens, D. A., Dahn, J. R. High Capacity Anode Materials for Rechargeable Sodium-Ion Batteries. 147 (4): 1271–1273, 2000.
- 35 Irisarri, E., Ponrouch, a., Palacin, M. R. Review—Hard Carbon Negative Electrode Materials for Sodium-Ion Batteries. *J. Electrochem. Soc.*, 162 (14): A2476–A2482, 2015.
- 36 Wang, H. G., Yuan, S., Ma, D. L., Zhang, X. B., Yan, J. M. Electrospun Materials for Lithium and Sodium Rechargeable Batteries: From Structure Evolution to Electrochemical Performance. *Energy Environ. Sci.*, 8 (6): 1660–1681, 2015.
- 37 Kim, J., Seo, D. H., Kim, H., Park, I., Yoo, J. K., Jung, S. K., Park, Y. U., Goddard III, W. A., Kang, K. Unexpected Discovery of Low-Cost Maricite NaFePO<sub>4</sub> as a High-Performance Electrode for Na-Ion Batteries. *Energy Environ. Sci.*, 8 (2): 540–545, 2015.
- 38 Xu, G. L., Amine, R., Abouimrane, A., Che, H., Dahbi, M., Ma, Z. F., Saadoun, I., Alami, J., Mattis, W. L., Pan, F., Chen, Z., Amine, K. Challenges in Developing Electrodes, Electrolytes, and Diagnostics Tools to Understand and Advance Sodium-Ion Batteries. *Adv. Energy Mater.*, 8 (14): 1–63, 2018.
- 39 Yamada, Y., Doi, T., Tanaka, I., Okada, S., Yamaki, J. I. Liquid-Phase Synthesis of Highly Dispersed NaFeF<sub>3</sub> Particles and Their Electrochemical Properties for Sodium-Ion Batteries. *J. Power Sources*, 196 (10): 4837–4841, 2011.

- 40 Jian, Z., Han, W., Lu, X., Yang, H., Hu, Y. S., Zhou, J., Zhou, Z., Li, J., Chen, W., Chen, D., Chen, L. Superior Electrochemical Performance and Storage Mechanism of  $\text{Na}_3\text{V}_2(\text{PO}_4)_3$  Cathode for Room-Temperature Sodium-Ion Batteries. *Adv. Energy Mater.*, 3 (2): 156–160, 2013.
- 41 Xiong, F., An, Q., Xia, L., Zhao, Y., Mai, L., Tao, H., Yue, Y. Revealing the Atomistic Origin of the Disorder-Enhanced Na-Storage Performance in  $\text{NaFePO}_4$  Battery Cathode. *Nano Energy*, 57608–615, 2019.
- 42 Tepavcevic, S., Xiong, H., Stamenkovic, V. R., Zuo, X., Balasubramanian, M., Prakapenka, V. B., Johnson, C. S., Rajh, T. Nanostructured Bilayered Vanadium Oxide Electrodes for Rechargeable Sodium-Ion Batteries. *ACS Nano*, 6 (1): 530–538, 2012.
- 43 Rai, A. K., Anh, L. T., Gim, J., Mathew, V., Kim, J. Electrochemical Properties of  $\text{Na}_x\text{CoO}_2$  ( $x \sim 0.4$ ) Cathode for Rechargeable Sodium-Ion Batteries. *Ceram. Int.*, 40 (1 PART B): 2411–2417, 2014.
- 44 Vassilaras, P., Toumar, A. J., Ceder, G. Electrochemical Properties of  $\text{NaNi}_{1/3}\text{Co}_{1/3}\text{Fe}_{1/3}\text{O}_2$  as a Cathode Material for Na-Ion Batteries. *Electrochem. commun.*, 3879–81, 2014.
- 45 Fu, B., Zhou, X., Wang, Y. High-Rate Performance Electrospun  $\text{Na}_{0.44}\text{MnO}_2$  Nanofibers as Cathode Material for Sodium-Ion Batteries. *J. Power Sources*, 310102–108, 2016.
- 46 Fang, Y., Liu, Q., Xiao, L., Ai, X., Yang, H., Cao, Y. High-Performance Olivine  $\text{NaFePO}_4$  Microsphere Cathode Synthesized by Aqueous Electrochemical Displacement Method for Sodium Ion Batteries. *ACS Appl. Mater. Interfaces*, 7 (32): 17977–17984, 2015.
- 47 Oh, S. M., Myung, S. T., Hassoun, J., Scrosati, B., Sun, Y. K. Reversible  $\text{NaFePO}_4$  Electrode for Sodium Secondary Batteries. *Electrochem. commun.*, 22 (1): 149–152, 2012.
- 48 Burba, C. M., Frech, R. Vibrational Spectroscopic Investigation of Structurally-Related  $\text{LiFePO}_4$ ,  $\text{NaFePO}_4$ , and  $\text{FePO}_4$  Compounds. *Spectrochim. Acta - Part A Mol. Biomol. Spectrosc.*, 65 (1): 44–50, 2006.
- 49 Casas-Cabanas, M., Roddatis, V. V., Saurel, D., Kubiak, P., Carretero-González, J., Palomares, V., Serras, P., Rojo, T. Crystal Chemistry of Na Insertion/deinsertion in  $\text{FePO}_4$ - $\text{NaFePO}_4$ . *J. Mater. Chem.*, 22 (34): 17421–17423, 2012.
- 50 Lepage, Y., Donnay, G. The Crystal Structure of the New Mineral Maricite,  $\text{NaFePO}_4$ . *Can. Mineral.*, 15 (4): 518–521, 1977.
- 51 Li, J., Ma, Z. F. Past and Present of  $\text{LiFePO}_4$ : From Fundamental Research to Industrial Applications. *Chem*, 5 (1): 3–6, 2019.

- 
- 52 Rahman, M. M., Sultana, I., Mateti, S., Liu, J., Sharma, N., Chen, Y. Maricite NaFePO<sub>4</sub>/C/graphene: A Novel Hybrid Cathode for Sodium-Ion Batteries. *J. Mater. Chem. A*, 5 (32): 16616–16621, 2017.
- 53 Liu, Y., Zhang, N., Wang, F., Liu, X., Jiao, L., Fan, L. Z. Approaching the Downsizing Limit of Maricite NaFePO<sub>4</sub> Toward High-Performance Cathode for Sodium-Ion Batteries. *Adv. Funct. Mater.*, 28 (30): 1–9, 2018.
- 54 Xie, J., Li, C., Cui, Z., Guo, X. Transition-Metal-Free Magnesium-Based Batteries Activated by Anionic Insertion into Fluorinated Graphene Nanosheets. *Adv. Funct. Mater.*, 25 (41): 6519–6526, 2015.
- 55 Arthur, T. S., Zhang, R., Ling, C., Glans, P. A., Fan, X., Guo, J., Mizuno, F. Understanding the Electrochemical Mechanism of K- $\alpha$ MnO<sub>2</sub> for Magnesium Battery Cathodes. *ACS Appl. Mater. Interfaces*, 6 (10): 7004–7008, 2014.
- 56 Bonnick, P., Blanc, L., Vajargah, S. H., Lee, C. W., Sun, X., Balasubramanian, M., Nazar, L. F. Insights into Mg<sup>2+</sup> Intercalation in a Zero-Strain Material: Thiospinel Mg<sub>x</sub>Zr<sub>2</sub>S<sub>4</sub>. *Chem. Mater.*, 30 (14): 4683–4693, 2018.
- 57 Salama, M., Sharma, R., Attias, R., Yemini, R., Gofer, Y., Aurbach, D., Noked, M. Metal-Sulfur Batteries-Overview and Research Methods. *ACS Energy Lett.*, 4 (2): 436–446, 2019.
- 58 Wang, P., Buchmeiser, M. R. Rechargeable Magnesium–Sulfur Battery Technology: State of the Art and Key Challenges. *Adv. Funct. Mater.*, 29 (49): 1905248, 2019.
- 59 Zhao-Karger, Z., Fichtner, M. Magnesium-Sulfur Battery: Its Beginning and Recent Progress. *MRS Commun.*, 7 (4): 770–784, 2017.
- 60 Gao, T., Hou, S., Huynh, K., Wang, F., Eidson, N., Fan, X., Han, F., Luo, C., Mao, M., Li, X., Wang, C. Existence of Solid Electrolyte Interphase in Mg Batteries: Mg/S Chemistry as an Example. *ACS Appl. Mater. Interfaces*, 10 (17): 14767–14776, 2018.
- 61 Gao, T., Hou, S., Huynh, K., Wang, F., Eidson, N., Fan, X., Han, F., Luo, C., Mao, M., Li, X., Wang, C. Existence of Solid Electrolyte Interphase in Mg Batteries: Mg/S Chemistry as an Example. *ACS Appl. Mater. Interfaces*, 10 (17): 14767–14776, 2018.
- 62 Drvarič Talian, S., Kapun, G., Moškon, J., Vizintin, A., Randon-Vitanova, A., Dominko, R., Gaberšček, M. Which Process Limits the Operation of a Li-S System? *Chem. Mater.*, 31: 9012–9023, 2019.

- 63 Zhou, X., Tian, J., Hu, J., Li, C. High Rate Magnesium–Sulfur Battery with Improved Cyclability Based on Metal–Organic Framework Derivative Carbon Host. *Adv. Mater.*, 30 (7): 1–8, 2018.
- 64 Wang, W., Yuan, H., Nuli, Y., Zhou, J., Yang, J., Wang, J. Sulfur@microporous Carbon Cathode with a High Sulfur Content for Magnesium-Sulfur Batteries with Nucleophilic Electrolytes. *J. Phys. Chem. C*, 12226764–26776, 2018.
- 65 Zhao-Karger, Z., Zhao, X., Wang, D., Diemant, T., Behm, R. J., Fichtner, M. Performance Improvement of Magnesium Sulfur Batteries with Modified Non-Nucleophilic Electrolytes. *Adv. Energy Mater.*, 5 (3): 1401155, 2015.
- 66 Zhao-Karger, Z., Zhao, X., Wang, D., Diemant, T., Behm, R. J., Fichtner, M. Performance Improvement of Magnesium Sulfur Batteries with Modified Non-Nucleophilic Electrolytes. *Adv. Energy Mater.*, 5 (3): 2015.
- 67 Fan, H., Zheng, Z., Zhao, L., Li, W., Wang, J., Dai, M., Zhao, Y., Xiao, J., Wang, G., Ding, X., Xiao, H., Li, J., Wu, Y., Zhang, Y. Extending Cycle Life of Mg/S Battery by Activation of Mg Anode/Electrolyte Interface through an LiCl-Assisted MgCl<sub>2</sub> Solubilization Mechanism. *Adv. Funct. Mater.*, 30 (9): 1909370, 2020.
- 68 Attias, R., Salama, M., Hirsch, B., Goffer, Y., Aurbach, D. Anode-Electrolyte Interfaces in Secondary Magnesium Batteries. *Joule*, 3 (1): 27–52, 2019.
- 69 Yu, X., Manthiram, A. Performance Enhancement and Mechanistic Studies of Magnesium-Sulfur Cells with an Advanced Cathode Structure. *ACS Energy Lett.*, 1 (2): 431–437, 2016.
- 70 Xu, Y., Ye, Y., Zhao, S., Feng, J., Li, J., Chen, H., Yang, A., Shi, F., Jia, L., Wu, Y., Yu, X., Glans-Suzuki, P. A., Cui, Y., Guo, J., Zhang, Y. In Situ X-Ray Absorption Spectroscopic Investigation of the Capacity Degradation Mechanism in Mg/S Batteries. *Nano Lett.*, 19 (5): 2928–2934, 2019.
- 71 Peng, S., Ilango, P. R. Electrospinning Technology. *Electrospinning of Nanofibers for Battery Applications*. Springer Singapore: Singapore, 2020.
- 72 Xue, J., Wu, T., Dai, Y., Xia, Y. Electrospinning and Electrospun Nanofibers: Methods, Materials, and Applications. *Chem. Rev.*, 119 (8): 5298–5415, 2019.
- 73 Teo, W. E., Ramakrishna, S. A Review on Electrospinning Design and Nanofibre Assemblies. *Nanotechnology*, 17 (14): R89-R106, 2006.

- 
- 74 Baji, A., Mai, Y. W., Wong, S. C., Abtahi, M., Chen, P. Electrospinning of Polymer Nanofibers: Effects on Oriented Morphology, Structures and Tensile Properties. *Compos. Sci. Technol.*, 70 (5): 703–718, 2010.
- 75 Sun, G., Sun, L., Xie, H., Liu, J. Electrospinning of Nanofibers for Energy Applications. *Nanomater. (Basel, Switzerland)*, 6 (7): 129, 2016.
- 76 Zhang, B., Yu, Y., Xu, Z. L., Abouali, S., Akbari, M., He, Y. B., Kang, F., Kim, J. K. Correlation Between Atomic Structure and Electrochemical Performance of Anodes Made from Electrospun Carbon Nanofiber Films. *Adv. Energy Mater.*, 4 (7): 1301448, 2014.
- 77 Li, D., Wang, Y., Xia, Y. Electrospinning of Polymeric and Ceramic Nanofibers as Uniaxially Aligned Arrays. *Nano Lett.*, 3 (8): 1167–1171, 2003.
- 78 Park, S. H., Kim, B. K., Lee, W. J. Electrospun activated carbon nanofibers with hollow core/highly mesoporous shell structure as counter electrodes for dye-sensitized solar cells. *J. Power Sources*, 239: 122–127, 2013.
- 79 Cakici, M., Reddy, K. R., Alonso-Marroquin, F. Advanced Electrochemical Energy Storage Supercapacitors Based on the Flexible Carbon Fiber Fabric-Coated with Uniform Coral-like MnO<sub>2</sub> Structured Electrodes. *Chem. Eng. J.*, 309: 151–158, 2017.
- 80 Zhang, L., Aboagye, A., Kelkar, A., Lai, C., Fong, H. A Review: Carbon Nanofibers from Electrospun Polyacrylonitrile and Their Applications. *J. Mater. Sci.*, 49 (2): 463–480, 2014.
- 81 Serp, P., Corrias, M., Kalck, P. Carbon Nanotubes and Nanofibers in Catalysis. *Appl. Catal. A Gen.*, 253 (2): 337–358, 2003.
- 82 De Jong, K. P., Geus, J. W. Carbon Nanofibers: Catalytic Synthesis and Applications. *Catal. Rev. - Sci. Eng.*, 42 (4): 481–510, 2000.
- 83 Feng, L., Xie, N., Zhong, J. Carbon Nanofibers and Their Composites: A Review of Synthesizing, Properties and Applications. *Materials (Basel)*, 7 (5): 3919–3945, 2014.
- 84 Zhang, X., Ji, L., Toprakci, O., Liang, Y., Alcoutlabi, M. Electrospun Nanofiber-Based Anodes, Cathodes, and Separators for Advanced Lithium-Ion Batteries. *Polym. Rev.*, 51 (3): 239–264, 2011.
- 85 Liu, J., Yue, Z., Fong, H. Continuous Nanoscale Carbon Fibers with Superior Mechanical Strength. *Small*, 5 (5): 536–542, 2009.
- 86 Li, W., Li, M., Adair, K. R., Sun, X., Yu, Y. Carbon Nanofiber-Based Nanostructures for Lithium-Ion and Sodium-Ion Batteries. *J. Mater. Chem. A*, 5 (27): 13882–13906, 2017.

- 87 Zhu, Y., Han, X., Xu, Y., Liu, Y., Zheng, S., Xu, K., Hu, L., Wang, C. Electrospun Sb/C Fibers for a Stable and Fast Sodium-Ion Battery Anode. *ACS Nano*, 7 (7): 6378–6386, 2013.
- 88 Liu, J., Tang, K., Song, K., Van Aken, P. a., Yu, Y., Maier, J. Electrospun Na<sub>3</sub>V<sub>2</sub>(PO<sub>4</sub>)<sub>3</sub>/C Nanofibers as Stable Cathode Materials for Sodium-Ion Batteries. *Nanoscale*, 6 (10): 5081–5086, 2014.
- 89 Xiong, Y., Qian, J., Cao, Y., Ai, X., Yang, H. Electrospun TiO<sub>2</sub>/C Nanofibers As a High-Capacity and Cycle-Stable Anode for Sodium-Ion Batteries. *ACS Appl. Mater. Interfaces*, 8 (26): 16684–16689, 2016.
- 90 Peng, S., Ilango, P. R. Electrospinning of Nanofibers for Na-Ion Battery. *Electrospinning of Nanofibers for Battery Applications*. Springer Singapore: Singapore, 2020.
- 91 Choi, N. S., Ha, S. Y., Lee, Y., Jang, J. Y., Jeong, M. H., Shin, W. C., Ue, M. Recent Progress on Polymeric Binders for Silicon Anodes in Lithium-Ion Batteries. *J. Electrochem. Sci. Technol.*, 6 (2): 35–49, 2015.
- 92 Chou, S. L., Pan, Y., Wang, J. Z., Liu, H. K., Dou, S. X. Small Things Make a Big Difference: Binder Effects on the Performance of Li and Na Batteries. *Phys. Chem. Chem. Phys.*, 16 (38): 20347–20359, 2014.
- 93 Bai, Y., Wang, Z., Wu, C., Xu, R., Wu, F., Liu, Y., Li, H., Li, Y., Lu, J., Amine, K. Hard Carbon Originated from Polyvinyl Chloride Nanofibers As High-Performance Anode Material for Na-Ion Battery. *ACS Appl. Mater. Interfaces*, 7 (9): 5598–5604, 2015.
- 94 Chen, C., Lu, Y., Ge, Y., Zhu, J., Jiang, H., Li, Y., Hu, Y., Zhang, X. Synthesis of Nitrogen-Doped Electrospun Carbon Nanofibers as Anode Material for High-Performance Sodium-Ion Batteries. *Energy Technol.*, 4 (11): 1440–1449, 2016.
- 95 Liu, Y., Wang, F., Fan, L. Z. Self-Standing Na-Storage Anode of Fe<sub>2</sub>O<sub>3</sub> Nanodots Encapsulated in Porous N-Doped Carbon Nanofibers with Ultra-High Cyclic Stability. *Nano Res.*, 11 (8): 4026–4037, 2018.
- 96 Li, W., Zeng, L., Yang, Z., Gu, L., Wang, J., Liu, X., Cheng, J., Yu, Y. Free-Standing and Binder-Free Sodium-Ion Electrodes with Ultralong Cycle Life and High Rate Performance Based on Porous Carbon Nanofibers. *Nanoscale*, 6 (2): 693–698, 2014.
- 97 Yin, H., Li, Q., Cao, M., Zhang, W., Zhao, H., Li, C., Huo, K., Zhu, M. Nanosized-Bismuth-Embedded 1D Carbon Nanofibers as High-Performance Anodes for Lithium-Ion and Sodium-Ion Batteries. *Nano Res.*, 10 (6): 2156–2167, 2017.

- 
- 98 Liu, J., Tang, K., Song, K., van Aken, P. A., Yu, Y., Maier, J. Tiny  $\text{Li}_4\text{Ti}_5\text{O}_{12}$  Nanoparticles Embedded in Carbon Nanofibers as High-Capacity and Long-Life Anode Materials for Both Li-Ion and Na-Ion Batteries. *Phys. Chem. Chem. Phys.*, 15 (48): 20813–20818, 2013.
- 99 Ge, Y., Zhu, J., Lu, Y., Chen, C., Qiu, Y., Zhang, X. The Study on Structure and Electrochemical Sodiation of One-Dimensional Nanocrystalline  $\text{TiO}_2\text{@C}$  Nanofiber Composites. *Electrochim. Acta*, 176: 989–996, 2015.
- 100 Kang, Y., Deng, C., Chen, Y., Liu, X., Liang, Z., Li, T., Hu, Q., Zhao, Y. Binder-Free Electrodes and Their Application for Li-Ion Batteries. *Nanoscale Res. Lett.*, 15 (1): 112, 2020.
- 101 Guo, J., Sun, A., Wang, C. A Porous Silicon-Carbon Anode with High Overall Capacity on Carbon Fiber Current Collector. *Electrochem. commun.*, 12 (7): 981–984, 2010.
- 102 Waluś, S., Barchasz, C., Bouchet, R., Martin, J. F., Leprêtre, J. C., Alloin, F. Non-Woven Carbon Paper as Current Collector for Li-ion/ $\text{Li}_2\text{S}$  System: Understanding of the First Charge Mechanism. *Electrochim. Acta*, 180: 178–186, 2015.
- 103 Mao, M., Cui, C., Wu, M., Zhang, M., Gao, T., Fan, X., Chen, J., Wang, T., Ma, J., Wang, C. Flexible  $\text{ReS}_2$  nanosheets/N-Doped Carbon Nanofibers-Based Paper as a Universal Anode for Alkali (Li, Na, K) Ion Battery. *Nano Energy*, 45 (3): 346–352, 2018.
- 104 Yuvaraj, S., Oh, W., Yoon, W. S. Recent Progress on Sodium Vanadium Fluorophosphates for High Voltage Sodium-Ion Battery Application. *J. Electrochem. Sci. Technol.*, 10 (1): 1–13, 2019.
- 105 Zhu, Q., Nan, B., Shi, Y., Zhu, Y., Wu, S., He, L., Deng, Y., Wang, L., Chen, Q., Lu, Z.  $\text{Na}_3\text{V}_2(\text{PO}_4)_3/\text{C}$  Nanofiber Bifunction as Anode and Cathode Materials for Sodium-Ion Batteries. *J. Solid State Electrochem.*, 21 (10): 2985–2995, 2017.
- 106 Niu, Y., Xu, M., Dai, C., Shen, B., Li, C. M. Electrospun Graphene-Wrapped  $\text{Na}_{6.24}\text{Fe}_{4.88}(\text{P}_2\text{O}_7)_4$  Nanofibers as a High-Performance Cathode for Sodium-Ion Batteries. *Phys. Chem. Chem. Phys.*, 19 (26): 17270–17277, 2017.
- 107 Luo, L., Cheng, B., Chen, Y., Chen, S., Liu, G., Zhuo, H. Electrospun  $\text{Na}_3\text{V}_2(\text{PO}_4)_3/\text{C}$  Nanofibers as Self-Standing Cathode Material for High Performance Sodium Ion Batteries. *Mater. Res. Express*, 7 (2): 025508, 2020.
- 108 Li, H., Bai, Y., Wu, F., Li, Y., Wu, C. Budding Willow Branches Shaped  $\text{Na}_3\text{V}_2(\text{PO}_4)_3/\text{C}$  Nanofibers Synthesized via an Electrospinning Technique and Used as Cathode Material for Sodium Ion Batteries. *J. Power Sources*, 273 (1): 784–792, 2015.

- 109 Bachtin, K., Kaus, M., Pfaffmann, L., Indris, S., Knapp, M., Roth, C., Ehrenberg, H. Comparison of Electrospun and Conventional LiFePO<sub>4</sub>/C Composite Cathodes for Li-Ion Batteries. *Mater. Sci. Eng. B Solid-State Mater. Adv. Technol.*, 213 (11): 98–104, 2016.
- 110 Kalluri, S., Hau Seng, K., Kong Pang, W., Guo, Z., Chen, Z., Liu, H. K., Dou, S. X. Electrospun P2-Type Na<sub>2/3</sub>(Fe<sub>1/2</sub>Mn<sub>1/2</sub>)O<sub>2</sub> Hierarchical Nanofibers as Cathode Material for Sodium-Ion Batteries. *ACS Appl. Mater. Interfaces*, 6 (12): 8953–8958, 2014.
- 111 Jin, T., Liu, Y., Li, Y., Cao, K., Wang, X., Jiao, L. Electrospun NaVPO<sub>4</sub>F/C Nanofibers as Self-Standing Cathode Material for Ultralong Cycle Life Na-Ion Batteries. *Adv. Energy Mater.*, 7 (15): 1700087, 2017.
- 112 Li, Y., Li, Q., Tan, Z. A Review of Electrospun Nanofiber-Based Separators for Rechargeable Lithium-Ion Batteries. *J. Power Sources*, 443 (12): 227262, 2019.
- 113 Liu, M., Deng, N., Ju, J., Fan, L., Wang, L., Li, Z., Zhao, H., Yang, G., Kang, W., Yan, J., Cheng, B. A Review: Electrospun Nanofiber Materials for Lithium-Sulfur Batteries. *Adv. Funct. Mater.*, 29 (49): 1–34, 2019.
- 114 Bai, S., Liu, X., Zhu, K., Wu, S., Zhou, H. Metal-Organic Framework-Based Separator for Lithium-Sulfur Batteries. *Nat. Energy*, 1: 16094, 2016.
- 115 Jeong, Y. C., Kim, J. H., Kwon, S. H., Oh, J. Y., Park, J., Jung, Y., Lee, S. G., Yang, S. J., Park, C. R. Rational Design of Exfoliated 1T MoS<sub>2</sub>@CNT-Based Bifunctional Separators for Lithium Sulfur Batteries. *J. Mater. Chem. A*, 5 (45): 23909–23918, 2017.
- 116 Hou, T. Z., Chen, X., Peng, H. J., Huang, J. Q., Li, B. Q., Zhang, Q., Li, B. Design Principles for Heteroatom-Doped Nanocarbon to Achieve Strong Anchoring of Polysulfides for Lithium–Sulfur Batteries. *Small*, 12 (24): 3283–3291, 2016.
- 117 He, Y., Qiao, Y., Chang, Z., Cao, X., Jia, M., He, P., Zhou, H. Developing A “Polysulfide-Phobic” Strategy to Restrain Shuttle Effect in Lithium–Sulfur Batteries. *Angew. Chemie - Int. Ed.*, 58 (34): 11774–11778, 2019.
- 118 Conder, J., Forner-Cuenca, A., Gubler, E. M., Gubler, L., Novák, P., Trabesinger, S. Performance-Enhancing Asymmetric Separator for Lithium-Sulfur Batteries. *ACS Appl. Mater. Interfaces*, 8 (29): 18822–18831, 2016.
- 119 Ahn, W., Lim, S. N., Lee, D. U., Kim, K. B., Chen, Z., Yeon, S. H. Interaction Mechanism between a Functionalized Protective Layer and Dissolved Polysulfide for Extended Cycle Life of Lithium Sulfur Batteries. *J. Mater. Chem. A*, 3 (18): 9461–9467, 2015.

- 
- 120 Jeong, Y. C., Kim, J. H., Nam, S., Park, C. R., Yang, S. J. Rational Design of Nanostructured Functional Interlayer/Separator for Advanced Li–S Batteries. *Adv. Funct. Mater.*, 28 (38): 1–32, 2018.
- 121 Yao, H., Yan, K., Li, W., Zheng, G., Kong, D., Seh, Z. W., Narasimhan, V. K., Liang, Z., Cui, Y. Improved Lithium-Sulfur Batteries with a Conductive Coating on the Separator to Prevent the Accumulation of Inactive S-Related Species at the Cathode-Separator Interface. *Energy Environ. Sci.*, 7 (10): 3381–3390, 2014.
- 122 Su, Y. S., Manthiram, A. A New Approach to Improve Cycle Performance of Rechargeable Lithium-Sulfur Batteries by Inserting a Free-Standing MWCNT Interlayer. *Chem. Commun.*, 48 (70): 8817–8819, 2012.
- 123 Ji, Y., Hu, J., Biskupek, J., Kaiser, U., Song, Y. F., Streb, C. Polyoxometalate-Based Bottom-Up Fabrication of Graphene Quantum Dot/Manganese Vanadate Composites as Lithium Ion Battery Anodes. *Chem. - A Eur. J.*, 23 (65): 16637–16643, 2017.
- 124 Ji, Y., Huang, L., Hu, J., Streb, C., Song, Y. Polyoxometalate-Functionalized Nanocarbon Materials for Energy Conversion, Energy Storage and Sensor Systems. *Energy Environ. Sci.*, 8776–789, 2015.
- 125 Hu, J., Ji, Y., Chen, W., Streb, C., Song, Y. “Wiring” Redox-Active Polyoxometalates to Carbon Nanotubes Using a Sonication-Driven Periodic Functionalization Strategy. *Energy Environ. Sci.*, 9 (3): 1095–1101, 2016.
- 126 Ji, Y., Hu, J., Huang, L., Chen, W., Streb, C., Song, Y. F. Covalent Attachment of Anderson-Type Polyoxometalates to Single-Walled Carbon Nanotubes Gives Enhanced Performance Electrodes for Lithium Ion Batteries. *Chem. - A Eur. J.*, 21 (17): 6469–6474, 2015.
- 127 Ji, Y., Ma, Y., Liu, R., Ma, Y., Cao, K., Kaiser, U., Varzi, A., Song, Y. F., Passerini, S., Streb, C. Modular Development of Metal Oxide/Carbon Composites for Electrochemical Energy Conversion and Storage. *J. Mater. Chem. A*, 7 (21): 13096–13102, 2019.
- 128 Long, D. L., Tsunashima, R., Cronin, L. Polyoxometalates: Building Blocks for Functional Nanoscale Systems. *Angew. Chemie - Int. Ed.*, 49 (10): 1736–1758, 2010.
- 129 Nishimoto, Y., Yokogawa, D., Yoshikawa, H., Awaga, K., Irlé, S. Super-Reduced Polyoxometalates: Excellent Molecular Cluster Battery Components and Semipermeable Molecular Capacitors. *J. Am. Chem. Soc.*, 136 (25): 9042–9052, 2014.
- 130 Wang, H., Hamanaka, S., Nishimoto, Y., Irlé, S., Yokoyama, T., Yoshikawa, H., Awaga, K. In Operando X-Ray Absorption Fine Structure Studies of Polyoxometalate Molecular

- Cluster Batteries: Polyoxometalates as Electron Sponges. *J. Am. Chem. Soc.*, 134 (10): 4918–4924, 2012.
- 131 Kawasaki, N., Wang, H., Nakanishi, R., Hamanaka, S., Kitaura, R., Shinohara, H., Yokoyama, T., Yoshikawa, H., Awaga, K. Nanohybridization of Polyoxometalate Clusters and Single-Wall Carbon Nanotubes: Applications in Molecular Cluster Batteries. *Angew. Chemie - Int. Ed.*, 50 (15): 3471–3474, 2011.
- 132 Ma, D., Liang, L., Chen, W., Liu, H., Song, Y. F. Covalently Tethered Polyoxometalate-Pyrene Hybrids for Noncovalent Sidewall Functionalization of Single-Walled Carbon Nanotubes as High-Performance Anode Material. *Adv. Funct. Mater.*, 23 (48): 6100–6105, 2013.
- 133 Hu, J., Diao, H., Luo, W., Song, Y. F. Dawson-Type Polyoxomolybdate Anions ( $P_2Mo_{18}O_{62}^{6-}$ ) Captured by Ionic Liquid on Graphene Oxide as High-Capacity Anode Material for Lithium-Ion Batteries. *Chem. - A Eur. J.*, 23 (36): 8729–8735, 2017.
- 134 Li, M., Cong, L., Zhao, J., Zheng, T., Tian, R., Sha, J., Su, Z., Wang, X. Self-Organization towards Complex Multi-Fold Meso-Helices in the Structures of Wells-Dawson Polyoxometalate-Based Hybrid Materials for Lithium-Ion Batteries. *J. Mater. Chem. A*, 5 (7): 3371–3376, 2017.
- 135 Chen, H. Y., Friedl, J., Pan, C. J., Haider, A., Al-Oweini, R., Cheah, Y. L., Lin, M. H., Kortz, U., Hwang, B. J., Srinivasan, M., Stimming, U. In Situ X-Ray Absorption near Edge Structure Studies and Charge Transfer Kinetics of  $Na_6[V_{10}O_{28}]$  Electrodes. *Phys. Chem. Chem. Phys.*, 19 (4): 3358–3365, 2017.
- 136 Bachtin, K. Elektrospinning von Kathodenmaterialien Für Lithium Ionen Batterien. Ph.D. Dissertation, Karlsruher Institute of Technology ( KIT ), Karlsruhe, 2016.
- 137 Wu, Y., Reddy, M. V, Chowdari, B. V. R., Ramakrishna, S. Long-Term Cycling Studies on Electrospun Carbon Nanofibers as Anode Material for Lithium Ion Batteries. *ACS Appl. Mater. Interfaces*, 5 (22): 12175–12184, 2013.
- 138 Liu, J., Wang, P. H., Li, R. Y. Continuous Carbonization of Polyacrylonitrile-based Oxidized Fibers: Aspects on Mechanical Properties and Morphological Structure. *J. Appl. Polym. Sci.*, 52 (7): 945–950, 1994.
- 139 Ferrari, A. C. Raman Spectroscopy of Graphene and Graphite: Disorder, Electron–phonon Coupling, Doping and Nonadiabatic Effects. *Solid State Commun.*, 143 (1): 47–57, 2007.

- 
- 140 López-Honorato, E., Meadows, P. J., Shatwell, R. A., Xiao, P. Characterization of the Anisotropy of Pyrolytic Carbon by Raman Spectroscopy. *Carbon*, 48881–890, 2010.
- 141 Sadezky, A., Muckenhuber, H., Grothe, H., Niessner, R., Pöschl, U. Raman Microspectroscopy of Soot and Related Carbonaceous Materials: Spectral Analysis and Structural Information. *Carbon*, 43 (8): 1731–1742, 2005.
- 142 Bokobza, L., Bruneel, J.-L., Couzi, M. Raman Spectra of Carbon-Based Materials (from Graphite to Carbon Black) and of Some Silicone Composites. *C*, 1 (1): 77–94, 2015.
- 143 Peng, Y. T., Lo, C. T. Effect of Microstructure and Morphology of Electrospun Ultra-Small Carbon Nanofibers on Anode Performances for Lithium Ion Batteries. *J. Electrochem. Soc.*, 162 (6): A1085–A1093, 2015.
- 144 Boaretto, N., Rana, M., Marcilla, R., Vilatela, J. J. Revealing the Mechanism of Electrochemical Lithiation of Carbon Nanotube Fibers. *ACS Appl. Energy Mater.*, 3 (9): 8695–8705, 2020.
- 145 Komaba, S., Murata, W., Ishikawa, T., Yabuuchi, N., Ozeki, T., Nakayama, T., Ogata, A., Gotoh, K., Fujiwara, K. Electrochemical Na Insertion and Solid Electrolyte Interphase for Hard-Carbon Electrodes and Application to Na-Ion Batteries. *Adv. Funct. Mater.*, 21 (20): 3859–3867, 2011.
- 146 Wu, F., Dong, R., Bai, Y., Li, Y., Chen, G., Wang, Z., Wu, C. Phosphorus-Doped Hard Carbon Nanofibers Prepared by Electrospinning as an Anode in Sodium-Ion Batteries. *ACS Appl. Mater. Interfaces*, 10 (25): 21335–21342, 2018.
- 147 Stevens, D. A., Dahn, J. R. The Mechanisms of Lithium and Sodium Insertion in Carbon Materials. *J. Electrochem. Soc.*, 148 (8): 803–811, 2001.
- 148 Zhu, J., Chen, C., Lu, Y., Ge, Y., Jiang, H., Fu, K., Zhang, X. Nitrogen-Doped Carbon Nanofibers Derived from Polyacrylonitrile for Use as Anode Material in Sodium-Ion Batteries. *Carbon N. Y.*, 94 (11): 189–195, 2015.
- 149 Chen, T., Liu, Y., Pan, L., Lu, T., Yao, Y., Sun, Z., Chua, D. H. C., Chen, Q. Electrospun Carbon Nanofibers as Anode Materials for Sodium Ion Batteries with Excellent Cycle Performance. *J. Mater. Chem. A*, 2 (12): 4117–4121, 2014.
- 150 Hong, K. L., Qie, L., Zeng, R., Yi, Z. Q., Zhang, W., Wang, D., Yin, W., Wu, C., Fan, Q. J., Zhang, W. X., Huang, Y. H. Biomass Derived Hard Carbon Used as a High Performance Anode Material for Sodium Ion Batteries. *J. Mater. Chem. A*, 2 (32): 12733–12738, 2014.

- 151 Wang, J., Polleux, J., Lim, J., Dunn, B. Pseudocapacitive Contributions to Electrochemical Energy Storage in TiO<sub>2</sub> (anatase) Nanoparticles. *J. Phys. Chem. C*, 111 (40): 14925–14931, 2007.
- 152 Euchner, H., Vinayan, B. P., Reddy, M. A., Fichtner, M., Groß, A. Alkali Metal Insertion into Hard Carbon-the Full Picture. *J. Mater. Chem. A*, 8 (28): 14205–14213, 2020.
- 153 Anji Reddy, M., Helen, M., Groß, A., Fichtner, M., Euchner, H. Insight into Sodium Insertion and the Storage Mechanism in Hard Carbon. *ACS Energy Lett.*, 3 (12): 2851–2857, 2018.
- 154 Hou, H., Qiu, X., Wei, W., Zhang, Y., Ji, X. Carbon Anode Materials for Advanced Sodium-Ion Batteries. *Adv. Energy Mater.*, 7 (24): 1–30, 2017.
- 155 Gogotsi, Y., Penner, R. M. Energy Storage in Nanomaterials - Capacitive, Pseudocapacitive, or Battery-Like. *ACS Nano*, 12 (3): 2081–2083, 2018.
- 156 Tian, G., Zhao, Z., Sarapulova, A., Das, C., Zhu, L., Liu, S., Missiul, A., Welter, E., Maibach, J., Dsoke, S. Understanding the Li-Ion Storage Mechanism in a Carbon Compositing Zinc Sulfide Electrode. *J. Mater. Chem. A*, 7 (26): 15640–15653, 2019.
- 157 Bard, A. J., Faulkner, L. R. *Electrochemical Method: Fundamentals and Applications*; John Wiley & Sons: New York, 1980.
- 158 Wang, D., Wu, Y., Lv, J., Wang, R., Xu, S. Carbon Encapsulated Maricite NaFePO<sub>4</sub> Nanoparticles as Cathode Material for Sodium-Ion Batteries. *Colloids Surfaces A Physicochem. Eng. Asp.*, 583 (12): 123957, 2019.
- 159 Zhu, Y., Xu, Y., Liu, Y., Luo, C., Wang, C. Comparison of Electrochemical Performances of Olivine NaFePO<sub>4</sub> in Sodium-Ion Batteries and Olivine LiFePO<sub>4</sub> in Lithium-Ion Batteries. *Nanoscale*, 5 (2): 780–787, 2013.
- 160 Ferrari, A. C., Robertson, J. Interpretation of Raman Spectra of Disordered and Amorphous Carbon. *Phys. Rev. B*, 61 (20): 14095–14107, 2000.
- 161 Zhao-Karger, Z., Liu, R., Dai, W., Li, Z., Diemant, T., Vinayan, B. P., Bonatto Minella, C., Yu, X., Manthiram, A., Behm, R. J., Ruben, M., Fichtner, M. Toward Highly Reversible Magnesium-Sulfur Batteries with Efficient and Practical Mg[B(hfip)<sub>4</sub>]<sub>2</sub> Electrolyte. *ACS Energy Lett.*, 3 (8): 2005–2013, 2018.
- 162 Zhao-Karger, Z., Gil Bardaji, M. E., Fuhr, O., Fichtner, M. A New Class of Non-Corrosive, Highly Efficient Electrolytes for Rechargeable Magnesium Batteries. *J. Mater. Chem. A*, 5 (22): 10815–10820, 2017.

- 
- 163 Day, V. W., Klemperer, W. G., Maltbie, D. J. Where Are the Protons in  $\text{H}_3\text{V}_{10}\text{O}_{28}^{3-}$ ? *J. Am. Chem. Soc.*, 109 (10): 2991–3002, 1987.
- 164 Scofield, J. H. Hartree-Slater Subshell Photoionization Cross-Sections AT 1254 and 1478 eV. *J. Electron Spectros. Relat. Phenomena*, 8 (2): 129–137, 1976.
- 165 Hippauf, F., Nickel, W., Hao, G. P., Schwedtmann, K., Giebeler, L., Oswald, S., Borchardt, L., Doerfler, S., Weigand, J. J., Kaskel, S. The Importance of Pore Size and Surface Polarity for Polysulfide Adsorption in Lithium Sulfur Batteries. *Adv. Mater. Interfaces*, 3 (18): 1–9, 2016.
- 166 Meng, Z., Foix, D., Brun, N., Dedryvère, R., Stievano, L., Morcrette, M., Berthelot, R. Alloys to Replace Mg Anodes in Efficient and Practical Mg-Ion/Sulfur Batteries. *ACS Energy Lett.*, 4 (9): 2040–2044, 2019.
- 167 Muthuraj, D., Ghosh, A., Kumar, A., Mitra, S. Nitrogen and Sulfur Doped Carbon Cloth as Current Collector and Polysulfide Immobilizer for Magnesium-Sulfur Batteries. *ChemElectroChem*, 6 (3): 684–689, 2019.
- 168 Maletti, S., Podetti, F. S., Oswald, S., Giebeler, L., Barbero, C. A., Mikhailova, D., Balach, J.  $\text{LiV}_3\text{O}_8$ -Based Functional Separator Coating as Effective Polysulfide Mediator for Lithium-Sulfur Batteries. *ACS Appl. Energy Mater.*, 3 (3): 2893–2899, 2020.
- 169 Fan, Y., Ma, F., Liang, J., Chen, X., Miao, Z., Duan, S., Wang, L., Wang, T., Han, J., Cao, R., Jiao, S., Li, Q. Accelerated Polysulfide Conversion on Hierarchical Porous Vanadium-Nitrogen-Carbon for Advanced Lithium-Sulfur Batteries. *Nanoscale*, 12 (2): 584–590, 2020.
- 170 Zubair, U., Bianco, S., Amici, J., Francia, C., Bodoardo, S. Probing the Interaction Mechanism of Heterostructured  $\text{VO}_x\text{N}_y$  Nanoparticles Supported in Nitrogen-Doped Reduced Graphene Oxide Aerogel as an Efficient Polysulfide Electrocatalyst for Stable Sulfur Cathodes. *J. Power Sources*, 461 (4): 228144, 2020.
- 171 Chen, G. Z. Supercapacitor and Supercapattery as Emerging Electrochemical Energy Stores. *Int. Mater. Rev.*, 62 (4): 173–202, 2017.
- 172 Luo, C. J., Stoyanov, S. D., Stride, E., Pelan, E., Edirisinghe, M. Electrospinning versus Fibre Production Methods: From Specifics to Technological Convergence. *Chem. Soc. Rev.*, 41 (13): 4708–4735, 2012.
- 173 Kannan, B., Cha, H., Hosie, I. C. Electrospinning—Commercial Applications, Challenges and Opportunities. *Nano-Size Polymers: Preparation, Properties, Applications*; Springer International Publishing: Cham, 2016.

## 9 Acknowledgement

When it comes to express my gratitude, the first person who comes to my mind is Prof. Helmut Ehrenberg. I am lucky and honored to spend the last three years at his group thanks to the precious opportunity which Helmut has offered me. I have also been very lucky to join the group of Dr. Sylvio Indris who has supervised me academically and scientifically. Guided by these two open-minded, kind, and easy-going characters, many procedures went very smoothly. I would also like to thank Prof. Rolf Schuster for his time and work invested as my second reviewer.

Secondly, I highly appreciate all the help and aid that all my colleagues at IAM have provided me. The most gratitude I have is towards Liuda Mereacre, who has been such an important role at the institute, for her patience, kindness, and hardworking. Our senior scientist and postdocs: Dr. Michael Knapp, Dr. Weibo Hua, Dr. Christian Njel, Dr. Guiying Tian, Dr. Jiangong Zhu, Dr. Qiang Fu and all other group leaders and scientists have given me great guidance and advice with their intelligent minds. Udo Geckle, Heinz-Robert Goebel, Almut Kriese, Bettina Hunzinger, all other technicians and staff have been supportive to help me carry out my work efficiently. Also, I would like to thank all other PhD students who have helped me in many different folds and everyone's effort for a harmonic and friendly atmosphere.

Thirdly, I would like to thank Charlotte Waldhelm, who has finished her bachelor thesis and worked as a Hiwi with me, for her work involved in the first part of my thesis. I thank Dr. Jiyuan Chun and Dr. Zhao-Karger, who have cooperated with me to accomplish the modified separator for Mg-S battery. It was very satisfying and efficient work which showed me the important value of teamwork.

Last but not least, I would like to say thank you to my mom: "Xie Xie Ma Ma" for her bravery, hard work, support and everything. I also thank my husband who has taken my hands and lead me to a whole new life in Germany.

The journey at KIT, Karlsruhe, has been a pleasant one exceeded my expectations in many ways. It was also a hard one in positive ways that helped me grew up not only academically, but also in building more determined mind and stronger character. I thank myself for coming all the way to this end. "**P**ositive, **H**old on, **D**on't give up" is a life-long motto.